Research Square

Preprints are preliminary reports that have not undergone peer review.
They should not be considered conclusive, used to inform clinical practice,
or referenced by the media as validated information.

Convergent utilization of APN receptor by hedgehog merbecoviruses

Huan Yan

huanyan@whu.edu.cn

Wuhan University https://orcid.org/0000-0001-8744-8665

Peng Liu

Wuhan University

Qianhui Zhu

Institute of Biophysics Chinese Academy of Sciences

Jingyi Liu

Peking University

Zhixing Ma

Wuhan University

Guocui Mou

Chinese Academy of Medical Sciences (CAMS) & Peking Union Medical College (PUMC)

Yuanling Yu

Beijing Changping Laboratory

Chen Liu

Wuhan University

Chengbao Ma

Wuhan University

Junyu Si

Wuhan University

Xiao Yang

Wuhan University

Meiling Huang

Wuhan University

Yanchu Liu

Wuhan University https://orcid.org/0009-0001-8411-7470

Yehui Sun

Wuhan University

Xiao Yu

Wuhan University

Yucheng Sun

Wuhan University

Tianci Liu

Changping Laboratory, Beijing

Lingling Yu

Beijing Changping Laboratory

Qianran Wang

Beijing Changping Laboratory

Honghao Ma

Beijing Changping Laboratory

Qi Lv

Key Laboratory of Human Disease Comparative Medicine, Chinese Ministry of Health, Beijing Key Laboratory for Animal Models of Emerging and Remerging Infectious Diseases, Institute of Laboratory Anim

Jing Li

Wuhan University

Linlin Bao

Institute of Laboratory Animal Science, Chinese Academy of Medical Sciences

Yunlong Cao

Peking University https://orcid.org/0000-0001-5918-1078

Xiangxi Wang

Institute of Biophysics, Chinese Academy of Sciences https://orcid.org/0000-0003-0635-278X

Biological Sciences - Article

Keywords: Merbecovirus, EriCoV, APN, receptor, hedgehog, TMPRSS2, Neutralizing antibodies

Posted Date: February 18th, 2026

DOI: https://doi.org/10.21203/rs.3.rs-8368823/v1

License: This work is licensed under a Creative Commons Attribution 4.0 International License. Read Full License

Additional Declarations: There is **NO** Competing Interest.

Version of Record: A version of this preprint was published at Nature Microbiology on September 16th, 2026. See the published version at https://doi.org/10.1038/s41564-026-02478-1.

Convergent utilization of APN receptor by hedgehog merbecoviruses

Peng Liu[1,#], Qianhui Zhu[2,3,#], Jingyi Liu[4,5,7,#], Zhixing Ma[1,#], Guocui Mou[8,#], Yuanling Yu[5], Chen Liu[1], Chengbao Ma[1], Junyu Si[1], Xiao Yang[1], Meiling Huang[1], Yanchu Liu[1], Yehui Sun[1], Xiao Yu[1], Yucheng Sun[1], Tianci Liu[2,3], Lingling Yu[5], Qianran Wang[5], Honghao Ma[5], Qi Lv[8], Jing Li[1], Linlin Bao[8,*], Yunlong Cao[4,5,6,*], Xiangxi Wang[2,3,*], Huan Yan[1,*]

Affiliations:

[1]State Key Laboratory of Virology and Biosafety, Hubei Provincial Research Center for Basic Biological Sciences, College of Life Sciences, TaiKang Center for Life and Medical Sciences, Wuhan University; Wuhan, Hubei, China

[2]Key Laboratory of Biomacromolecules (CAS), National Laboratory of Biomacromolecules, CAS Center for Excellence in Biomacromolecules, Institute of Biophysics, Chinese Academy of Sciences, Beijing, China

[3]University of Chinese Academy of Sciences, Beijing, China

[4]Biomedical Pioneering Innovation Center (BIOPIC), Peking University, Beijing, China

[5]Changping Laboratory, Beijing, China

[6]Peking-Tsinghua Center for Life Sciences, Tsinghua University, Beijing, China

[7]College of Future Technology, Peking University, Beijing, China

[8]Institute of Laboratory Animal Science, Chinese Academy of Medical Sciences (CAMS) & Peking Union Medical College (PUMC), Beijing, China

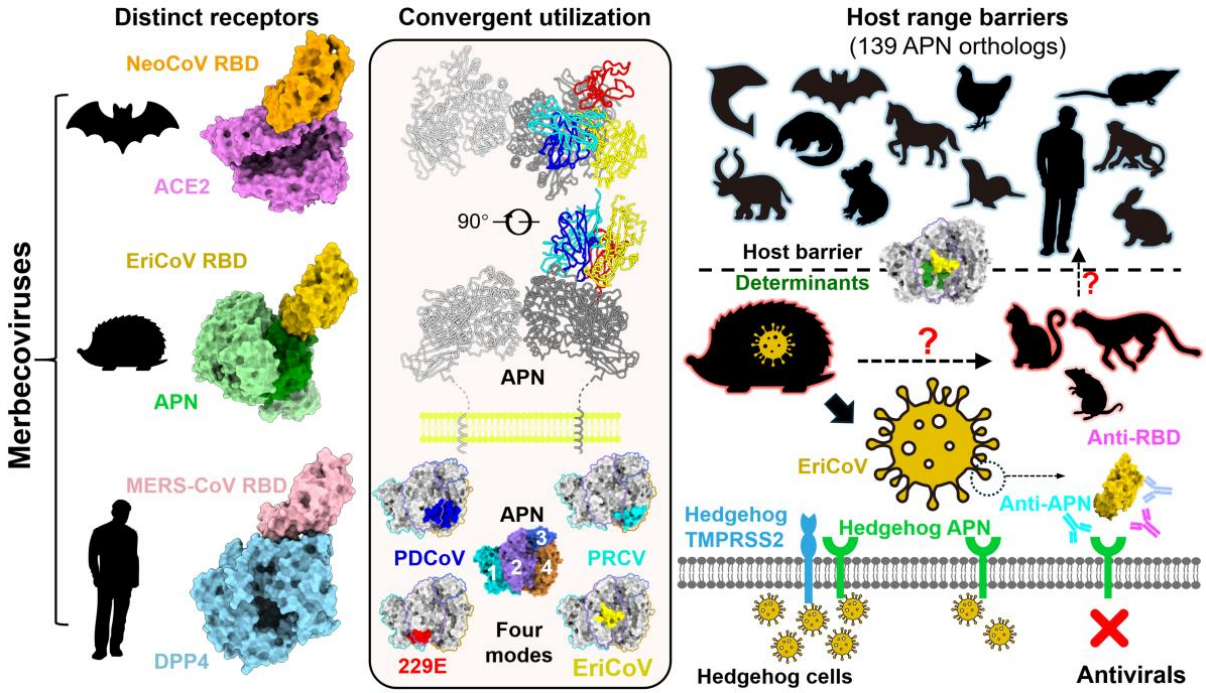
[#]These authors contributed equally to this work.

*Correspondence: Linlin Bao: bllmsl@aliyun.com (L.B.), Yunlong Cao: yunlongcao@pku.edu.cn (Y.C.), Xiangxi Wang: xiangxi@ibp.ac.cn (X.W.), Huan Yan: huanyan@whu.edu.cn (H.Y.)

Summary

Dipeptidyl peptidase-4 (DPP4) and angiotensin-converting enzyme 2 (ACE2) are well-established receptors for merbecoviruses, yet the receptor usage of merbecoviruses of European and Asian hedgehogs (EriCoVs) remains unknown[1–7]. Here, by testing hedgehog orthologs of known coronavirus receptors, we identify hedgehog aminopeptidase N (APN) as a functional receptor for various EriCoVs. Analysis of APN orthologs from 139 species reveals that EriCoVs exhibit a restricted host range, primarily utilizing APN from hedgehogs and, to a lesser extent, felids and some other species, shaped by specific molecular determinants at the virus–receptor interface. Cryo-EM analysis of EriCoV–APN complex reveals a novel APN-binding mode that is distinct from those used by alpha- and deltacoronaviruses. Functional assays further demonstrate that transmembrane serine protease 2 (TMPRSS2) enhances spike activation and promotes plasma membrane fusion. Neutralizing antibodies targeting the EriCoV RBD and hedgehog APN were generated and effectively blocked EriCoV pseudovirus entry or amplification in hedgehog-APN expressing human cells or primary hedgehog cells. The structural basis underlying the pan-EriCoV neutralization mediated by the RBD-targeting antibody BD23-0177 was further elucidated by cryo-EM analysis. Together, these findings uncover an unexpected convergent evolution of APN utilization among merbecoviruses, establishing a foundation for risk assessment and the development of targeted countermeasures.

Keywords: *Merbecovirus*; EriCoV; APN; receptor; hedgehog; TMPRSS2; Neutralizing antibodies



Graphic abstract: Convergent utilization of hedgehog APN by EriCoVs

Introduction

Three human betacoronaviruses—SARS-CoV-1, MERS-CoV, and SARS-CoV-2—have caused devastating outbreaks in the 21st century[8–12]. Among betacoronaviruses, the *Merbecovirus* subgenus has been designated a priority pathogen group by the World Health Organization (WHO)[13,14]. These viruses include the highly pathogenic Middle East respiratory syndrome coronavirus (MERS-CoV), which infects both humans and camels[10,15,16], along with numerous relatives with varying degrees of zoonotic potential[17–19].

Among them, *Betacoronavirus cameli* (MERSr-CoV), *Betacoronavirus pipistrelli* (HKU5), and *Betacoronavirus tylonycteridis* (HKU4) are three viral species that originated in bats[20–25] and have spilled over into mammals such as humans[10], camels[26–28], pangolins[4,29], and minks[30]. In 2013, a novel merbecovirus species (*Betacoronavirus erinacei*, or EriCoV/ErinCoV) was discovered in fecal samples from European hedgehogs (*Erinaceus europaeus*, *E.eur*) in Germany[31]. A related Asian lineage (HKU31) was later found in Amur hedgehogs (*Erinaceus amurensis*, *E.amu*) in China[32]. To date, EriCoVs have been reported exclusively in hedgehogs across a broad geographic range across Euroasia, including Germany[31], France[33], United Kingdom[34], Italy[35,36], Poland[37,38], Portugal[39], Russia[40], and China[32,41,42]. Among them, all Asian EriCoVs were sampled in *E.amu* hedgehogs, while nearly all European EriCoVs were found in *E.eur* hedgehogs, except for one strain found in *E.rou* hedgehogs and six strains from Moscow annotated as *Erinaceus sp.*[40]. Despite their broad geographic distribution and genetic diversity, EriCoVs remain poorly understood in terms of pathogenicity and cross-species potential[33,39].

The host range and transmissibility of coronaviruses are primarily determined by interactions between the spike (S) protein receptor-binding domain (RBD) and specific cellular receptors[43]. So far, at least six host proteins have been established as functional coronavirus receptors: carcinoembryonic antigen-related cell adhesion molecule 1a (CEACAM1a)[44,45], angiotensin-converting enzyme 2 (ACE2)[1–3], dipeptidyl peptidase-4 (DPP4)[21,22,46,47], aminopeptidase N (APN)[48,49], transmembrane protease serine 2 (TMPRSS2)[50–53], and dipeptidase 1 (DPEP1)[54]. Among them, ACE2 and APN are recognized by phylogenetically diverse coronaviruses with distinct RBD structures, indicating multiple independent receptor acquisition events during evolution[5,7,55]. ACE2 usage is shared by coronaviruses across alpha- and betacoronavirus, including setracoviruses (e.g., NL63[2]), sarbecoviruses (e.g., SARS-CoV-2[12,56,57]), and several merbecovirus clades (e.g., NeoCoV[1], MOW15-22[7], HKU5[5,6,30,58–60], HKU25[61]). APN serves as a receptor for multiple alpha- and deltacoronaviruses, including duvinacoviruses (e.g., 229E[48]), tegacoviruses (e.g., TGEV[49], CCoV-HuPn-2018[62], FCoV-23[63]), and buldecoviruses (e.g., PDCoV[64], and multiple Avian deltacoronaviruses[65]). TMPRSS2, besides serving as a functional receptor for HKU1, is a critical protease for spike activation of many coronaviruses, influencing the entry route and tropism of these viruses[57,66–68].

While DPP4 has been considered the canonical receptor for merbecoviruses, recent findings suggest that ACE2 usage may be more prevalent than previously apprehended[1,5,7,59]. In 2022, we reported that NeoCoV and PDF-2180, close relatives of MERS-CoV in African bats, use ACE2 as their functional receptors[1,69]. Subsequently, several other merbecovirus clades were also found to acquire ACE2 usage independently[5,7,59,61]. However, EriCoVs do not use either ACE2 or DPP4 for entry, leaving their entry and transmission mechanism unresolved[1,6,70].

Here, we show that EriCoVs use hedgehog APN as an entry receptor and can utilize hedgehog TMPRSS2 for efficient cell surface spike activation. Cryo-EM analyses unveil a previously

unrecognized APN-binding mode, representing the first case of convergent APN utilization by betacoronavirus. Antibodies targeting EriCoV RBD and APN were developed that can efficiently and broadly neutralize pseudovirus entry *in vitro*, including in primary hedgehog cells. This study provided the last major piece to the long-standing puzzle of merbecovirus receptor usage, and points the way toward effective assessment and mitigation of the zoonotic threats posed by those MERS-CoV relatives.

Results

Characterization of EriCoV spikes

To investigate the receptor binding features of EriCoVs, we analyzed 26 publicly available EriCoV genomic sequences and 27 EriCoV S glycoprotein sequences, with particular focus on the RBD regions. For conciseness and clarity, EriCoV strain names were abbreviated in this study (Extended Data Fig. 1a and Supplementary Table 1). Among these, 5 Asian EriCoV strains (HKU31) were identified in Amur hedgehogs (*E.amurensis*) from several provinces of China, while 22 European EriCoV strains were identified in various European countries, predominantly confirmed from European hedgehogs (*E.europaeus*) (Fig. 1a).

Phylogenetic analyses of both genomic sequences and S glycoprotein amino acid sequences revealed that Asian and European EriCoVs form sister lineages, distant from bat-borne merbecoviruses (Fig. 1b and Extended Data Fig. 1b). This separation suggests a long-term evolutionary divergence of EriCoVs in hedgehogs across Eurasia. Consistent with previous findings, EriCoV RBD sequences cluster with those of ACE2-using NeoCoV and PDF-2180, implying a potential shared ancestry (Fig. 1c)[1]. However, due to limited sequence homology and likely different receptor usage patterns, we classified EriCoVs and NeoCoV-related viruses into distinct clades in this study. Among the analyzed sequences, pairwise amino acid sequence analysis of S and RBD shows that two representative EriCoV strains from Asian and European, respectively, share moderate sequence identity (78~79%), but both are markedly divergent from other merbecoviruses (32~51% for RBD and 53~63% for S), with NeoCoV being the closest known strain to EriCoVs (Fig. 1d).

Structural comparison of RBDs from representative merbecoviruses revealed that EriCoV and NeoCoV share a similar overall RBD core and receptor-binding motif (RBM) architecture, including characteristic insertion–deletion (indel) patterns (Fig. 1e), which have been implicated in receptor usage shifts during coronavirus evolution[71]. Further examination of the putative RBM sequences confirmed shared indel patterns between NeoCoV and EriCoVs, except for indel 1, which lies outside the canonical interaction interface. However, only 2 out of 14 ACE2-interacting NeoCoV residues are conserved in EriCoV[1], suggesting a distinct receptor engagement mechanism (Fig. 1f).

Collectively, these analyses suggest that EriCoVs likely employ a novel receptor-binding strategy that does not involve known ACE2 or DPP4 interaction modes, concurring with the observations in prior studies[1,6].

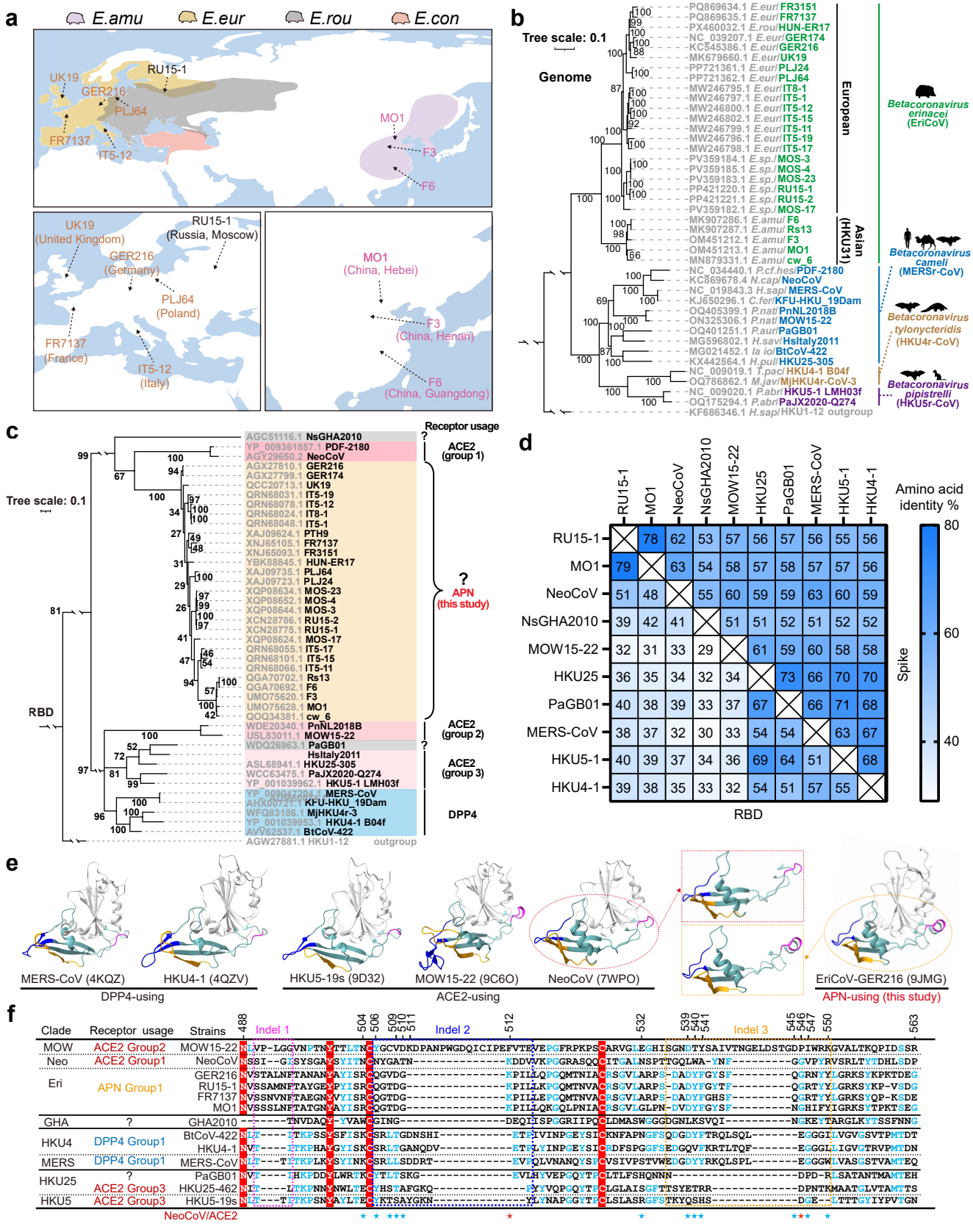

a
E.amu
E.eur
E.rou
E.con
UK19
GER216
RU15-1
PLJ64
FR7137
IT5-12
MO1
F3
F6
UK19 (United Kingdom)
RU15-1 (Russia, Moscow)
GER216 (Germany)
PLJ64 (Poland)
FR7137 (France)
IT5-12 (Italy)
MO1 (China, Hebei)
F3 (China, Henan)
F6 (China, Guangdong)
b
Tree scale: 0.1
Genome
European
Asian (HKU31)
Betacoronavirus erinacei (EriCoV)
Betacoronavirus cameli (MERSr-CoV)
Betacoronavirus tylonycteridis (HKU4r-CoV)
Betacoronavirus pipistrelli (HKU5r-CoV)
c
Tree scale: 0.1
RBD
Receptor usage
ACE2 (group 1)
APN (this study)
ACE2 (group 2)
ACE2 (group 3)
DPP4
outgroup
d
Amino acid identity %
Spike
RBD
e
MERS-CoV (4KQZ)
HKU4-1 (4QZV)
HKU5-19s (9D32)
MOW15-22 (9C6O)
NeoCoV (7WPO)
EriCoV-GER216 (9JMG)
DPP4-using
ACE2-using
APN-using (this study)
f
Clade
Receptor usage
Strains
Indel 1
Indel 2
Indel 3
NeoCoV/ACE2

Fig. 1 | Geographic distribution, phylogenetic relationship, and RBD features of EriCoVs. (**a**) Geographic distribution of Erinaceus hedgehogs and reported sampling locations of selective EriCoV strains. Host abbreviations: *E.eur* (*Erinaceus europaeus*), *E.amu* (*Erinaceus amurensis*), *E.rou* (*Erinaceus roumanicus*), *E.con* (*Erinaceus concolor*). Species distribution data retrieved from the International Union for Conservation of Nature (IUCN) Red List were mapped using GeoScene Pro. The color scheme of EriCoVs corresponds to their host, except for RU15-1 with an unconfirmed hedgehog species (*Erinaceus sp.*). (**b-c**) Maximum-likelihood phylogenetic trees of representative merbecoviruses based on complete genome nucleotide sequences (b) or RBD amino acid sequences (corresponding to NeoCoV residues 380–585) (c) were generated by IQ-TREE. HKU1-12 was designated as the outgroup. Host, viral species, receptor usage, and receptor binding mode are annotated. ACE2-using merbecoviruses were grouped according to evolutionarily distinct receptor-binding modes characteristic of the NeoCoV- (clade 1), MOW15-22- (clade 2), and HKU5/HKU25-related (clade 3) clades. Scale bars denote genetic distance (substitutions per site). (**d**) Pairwise amino acid identity matrix of receptor-binding domains (RBDs) and full-length S glycoproteins for selected merbecoviruses. EriCoV strains were labeled in green. (**e**) Structures of representative merbecovirus RBDs. The conserved RBD core subdomains are rendered in gray, and receptor-binding motifs (RBMs) are rendered in dusty teal; structurally divergent RBM indels are highlighted (magenta: indel 1; dark blue: indel 2; orange: indel 3). The magnified RBMs from NeoCoV and EriCoV (GER216) were shown to facilitate comparison. (**f**) Manually adjusted multiple sequence alignment of RBMs with optimized indel positioning. Fully conserved residues are shown with a red background; partially conserved residues are colored with light blue. Dashed boxes define indels that correspond with panel e. Residues mediating ACE2 interactions by NeoCoV are asterisked (red: conserved in EriCoVs; blue: divergent). NeoCoV residue numbering is shown.

Hedgehog APN is a receptor for EriCoVs

Given previous failed attempts to identify receptor functionality among various mammalian ACE2 orthologs[1] and the hypothesis that EriCoVs may utilize an uncharacterized receptor binding mode, we explored whether these viruses engage alternative known coronavirus receptors from hedgehog hosts, including DPP4, APN, and the recently identified HKU1 receptor TMPRSS2. To this end, we retrieved protein-coding sequences of ACE2, DPP4, TMPRSS2, and APN from the RNA-seq data of *E. amurensis* hedgehog (Genome Sequence Archive, GSA database)[72] for subsequent evaluation. Notably, APN amino acid sequences were identical between *E.amu* and *E.eur* hedgehogs, allowing *E.amu* APN to serve as a representative for both hedgehog host species (Supplementary Table 2).

We first tested two representative EriCoV strains: RU15-1 (European) and MO1 (Asian). Among the tested receptors, only *E.amu* APN, but not *E.amu* ACE2, DPP4, TMPRSS2, or human (h) counterparts, supported detectable RBD binding (Fig. 2a) and RU15-1 and MO1 pseudovirus entry (Fig. 2b,c). Flow cytometry confirmed specific binding of EriCoV RBDs to *E.amu* APN but not to hAPN (Fig. 2d). A pull-down assay further demonstrated that EriCoV RBD, but not 229E RBD, interacted specifically with *E.amu* APN (Fig. 2e). Bio-layer interferometry (BLI) assays also demonstrated the binding between *E.amu* APN and RU15-1 or MO1 RBD, which displayed relatively low binding affinity and high dissociation rate (Extended Data Fig. 2a,b). Notably, mutation of the APN catalytic site[73] did not impair IT5-12 RBD binding or pseudovirus entry, indicating that receptor function is independent of protease activity (Fig. 2f,g).

We next evaluated whether *E.amu* APN also serves as a functional receptor for additional EriCoV strains. *E.amu* APN, but not *E.amu* ACE2 or hAPN, supported RBD-hFc binding from all tested EriCoV strains (Extended Data Fig. 2c). In a cell-cell fusion assay, *E.amu* APN promoted spike-mediated membrane fusion for most tested strains in a trypsin-dependent manner (Fig. 2h and Extended Data Fig. 2d). The *E.amu* APN and Trypsin dependence were further validated by entry assays using VSV pseudotyped with S glycoproteins from diverse EriCoV strains (Fig. 2i and Extended Data Fig. 2e).

Together, these data demonstrate that APN serves as a functional receptor for both Asian and European EriCoVs through specific interaction with their RBDs.

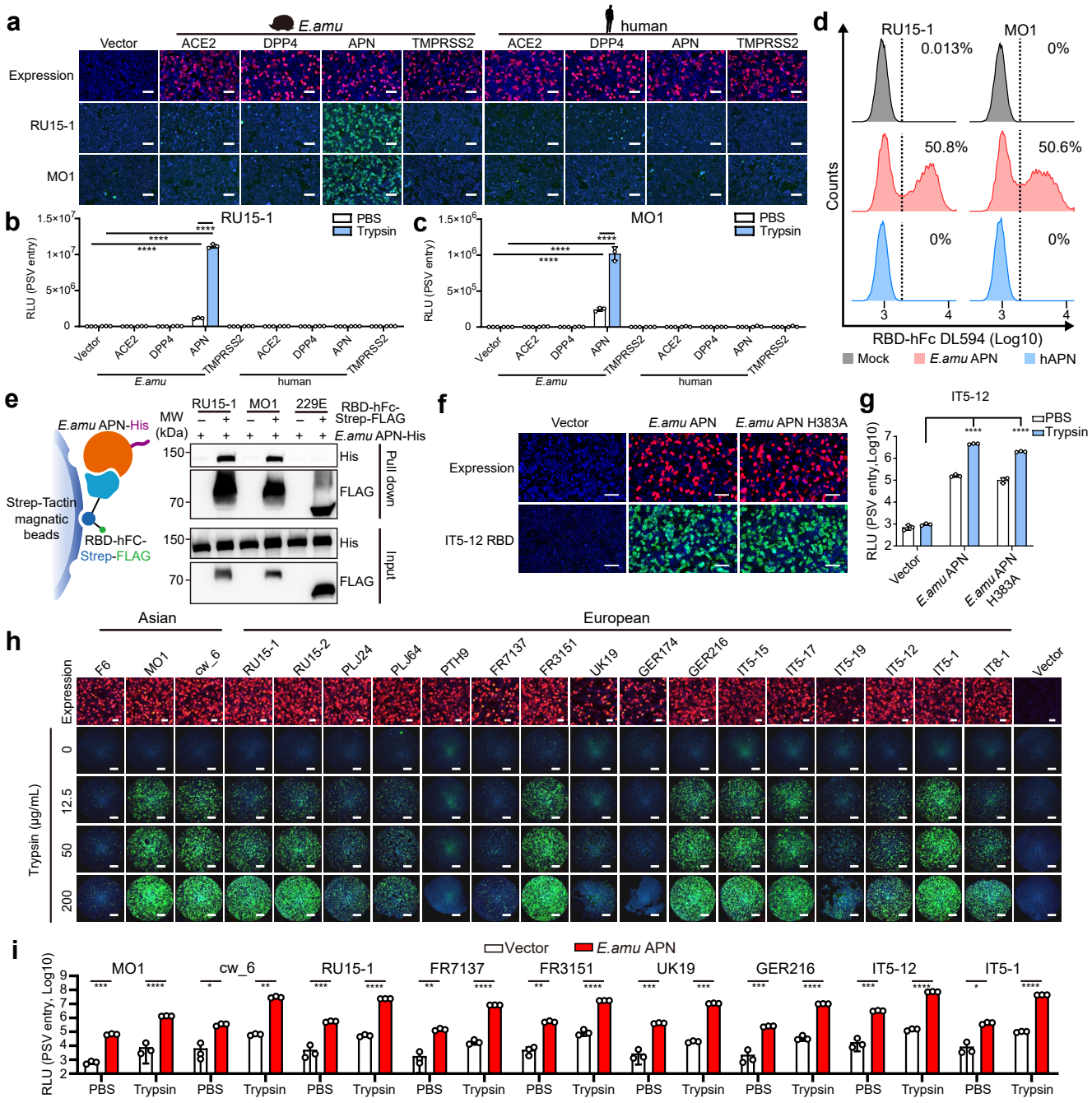

a
E.amu
human
Vector
ACE2
DPP4
APN
TMPRSS2
Expression
RU15-1
MO1
b
RU15-1
PBS
Trypsin
RLU (PSV entry)
c
MO1
d
RU15-1
MO1
0.013%
0%
50.8%
50.6%
0%
0%
Counts
RBD-hFc DL594 (Log10)
Mock
E.amu APN
hAPN
e
E.amu APN-His
Strep-Tactin magnatic beads
RBD-hFC-Strep-FLAG
MW (kDa)
RU15-1
MO1
229E
RBD-hFc-Strep-FLAG
E.amu APN-His
150
70
His
FLAG
Pull down
Input
f
Vector
E.amu APN
E.amu APN H383A
Expression
IT5-12 RBD
g
IT5-12
PBS
Trypsin
RLU (PSV entry,Log10)
h
Asian
European
F6
MO1
cw_6
RU15-1
RU15-2
PLJ24
PLJ64
PTH9
FR7137
FR3151
UK19
GER174
GER216
IT5-15
IT5-17
IT5-19
IT5-12
IT5-1
IT8-1
Vector
Expression
Trypsin (μg/mL)
0
12.5
50
200
i
Vector
E.amu APN
RLU (PSV entry, Log10)
PBS
Trypsin

Fig. 2 | Hedgehog APN functions as a receptor for EriCoVs. (**a-c**) Transient expression of *E. amurensis* (*E.amu*) APN, but not *E.amu* ACE2, DPP4, TMPRSS2, nor any tested human receptor counterparts, supported EriCoV RU15-1 and MO1 RBD human IgG1 Fc domain (hFc) fusion protein (RBD-hFc) binding (a), as well as pseudovirus entry (b-c) in HEK293T cells. Receptor expression was confirmed by immunofluorescence staining: FLAG-tagged ACE2, DPP4, and APN, and ALFA-tagged TMPRSS2 (red). Pseudoviruses (PSV) were pretreated with 1.25 mg/mL trypsin. (**d**) Flow cytometry analyses of RU15-1 and MO1 RBD-hFc binding to HEK293T cells transiently expressing hAPN or *E.amu* APN. Dashed lines: background threshold. Means of three technical repeats are shown. (**e**) Pull-down assay showing specific interaction of soluble *E.amu* APN ectodomain (His-tagged) with Strep-Tactin–immobilized RU15-1 or MO1 RBD-hFc-Strep-FLAG fusion proteins, with 229E RBD as a negative control. (**f-g**) *E.amu* APN receptor function is independent of its catalytic activity. IT5-12 RBD-hFc binding (f) and pseudovirus entry (g) in HEK293T cells transiently expressing WT *E.amu* APN or *E.amu* APN with H383A catalytic site mutation. Pseudoviruses were pretreated with PBS or 1.25 mg/mL trypsin. Mean ± SD for n=3 biological replicates. (**h**) S-mediated cell-cell membrane fusion of indicated Asian and European EriCoV strains in HEK293T cells stably expressing *E.amu* APN with the treatment of indicated concentrations of trypsin. S glycoprotein was evaluated by immunofluorescence, detecting the C-terminally fused HA tag (red). (**i**) Trypsin-pretreated (1.25 mg/mL trypsin) pseudovirus entry efficiency of selected EriCoV strains in HEK293T cells transiently expressing the *E.amu* APN. Mean ± SD and n=3 biological replicates for b,c,g, and i. Statistical significance was determined using unpaired two-tailed *t* tests. *: $P<0.05$, **: $P<0.01$, ***: $P<0.005$, ****: $P<0.001$, and NS: not significant. RLU: Relative light unit. Scale bars: 100 μm for a,f, and 5 mm for h.

Ortholog specificity and host tropism determinants

To assess the potential host range and spillover risk of EriCoVs, we examined the ability of various APN orthologs to support RBD binding and pseudovirus entry when transiently expressed in HEK293T cells. We first tested an APN library comprising 94 orthologs spanning 13 taxonomic orders (31 bats, 62 non-bat mammalian species, and one avian species), all with validated expressions (Fig. 3a, Extended Data Fig. 3a, and Supplementary Table 3).

Both the European (RU15-1) and Asian (MO1) EriCoV strains bound efficiently to hedgehog APN (*E.amu* APN) (Fig. 3b and Extended Data Fig. 3b). In contrast, APNs from *Sorex araneus* (*S.ara*) and *Suncus etruscus* (*S.etr*), which are also members of the order Eulipotyphla, did not support detectable binding. Notably, two feline APN orthologs from the leopard (*Panthera pardus, P.par*) and domestic cat (*Felis catus*, *F.cat*) supported detectable RU15-1 RBD binding, but not to MO1, indicating a strain-specific receptor compatibility (Fig. 3b and Extended Data Fig. 3b). Testing of additional APN orthologs from 40 Avian species, 2 marine mammalian species, and 3 other hedgehog-like/related species further confirmed the narrow host tropism of RU15-1 (Extended Data Fig. 4a-c). Notably, a recent study by Jin et al. reported that rat (*Rattus norvegicus, R.nor*) APN can function as an EriCoV receptor[74]. However, *R.nor* APN did not support RU15-1 or MO1 binding in our study. Therefore, we further verified the receptor function of selected APN orthologs from *P.par*, *F.cat, R.nor*, and African pygmy hedgehogs (*Atelerix albiventris, A.alb*) across multiple EriCoV strains. The result showed that *A.alb* APN, which shares 98.4% amino acid sequence identity, can support efficient binding of all tested species, while orthologs from felids and rats displayed suboptimal binding, with *R.nor* APN only supporting detectable FR7137 RBD binding (Fig. 3c). The GER216, FR7137, and PLJ64 are also capable of using hedgehog and felid APNs for pseudoviurs entry, highlighting the spillover potential of selected European EriCoV strains, especially FR7137 (Fig. 3c,d and Extended Data Fig. 4d).

To define the molecular basis of this restricted tropism, we constructed domain-swapped chimeras between human and *E.amu* APNs and assessed their ability to support EriCoV RBD binding (Fig. 3e). Substituting domain 2 of *E.amu* APN with its human counterpart abolished binding, while substituting *E.amu* Domain 2 with human APN counterpart restored binding, identifying domain 2 as a key determinant of species specificity. In contrast, swapping domains 1, 3, or 4 had minimal or no effect (Fig. 3f). Flow cytometry further confirmed the key contribution of domain 2 to species specificity (Fig. 3g). Fine mapping of domain 2 narrowed down the key host range determinants within region 288–331 (hAPN numbering), encompassing β16, β17, α1, and α2. Among them, β16 and α2 are more surface exposed, and the latter contains an N-319 glycosylation (Fig. 3h-j). Logoplot analysis based on the amino acid sequences of the 94 APN orthologs revealed high variability in this region, with *E.amu* APN displaying unique sequence features, particularly those around β16, as well as several key residues in α2 (Fig. 3k). The partial sequence similarity of this region in *F.cat* and *P.par* APNs and the absence of an evolutionarily conserved N319-glycosylation, but not in human or *S.ara* orthologs, likely explains their receptor compatibility.

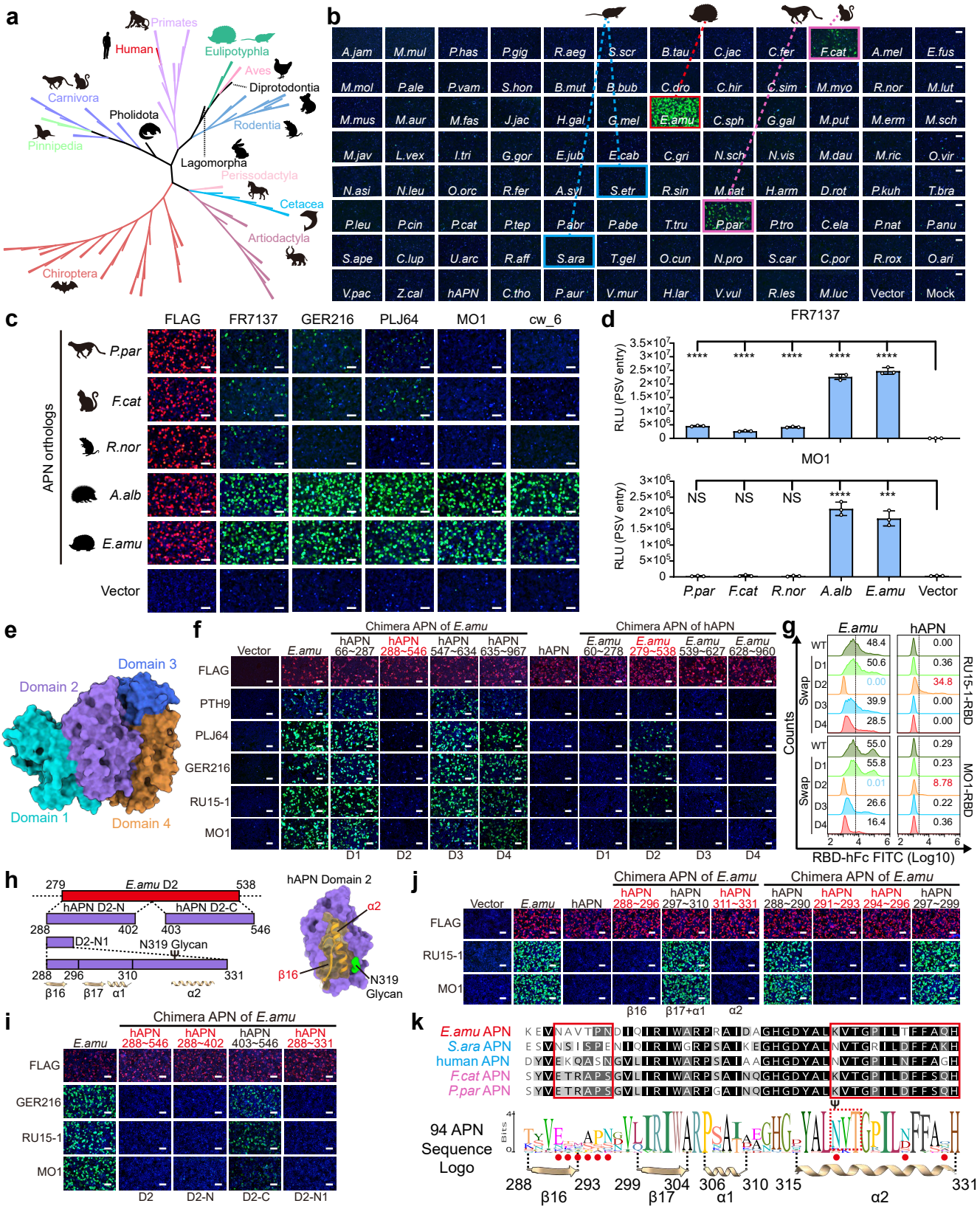

a
Primates
Human
Eulipotyphla
Aves
Diprotodontia
Carnivora
Pholidota
Rodentia
Pinnipedia
Lagomorpha
Perissodactyla
Cetacea
Artiodactyla
Chiroptera
b
A.jam M.mul P.has P.gig R.aeg S.scr B.tau C.jac C.fer F.cat A.mel E.fus
M.mol P.ale P.vam S.hon B.mut B.bub C.dro C.hir C.sim M.myo R.nor M.lut
M.mus M.aur M.fas J.jac H.gal G.mel E.amu C.sph G.gal M.put M.erm M.sch
M.jav L.vex I.tri G.gor E.jub E.cab C.gri N.sch N.vis M.dau M.ric O.vir
N.asi N.leu O.orc R.fer A.syl S.etr R.sin M.nat H.arm D.rot P.kuh T.bra
P.leu P.cin P.cat P.tep P.abr P.abe T.tru P.par P.tro C.ela P.nat P.anu
S.ape C.lup U.arc R.aff S.ara T.gel O.cun N.pro S.car C.por R.rox O.ari
V.pac Z.cal hAPN C.tho P.aur V.mur H.lar V.vul R.les M.luc Vector Mock
c
FLAG FR7137 GER216 PLJ64 MO1 cw_6
APN orthologs
P.par
F.cat
R.nor
A.alb
E.amu
Vector
d
FR7137
RLU (PSV entry)
3.5×10^7
3×10^7
2.5×10^7
2×10^7
1.5×10^7
1×10^7
5×10^6
0
****
MO1
3×10^6
2.5×10^6
2×10^6
1.5×10^6
1×10^6
5×10^5
NS
***
P.par F.cat R.nor A.alb E.amu Vector
e
Domain 3
Domain 2
Domain 1
Domain 4
f
Chimera APN of E.amu
Chimera APN of hAPN
Vector E.amu hAPN 66~287 hAPN 288~546 hAPN 547~634 hAPN 635~967 hAPN E.amu 60~278 E.amu 279~538 E.amu 539~627 E.amu 628~960
FLAG
PTH9
PLJ64
GER216
RU15-1
MO1
D1 D2 D3 D4
g
E.amu hAPN
WT D1 D2 D3 D4
Swap
Counts
48.4 50.6 0.00 39.9 28.5
0.00 0.36 34.8 0.00 0.00
RU15-1-RBD
55.0 55.8 0.01 26.6 16.4
0.29 0.23 8.78 0.22 0.36
MO1-RBD
RBD-hFc FITC (Log10)
h
279 E.amu D2 538
hAPN D2-N
hAPN D2-C
288 402 403 546
D2-N1
N319 Glycan
288 296 310 331
β16 β17 α1 α2
hAPN Domain 2
α2
β16
N319 Glycan
i
Chimera APN of E.amu
E.amu hAPN 288~546 hAPN 288~402 hAPN 403~546 hAPN 288~331
FLAG
GER216
RU15-1
MO1
D2 D2-N D2-C D2-N1
j
Chimera APN of E.amu
Chimera APN of E.amu
Vector E.amu hAPN hAPN 288~296 hAPN 297~310 hAPN 311~331 hAPN 288~290 hAPN 291~293 hAPN 294~296 hAPN 297~299
FLAG
RU15-1
MO1
β16 β17+α1 α2
k
E.amu APN
S.ara APN
human APN
F.cat APN
P.par APN
94 APN Sequence Logo
Bits
288 293 299 304 306 310 315 331
β16 β17 α1 α2

Fig. 3 | Multi-species APN tropism and host range determination of EriCoV. (**a**) Maximal likelihood phylogenetic trees of 94 APN orthologs from indicated species were constructed using IQ-TREE based on amino acid sequences. Taxonomic orders were annotated. Ortholog details are provided in Supplementary Table 3. (**b**) Binding of RU15-1 RBD-hFc (green) to HEK293T cells transiently expressing the indicated APN orthologs, assessed by immunofluorescence using an anti-hFc antibody. Red box: efficient binding. Magenta box: detectable binding. Blue box: two Eulipotyphla species tested without detected binding. (**c**) RBD-hFc of selected EriCoV strains binding (green) to HEK293T cells transiently expressing the indicated APN orthologs. (**d**) Entry of FR7137 and MO1 pseudoviruses into HEK293T cells transiently expressing indicated APN orthologs. PSVs were pretreated with 1.25 mg/mL trypsin. (**e**) Structural model of human APN with four domains highlighted in different colors. (**f-g**) Immunofluorescence (f) and flow cytometry (g) analyses of the indicated EriCoV RBD-hFc binding to HEK293T cells transiently expressing APN chimeras with domain swaps between human and *E.amu* APNs. Dashed lines: background threshold. Data shown are the mean of three technical repeats. (**h**) Schematic illustration of *E.amu* APN chimeras with equivalent residues from hAPN. Secondary structures and their surface localization of β16 and α2 in domain 2 (D2) were illustrated. (**i-j**) Fine mapping of the host range determinant restricting hAPN binding with RBD-hFc from RU15-1 and MO1. Chimeras exhibiting notable phenotypic changes are highlighted in red. (**k**) Sequence logo plot displaying the polymorphisms across APN orthologs. Key secondary structures and critical residues involved in host range determination were marked with red dots. APN expression (red signal in c,f,i, and j) was validated via immunofluorescence targeting the C-terminal FLAG tag. Data are presented as mean ± SD for d. N-319 glycosylation sequon is labeled with Ψ in panels h and k. Statistical significance was determined by unpaired two-tailed *t* tests (n=3 biological replicates). *: $P<0.05$, **: $P<0.01$, ***: $P<0.005$, and ****: $P<0.001$, NS: not significant. Scale bars: 100 μm for panels b, c, f, i, and j.

Structure basis of *E.amu* APN recognition by EriCoV

To elucidate the molecular basis underlying *E.amu* APN recognition, we determined several cryo-EM structures related to EriCoV and its RBDs in complex with hedgehog APN. We first determined the structure of the RU15-1 apo Spike. Cryo-EM analysis revealed that all RBDs adopt the "down" conformation (Extended Data Fig. 5a). This conformation is stabilized by an interaction network formed between glycans and neighboring protein surfaces: the N387 glycan on the RBD forms a hydrogen bond with N255 on the adjacent NTD, the N399 glycan on the RBD interacts with D527 on a neighboring RBD, and the N159 glycan on the NTD forms a hydrogen bond with S517 on the adjacent RBD. Collectively, these glycan–protein interactions lock the apo Spike in the "down" state (Extended Data Fig. 5b). A similar phenomenon has also been observed in other animal-derived apo spikes within the *Merbecovirus* subgenus, including HKU5, HKU25, and PDF-2180 (Extended Data Fig. 5c). Since all RBDs of RU15-1 apo Spike are in "closed" conformation, we ultimately chose RU15-1 RBD and *E.amu* APN for structural analysis.

To maintain the conformational uniformity of *E.amu* APN, 1 mM amastatin was added during sample preparation of the *E.amu* APN–RU15-1 complex, ensuring that all *E.amu* APN particles adopted a "closed" conformation. A total of 3,559 micrographs were collected, from which 443,002 particles were extracted and subjected to 2D classification. Approximately 38% of these particles corresponded to the target complex, containing two RU15-1 RBDs bound to opposite sides of the *E.amu* APN dimer. To further improve the local interface between the RU15-1 RBD and *E.amu* APN, symmetry expansion followed by local refinement was performed, yielding a final resolution of 3.38 Å for the *E.amu* APN monomer in complex with the RU15-1 RBD (Fig. 4a and Extended Data Fig. 6a).

At the binding interface, the RBM of RU15-1 engages *E.amu* APN primarily through a combination of hydrophobic and polar interactions. Specifically, RU15-1 RBD residues Y539, Y528, F529, A526, and P523 collectively form a hydrophobic pocket together with *E.amu* APN residues P286, A283, L309, P314, F415, P418, and H419, contributing significantly to the binding affinity of the complex. In addition, Y539 and R522 on RU15-1 RBD form hydrogen bonds with backbone atoms of *E.amu* APN residues K310 and F415, respectively, thereby reinforcing local binding stability. Furthermore, G530 and G535 of RU15-1 establish additional hydrogen bonds with K310 and N362 glycan of *E.amu* APN, respectively, establishing an extensive interaction network that underpins specific recognition of *E.amu* APN by RU15-1 (Fig. 4b).

Three distinct APN-binding modes have been reported among coronaviruses. Within the *Alphacoronavirus* genus, tegacoviruses TGEV, PRCV, CCoV-HuPn-2018, and FCoV-23 share a common binding mode, while HCoV-229E adopts a different one[62,63,75–77]. The deltacoronavirus PDCoV[55] also utilizes a distinct binding mode, featured by a slightly shifted binding orientation and footprint compared with tegacoviruses. (Fig. 4c and Extended Data Fig. 6b). Our cryo-EM reconstruction reveals that *betacoronavirus* EriCoV RBD binds to APN in a manner distinct from all previously known APN-using coronaviruses. Unlike the vertical binding orientations of tegacoviruses and PDCoV, or the configuration of 229E, the EriCoV RBD binds APN in a laterally shifted orientation. Mapping the binding footprints of the four binding modes onto the APN structure showed that RU15-1 engages a previously uncharacterized region in the central portion of domain 2. Despite variations, all four RBDs engage domain 2, along with varying contributions from domains 1 and 4 (Fig. 4d and Extended Data Fig. 6b). This convergent usage of APN resembles the varying receptor-

binding strategies observed for SARS-CoV-1, SARS-CoV-2, HCoV-NL63, NeoCoV, MOW15-22, and HKU5, all of which utilize ACE2 as their entry receptor[1,2,5–7,57,59,78].(Fig. 4d).

Structural comparison of the EriCoV–*E.amu* APN complex with NeoCoV–*P.pip* ACE2 and MERS-CoV–hDPP4 complexes revealed that all three merbecoviruses utilize the same side of their RBM—primarily the β-sheet surface—to engage their respective receptors (Fig. 4e). However, distinct indel patterns in the MERS-CoV RBM, as compared with the other two viruses, lead to conformational remodeling at the RBM tip, driving a shift in receptor specificity. Although EriCoV shares a similar RBM conformation with NeoCoV, multiple sequence differences at critical contact sites result in divergent receptor usage.

We then examined the molecular mechanisms of receptor species tropism from a structural perspective. In agreement with our functional data based on human and feline APN orthologs, all residues identified as critical for host range determination are situated in or around the RU15-1 RBD footprint, with some of them directly contributing to the RBD interaction, such as A283, P286, and K310 (corresponding to N319 in hAPN) (Fig. 4f). To assess residue-level contributions, we examined representative mutations at eight APN sites within the interface. A283K, P286S, and K310N markedly reduced RU15-1 binding (Fig. 4g), consistent with structural predictions that these substitutions introduce steric clashes (A283K and K310N) or disrupt hydrophobic contacts (P286S) (Extended Data Fig. 6c). As expected, replacing the entire hAPN region 288–331 with the *E.amu* APN counterpart (residues 279–322) conferred RU15-1 RBD binding (Extended Data Fig. 7a). To define key residues restricting hAPN receptor function, we performed PPI2 predictions to evaluate mutation combinations predicted to yield greater reductions in binding free energy (Extended Data Fig. 7b). Functional validation showed that at least five mutations within the interface, or six mutations within residues 288–331, are sufficient to convert hAPN into a functional receptor for RU15-1 and MO1 (Extended Data Fig. 7c).

To evaluate how RBM polymorphisms influence receptor recognition, we generated a sequence logo plot of 22 EriCoV RBMs. Most residues critical for *E.amu* APN interaction are highly conserved (Extended Data Fig. 7d). However, the position of $R522_{RU15\text{-}1}$ displays notable variability, featuring substitutions with distinct physicochemical properties. To explore the functional consequences of these variations, we generated several constructs with residue swaps at this site. Viral antigen binding assay revealed that R at this position confers higher binding affinity to *E.amu* APN compared to W and L, underscoring the role of EriCoV RBM polymorphism in modulating receptor binding affinity and probably ortholog specificity (Extended Data Fig. 7e).

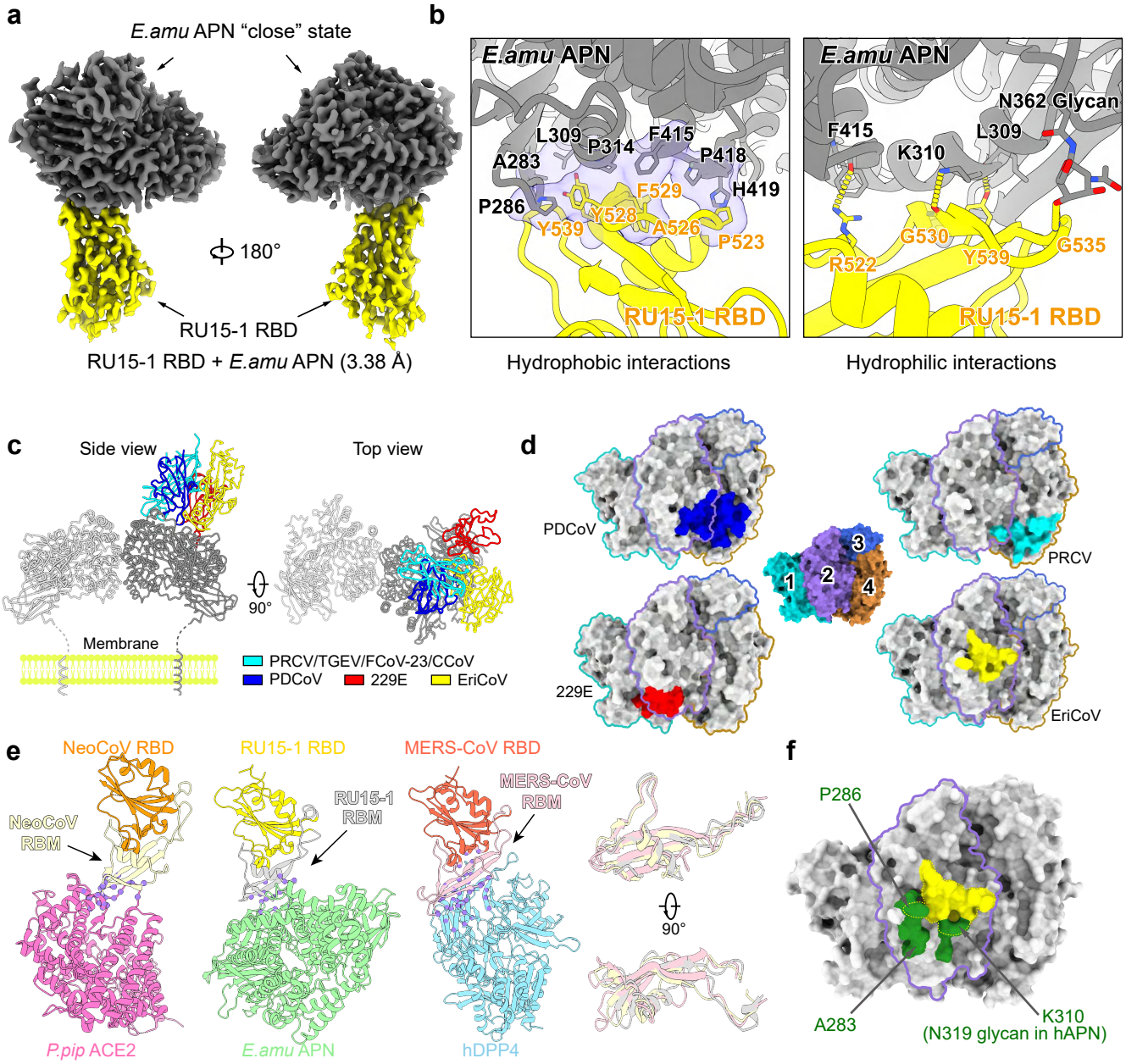

a
E.amu APN "close" state
180°
RU15-1 RBD
RU15-1 RBD + E.amu APN (3.38 Å)
b
E.amu APN
L309
P314
F415
P418
A283
F529
H419
P286
Y528
Y539
A526
P523
RU15-1 RBD
Hydrophobic interactions
E.amu APN
N362 Glycan
F415
L309
K310
G530
G535
R522
Y539
RU15-1 RBD
Hydrophilic interactions
c
Side view
Top view
90°
Membrane
PRCV/TGEV/FCoV-23/CCoV
PDCoV
229E
EriCoV
d
PDCoV
PRCV
229E
EriCoV
1
2
3
4
e
NeoCoV RBD
RU15-1 RBD
MERS-CoV RBD
NeoCoV RBM
RU15-1 RBM
MERS-CoV RBM
90°
P.pip ACE2
E.amu APN
hDPP4
f
P286
A283
K310
(N319 glycan in hAPN)
g
E.amu APN mutants
N282E
A283K
V284Q
T285A
P286S
K310N
T317N
Q321G
E.amu
hAPN
FLAG
RU15-1
MO1

Fig. 4 | Cryo-EM structures of RU15-1 RBD and in complex with *E.amu* APN. (**a**) The overall structure of the EriCoV RU15-1 RBD–*E.amu* APN complex. The RU15-1 RBD and *E.amu* APN are colored yellow and gray, respectively. (**b**) Interaction details between RU15-1 RBD and *E.amu* APN. Structures are shown as cartoon representations with key residues rendered as sticks. The hydrophobic pocket and hydrogen bonds are shown as a blue shadow with semi-transparency and yellow dashed lines, respectively. (**c**) Comparison of four distinct APN-binding modes used by the indicated coronaviruses, shown in both side and top views. PRCV (PDB: 4F5C), TGEV (PDB: 8Z27), FCoV-23 (PDB: 9DAZ), and CCoV-HuPn-2018 (PDB: 7U0L) share a common binding mode, and only PRCV is shown as a representative. RBDs of PDCoV (PDB: 7VPP), HCoV-229E (PDB: 8WDE), and EriCoV (RU15-1) (this study) are shown in blue, red, and yellow, respectively. Only hAPN dimmer is shown for clarity, with individual monomers colored in silver and gray, respectively. (**d**) RBD footprints of four representative APN-using coronaviruses mapped onto APN surfaces. APN structures are color-coded: domain 1 in dark turquoise, domain 2 in medium purple, domain 3 in royal blue, and domain 4 in dark goldenrod. RBD footprints follow the same color scheme as panel c. (**e**) Structural comparison of three merbecovirus binding modes with distinct receptors: NeoCoV–*P.pip* ACE2 (PDB: 7WPO), EriCoV–*E.amu* APN (PDB: 9W6D) and MERS-CoV–hDPP4 (PDB: 4KR0). Right: Zoomed-in view showing the superimposed RBMs from each virus. All structures are shown in cartoon representation. The *P.pip* ACE2, *E.amu* APN, and hDPP4 are colored hot pink, light green, and sky blue, respectively. The RBDs of NeoCoV, EriCoV, and MERS-CoV are colored dark orange, gold, and tomato, respectively, with their corresponding RBMs highlighted in wheat, silver, and light pink. (**f**) Summary of the host range determinants (green) identified in this study and RU15-1 RBD binding interface (yellow dashed line) mapped onto *E.amu* APN surface. Residue positions in secondary structures are indicated; domain 2 is outlined in purple. (**g**) RU15-1 and MO1 RBD-hFc binding (green) to HEK293T cells transiently expressing wild-type or mutant *E.amu* APN, assessed by immunofluorescence using an anti-hFc antibody. Scale bars: 100 μm.

EriCoV spike proteolytic activation

As indicated by our earlier pseudovirus entry data (e.g., Fig. 2i), EriCoV pseudovirus entry in HEK293T cells is highly dependent on trypsin treatment—a method commonly used to facilitate S protein activation via proteolytic cleavage[79–81]. Analysis of S protein incorporation in selected EriCoV pseudovirus particles revealed inefficient proteolytic processing during particle biogenesis, similar to what has been reported for NeoCoV[1] (Fig. 5a).

To investigate the role of host proteases in EriCoV entry and their cooperation with the receptor, we first assessed the impact of hTMPRSS2 or *E.amu* TMPRSS2 overexpression on pseudovirus entry without exogenous trypsin. Under this condition, pseudovirus entry of RU15-1 and MO1 was undetectable in HEK293T cells unless *E.amu* APN was co-expressed. Although the overall efficiency is low, entry was markedly increased upon co-expression of *E.amu* TMPRSS2, whereas hTMPRSS2 weakly enhanced entry, either with or without trypsin treatment (Fig. 5b,c). Notably, hAPN failed to support detectable entry even in the presence of *E.amu* TMPRSS2, and that *E.amu* TMPRSS2 functions in a receptor-dependent manner.

To determine whether this phenotype was specific to RU15-1 and MO1, we evaluated pseudoviruses of additional EriCoV strains. Since many strains showed lower infectivity, the pseudoviral particles were pre-treated with trypsin, followed by enzymatic inactivation before and during infection by 10% FBS. In HEK293T cells transiently expressing the different combinations of *E.amu* APN and *E.amu* TMPRSS2, all strains displayed similar dependence on APN and TMPRSS2 co-expression for more efficient entry, although at varying efficiencies (Fig. 5d). Protease inhibition assay indicates that EriCoV entry can be inhibited by cathepsin B/L inhibitor E64d[57,82] in 293T cells, but also becomes sensitive to TMPRSS2 inhibitor Camostat[57] once *E.amu* TMPRSS2 is co-expressed (Fig. 5e and Extended Data Fig. 8a).

To further assess S-mediated viral propagation, we generated replication-competent VSV (rcVSV) encoding the S glycoproteins of IT5-12, RU15-1, or MO1[1,5,7] (Extended Data Fig. 8b). Viral amplification was observed in Caco-2 cells expressing *E.amu* APN and can be boosted with trypsin treatment (Extended Data Fig. 8c). In Caco-2 cells overexpressing *E.amu* APN only, rcVSV-RU15-1 and rcVSV-MO1 propagated over time and were sensitive to the E64d, which indicates these viruses predominantly adopt the endocytosis pathway under this condition[57,82]. Co-expression of *E.amu* APN and *E.amu* TMPRSS2 supported more efficient rcVSV amplification and syncytium formation, particularly for the Asian strain MO1. Under these conditions, infection became sensitive to Camostat and less sensitive to E64d, suggesting a shift from cathepsin-dependent endocytosis to TMPRSS2-mediated plasma membrane fusion. Consistently, syncytium formation was reduced upon Camostat treatment, indicating that *E.amu* TMPRSS2 promotes cell-surface entry that bypasses the endosomal route (Fig. 5f). As a positive control, the OC43 HR2-derived fusion inhibitor EK1C4 peptide[83] potently suppressed the viral amplification under the tested conditions.

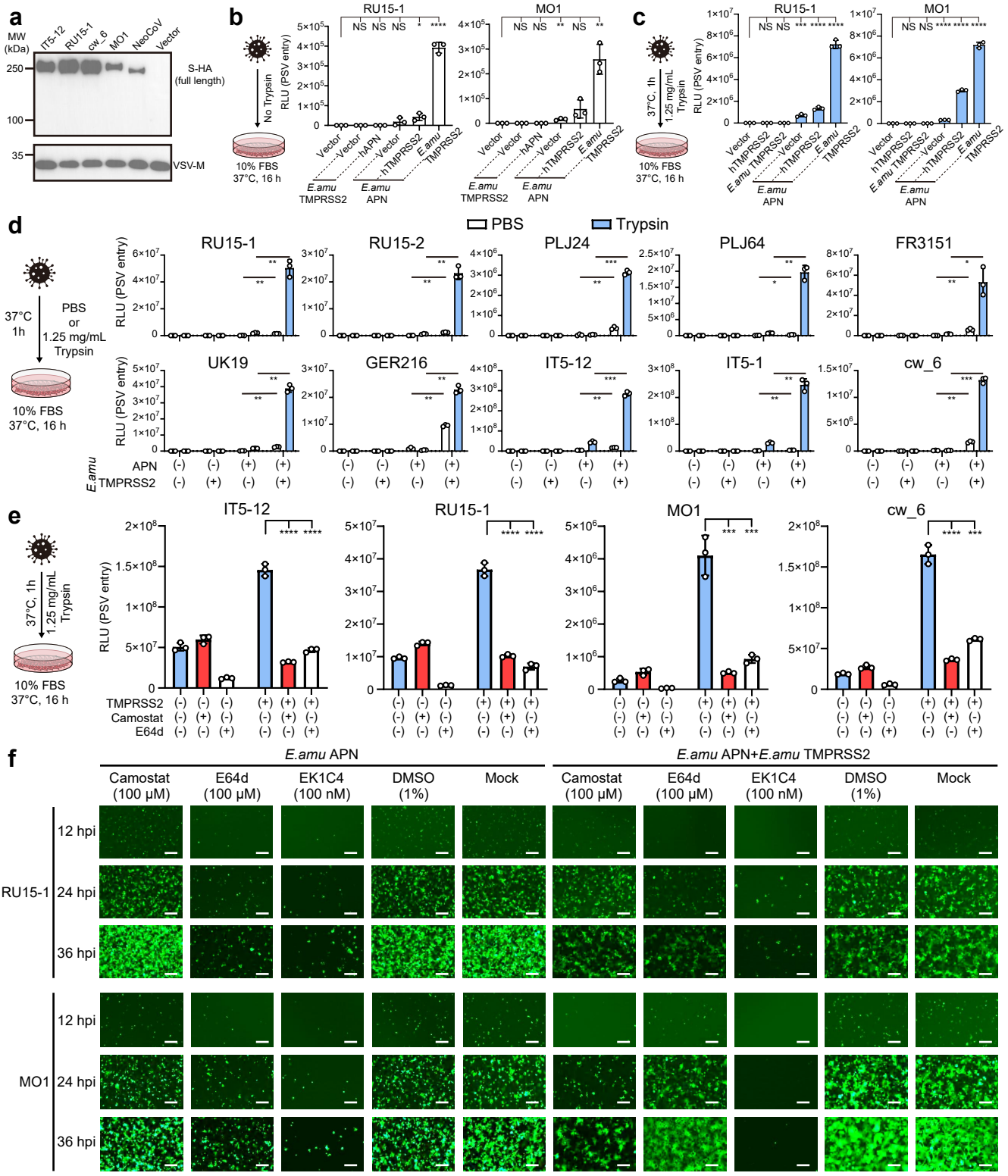

a
MW (kDa)
IT5-12
RU15-1
cw_6
MO1
NeoCoV
Vector
250
100
35
S-HA (full length)
VSV-M
b
No Trypsin
10% FBS 37°C, 16 h
RU15-1
MO1
RLU (PSV entry)
Vector
hAPN
hTMPRSS2
E.amu TMPRSS2
E.amu APN
c
37°C, 1h 1.25 mg/mL Trypsin
10% FBS 37°C, 16 h
d
PBS
Trypsin
37°C 1h
PBS or 1.25 mg/mL Trypsin
10% FBS 37°C, 16 h
RU15-1
RU15-2
PLJ24
PLJ64
FR3151
UK19
GER216
IT5-12
IT5-1
cw_6
E.amu
APN
TMPRSS2
e
37°C, 1h 1.25 mg/mL Trypsin
10% FBS 37°C, 16 h
IT5-12
RU15-1
MO1
cw_6
TMPRSS2
Camostat
E64d
f
E.amu APN
E.amu APN+E.amu TMPRSS2
Camostat (100 μM)
E64d (100 μM)
EK1C4 (100 nM)
DMSO (1%)
Mock
RU15-1
MO1
12 hpi
24 hpi
36 hpi

Fig. 5 | EriCoVs rely on hedgehog TMPRSS2 for efficient plasma membrane fusion. (**a**) Detection of EriCoV S glycoprotein in VSV pseudovirions via Western blot using an anti-HA antibody targeting the C-terminally fused HA tag. VSV-M serves as a loading control. (**b-c**) Entry of RU15-1 and MO1 pseudovirus into HEK293T cells transiently expressing the indicated APN and TMPRSS2 orthologs. Flowcharts summarize the infection conditions with PBS (b) or trypsin (c) treatment. (**d**) Entry efficiency of selected EriCoV pseudoviruses into HEK293T cells expressing the *E.amu* APN, *E.amu* TMPRSS2, or both. PSVs were pretreated with PBS or 1.25 mg/mL Trypsin, and infection was conducted in the presence of 10% FBS. (**e**) Entry of selected EriCoV pseudoviruses into HEK293T cells expressing *E.amu* APN alone or co-expressing *E.amu* APN and *E.amu* TMPRSS2 upon 100 μM Camostat or E64d treatment. PSVs were pretreated with 1.25 mg/mL Trypsin. (**f**) Propagation of rcVSV-RU15-1 and rcVSV-MO1 in Caco-2-*E.amu* APN (left) or Caco-2-*E.amu* APN-*E.amu* TMPRSS2 (right) stable cells. Data are presented as mean ± SD for b,c, and d. Statistical significance was determined using unpaired two-tailed *t* tests (n=3 biological replicates). *: $P<0.05$, **: $P<0.01$, ***: $P<0.005$, ****: $P<0.001$, and NS: not significant. Scale bars: 200 μm for panel f.

Neutralizing antibodies against EriCoV

Next, we investigated whether antibodies that block RBD–APN interaction could neutralize EriCoV entry. Mice were immunized with RBD proteins from the MO1 and RU15-1 strains, which share only 79% identity in their RBD sequences (Fig. 6a). ELISA confirmed that two immunizations elicited robust antibody responses against both the MO1 and RU15-1 RBDs (Fig. 6b). Three mice per group with the highest ELISA titers were selected for splenocyte isolation. Single B cells (7-AAD$^-$/CD19$^+$/IgM$^-$/IgD$^-$/OVA$^-$/RBD$^+$) were sorted for monoclonal antibody discovery (Extended Data Fig. 9a). In total, we obtained 54 MO1 RBD-binding antibodies and 67 RU15-1 RBD-binding antibodies (Supplementary Table 4), which were evaluated for their neutralizing activities (Fig. 6c). Among the MO1-targeting antibodies, 36 (67%) exhibited strong neutralizing activity (IC_{50}<0.1 μg/mL). In contrast, only 8 (12%) of the RU15-1-targeting antibodies displayed strong neutralizing activity, while 46 (69%) showed no neutralization.

We next examined the relationship between RBD-binding epitope and EriCoV neutralization. Epitope binning assays were performed using SPR competition for antibodies binding to both the RU15-1 or MO1 RBDs (Extended Data Fig. 9b,c). The antibodies from both groups segregated into two distinct epitope bins, only one of which correlated strongly with pseudovirus neutralization. To determine if neutralization resulted from blocking receptor engagement, we selected ten representative antibodies from each group for APN competition assays (Extended Data Fig. 9d). Recombinant RBD-hFc proteins were pre-incubated with RBD-binding antibodies and applied to HEK293T cells transiently expressing *E.amu* APN to evaluate antibody APN blockade. Antibody-mediated inhibition of APN binding correlated closely with viral neutralization (Extended Data Fig. 9d,e), underscoring the essential role of the RBD–APN interaction in EriCoV entry. Eight potent neutralizing antibodies against RU15-1 or MO1 were further validated by neutralizing assays against the amplification of rcVSV-MO1, rcVSV-RU15-1,or rcVSV-IT5-12. As expected, antibodies against European or Asian EriCoV strains potently inhibited the amplification of their corresponding lineages. Notably, two antibodies against RU15-1, BD23-0177 and BD23-0163, displayed cross-neutralization to MO1 (Fig. 6d). The pan-EriCoV activity of BD23-0177 was further confirmed by its potent inhibition of the entry of various EriCoV strains, suggesting conserved antigenicity among EriCoVs (Extended Data Fig. 9f).

To elucidate the neutralization mechanisms of RBD-specific antibodies, we selected one neutralizing and one non-neutralizing monoclonal antibody from each immunization group for structural characterization, representing distinct epitope bins defined by SPR competition. The RU15-1 group comprised the neutralizing antibody BD23-0177 and the non-neutralizing BD23-0152, while the MO1 group comprised the neutralizing BD23-0027 and the non-neutralizing BD23-0087. Cryo-EM reconstructions of the antibody–RBD complexes reached final map resolutions of 3.84 Å (RU15-1 complexes) and 3.65 Å (MO1 complexes) (Extended Data Fig. 10a,b). BD23-0177 binds to the tip of the RU15-1 RBD, corresponding to the receptor-binding motif (RBM) region. Four hydrogen bonds form between RU15-1 residues T537, Y539, R494, and D525 and BD23-0177 residues T31 and A32 on the light chain and Y32 and N56 on the heavy chain, respectively. Additional hydrophobic interactions involving BD23-0177 residues Y32, Y99, V98, and V102 on the heavy chain and H91 and A32 on the light chain, together with RU15-1 residues Y528 and Y539, form a large hydrophobic pocket that stabilizes the complex. Notably, this epitope extensively overlaps with the *E.amu* APN binding site, resulting in steric hindrance and thereby conferring neutralizing activity of BD23-0177 (Fig. 6e-g). By contrast, structural analysis of MO1 RBD in complex with its two

antibodies revealed that the neutralizing antibody BD23-0027 does not target the canonical RBM. Instead, BD23-0027 recognizes an epitope at the rear-left side of the MO1 RBD tip. At the interface, the heavy and light chains of BD23-0027 form an extensive hydrophobic pocket comprising 12 hydrophobic residues, supported by a dense hydrogen-bonding network. For example, MO1 RBD residues D499, H536, N534, and Q506 form hydrogen bonds with BD23-0027 heavy chain residues Y52, N33, Y104, and N100, respectively. Mechanistically, BD23-0027 appears to exert its neutralizing effect by inducing steric clashes with the *E.amu* APN N362 glycan, thereby preventing its approach to the MO1 RBD (Extended Data Fig. 11a-c).

In pseudovirus neutralization assays, BD23-0177 exhibited cross-neutralizing activity against both RU15-1 and MO1, identifying it as a broadly neutralizing antibody. Structural comparison of the RU15-1 and MO1 complexes revealed that BD23-0177 targets a relatively conserved region shared between the two RBDs. Among the 14 RU15-1 residues interacting with BD23-0177 within 4 Å, 11 are conserved, yielding a conservation rate of 78%. In contrast, only 8 of the 14 interacting residues in the MO1 RBD are conserved. These findings provide a molecular explanation for the broad neutralization capacity of BD23-0177 and highlight its potential as a therapeutic antibody candidate, offering a solid structural foundation for future antibody-based drug development (Extended Data Fig. 11d,e).

To further investigate whether antibodies targeting APN could block infection, mice were immunized intramuscularly with *E.amu* APN mRNA, followed by a booster injection with mRNA with incomplete Freund's adjuvant (IFA) on Day 35 (Fig. 6h). Spleens were harvested on Day 40, and *E.amu* APN-specific single B cells were sorted. In total,83 *E.amu* APN-binding antibodies were obtained (Supplementary Table 4), over half of which displayed strong neutralization activity against EriCoV pseudovirus entry in HEK293T-*E.amu* APN cells (Fig. 6i). Two neutralizing antibodies (BD24-0134 and BD24-0154) and one non-neutralizing antibody (BD24-0131) were selected for further analysis in different infection systems. All three are *E.amu* APN-specific and do not cross with hAPN (Extended Data Fig. 12a). Entry and propagation assays demonstrated that the neutralizing antibodies efficiently blocked RU15-1 and MO1 infection in different cells, including HEK293T cells overexpressing APN from the African pygmy hedgehog (*A.alb*) (Extended Data Fig. 12b,c). As Amur hedgehog cells are unavailable, African pygmy hedgehog cells were used as a surrogate model to examine the role of endogenous APN. Although we failed to culture lung and intestinal cells or generate organoids for infection assay, primary kidney cells were successfully isolated and cultured, and supported EriCoV (MO1) pseudovirus entry. Entry of EriCoV pseudovirus, but not the VSV-G pseudovirus control, was effectively inhibited by the neutralizing *E.amu* APN antibodies, confirming the essential role of endogenous APN for EriCoV entry (Fig. 6j, and Extended Data Fig. 12d,e).

Together, these neutralizing antibodies represent promising therapeutic candidates for pandemic preparedness against potential future EriCoV spillover events. This is particularly relevant given that population immunity from SARS-CoV-2 infection and vaccination history shows negligible neutralizing activity against EriCoV (Extended Data Fig. 12f and Supplementary Table 5).

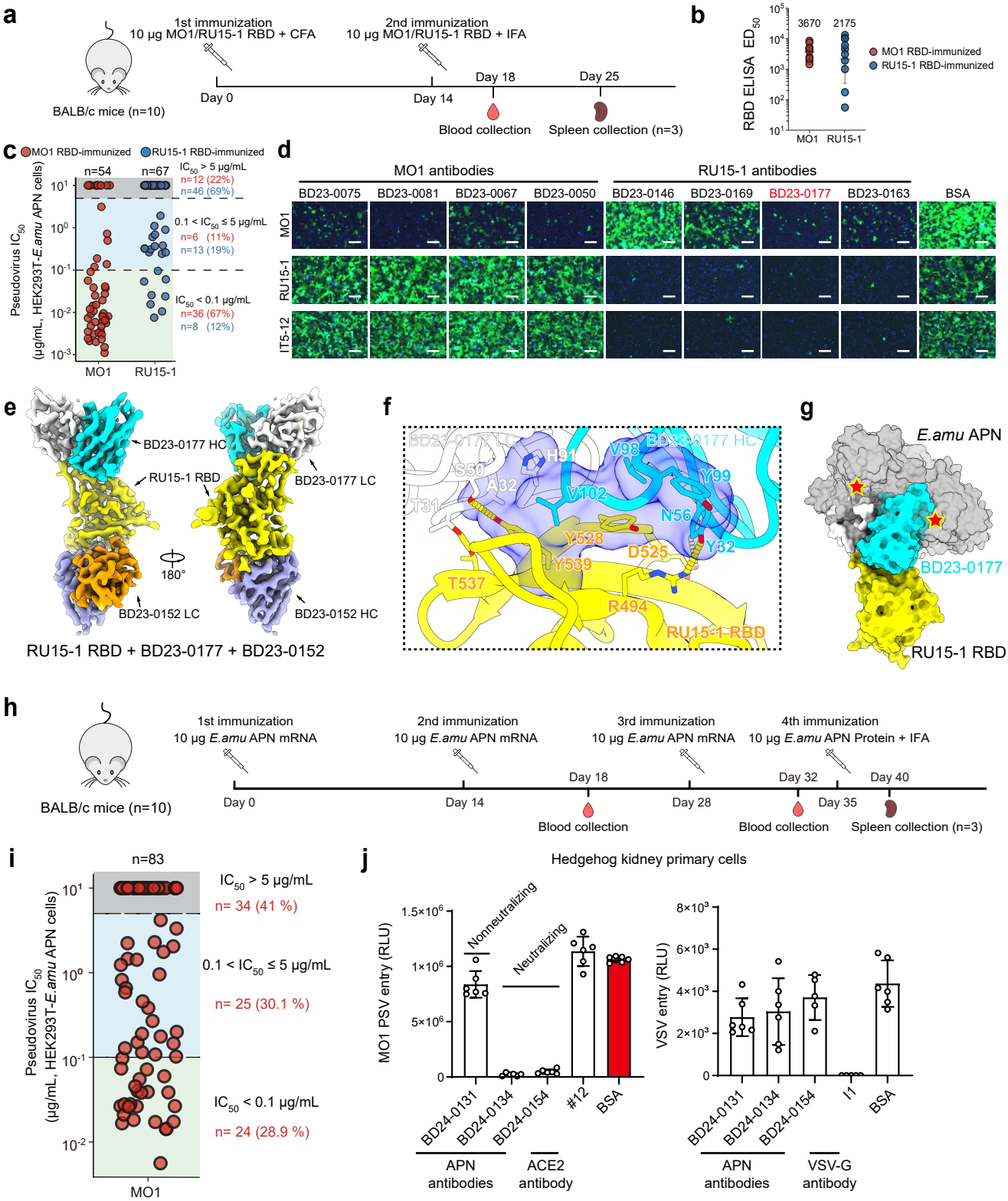

a
1st immunization
10 μg MO1/RU15-1 RBD + CFA
2nd immunization
10 μg MO1/RU15-1 RBD + IFA
BALB/c mice (n=10)
Day 0
Day 14
Day 18
Day 25
Blood collection
Spleen collection (n=3)
b
RBD ELISA ED50
3670
2175
MO1 RBD-immunized
RU15-1 RBD-immunized
MO1
RU15-1
c
MO1 RBD-immunized
RU15-1 RBD-immunized
Pseudovirus IC50 (μg/mL, HEK293T-E.amu APN cells)
n=54
n=67
IC50 > 5 μg/mL
n=12 (22%)
n=46 (69%)
0.1 < IC50 ≤ 5 μg/mL
n=6 (11%)
n=13 (19%)
IC50 < 0.1 μg/mL
n=36 (67%)
n=8 (12%)
MO1
RU15-1
d
MO1 antibodies
RU15-1 antibodies
BD23-0075
BD23-0081
BD23-0067
BD23-0050
BD23-0146
BD23-0169
BD23-0177
BD23-0163
BSA
MO1
RU15-1
IT5-12
e
BD23-0177 HC
RU15-1 RBD
BD23-0177 LC
180°
BD23-0152 LC
BD23-0152 HC
RU15-1 RBD + BD23-0177 + BD23-0152
f
BD23-0177 LC
BD23-0177 HC
H91
V98
S50
A32
Y99
T31
V102
N56
Y528
D525
Y32
Y539
T537
R494
RU15-1-RBD
g
E.amu APN
BD23-0177
RU15-1 RBD
h
BALB/c mice (n=10)
1st immunization
10 μg E.amu APN mRNA
2nd immunization
10 μg E.amu APN mRNA
3rd immunization
10 μg E.amu APN mRNA
4th immunization
10 μg E.amu APN Protein + IFA
Day 0
Day 14
Day 18
Day 28
Day 32
Day 35
Day 40
Blood collection
Blood collection
Spleen collection (n=3)
i
n=83
Pseudovirus IC50 (μg/mL, HEK293T-E.amu APN cells)
IC50 > 5 μg/mL
n= 34 (41 %)
0.1 < IC50 ≤ 5 μg/mL
n= 25 (30.1 %)
IC50 < 0.1 μg/mL
n= 24 (28.9 %)
MO1
j
Hedgehog kidney primary cells
MO1 PSV entry (RLU)
Nonneutralizing
Neutralizing
BD24-0131
BD24-0134
BD24-0154
#12
BSA
APN antibodies
ACE2 antibody
VSV entry (RLU)
BD24-0131
BD24-0134
BD24-0154
I1
BSA
APN antibodies
VSV-G antibody

Fig. 6 | Neutralizing antibodies efficiently block EriCoV S-mediated entry. (**a**) Schematic of EriCoV RBD immunization in mice (n=10 per group). (**b**) ELISA analyses of serum samples from immunized mice. ED_{50} values were calculated using four-parameter logistic regression. Geometric mean titers (GMT), fold changes, and statistical significance were determined by two-tailed *t* test and are shown above each group. (**c**) Pseudovirus IC_{50} values of monoclonal antibodies (mAbs) derived from MO1 (red circles, n=54) or RU15-1 (blue circles, n=67) immunization groups, categorized by potency. Neutralization assays were performed in HEK293T-*E.amu* APN cells using pseudoviruses corresponding to the respective immunogens. (**d**) Inhibition of rcVSV-EriCoV-S propagation by RU15-1 or MO1-targeting neutralizing antibodies (10 μg/mL) in Caco-2 cells stably expressing the *E.amu* APN and *E.amu* TMPRSS2. (**e-g**) Cryo-EM structures of RU15-1 RBDs in complex with Fabs. (e) The overall structures of the EriCoV RU15-1 RBD bound to BD23-0177 and BD23-0152. (f) The interaction details of RU15-1 RBD bound to BD23-0177. The hydrophobic pocket and hydrogen bonds are colored semi-transparent blue and yellow dash line, respectively. (g) The structural basis of the neutralization mechanism of antibodies BD23-0177. (**h**) Schematic of *E.amu* APN immunization in mice (n=10). (**i**) Pseudovirus IC_{50} values of mAbs derived from *E.amu* APN-immunized mice, categorized by potency. Neutralization assays were performed in HEK293T-*E.amu* APN cells using MO1 pseudoviruses. (**j**). VSV-G assembled pseudovirus served as a virus control, which can be neutralized by an I1 antibody (anti-VSV-G). Mean ± SD for j. BSA: 10 μg/mL Bovine serum albumin for d and j. Scale bars: 200 μm for d. RLU, relative light units.

Discussion

Coronaviruses circulating in wildlife continue to pose a significant threat of future pandemics[84,85]. Predicting the cross-species transmission potential of specific coronavirus strains remains challenging due to limited knowledge of their host entry and transmission mechanisms. EriCoVs as relatives of MERS-CoV have been known for over a decade and are now known to be genetically diverse and widely distributed[31,39]. Unlike bats, which generally inhabit areas distant from human populations, hedgehogs often interact with humans as urban wildlife or pets[86]. As important members of the merbecovirus subgenus associated with potential high pathogenicity, EriCoVs remain poorly characterized in terms of their spillover risks. A key obstacle to this understanding is the lack of receptor information, which hinders cross-species risk assessment, viral isolation, pathogenesis studies, and the development of countermeasures.

DPP4 was first identified in 2013 as a functional receptor for MERS-CoV[46] and later considered the canonical receptor for merbecoviruses, especially after the identification of more DPP4-using HKU4-related viruses[22,70]. However, many merbecoviruses appear unable to use DPP4 orthologs from either humans or their host species[1,6,32,81]. A decade later, the identification of ACE2-using NeoCoV and others indicates that ACE2 is also an important receptor in mediating merbecovirus entry[1,69]. Subsequent discoveries of two additional independently acquired interaction modes have established ACE2 as another major receptor in this subgenus[5–7,30,58,59,8760]. With most merbecovirus receptor usage now defined, EriCoV remained the last unresolved lineage. Notably, while EriCoV shows certain homology and similar insertion/deletion patterns with ACE2-using NeoCoV, these viruses do not appear to use ACE2[1,6]. Some studies proposed that DPP4 may serve as an alternative receptor for EriCoVs through *in silico* protein docking simulations; however, no functional evidence supported this hypothesis[39].

Our study identifies APN as a functional receptor for EriCoVs, unexpectedly expanding APN usage to the betacoronavirus genus. APN was initially identified as a receptor for two alphacoronaviruses[48,49], each engaging it through distinct binding modes[62,76,77]. More recently, deltacoronaviruses like PDCoV and avian CoVs were also shown to use APN via a third binding mode[55]. Our findings add a fourth APN-binding mode, in which EriCoV binds to APN through a uniquely oriented RBD with a distinct footprint that evolved independently. This finding underscores the remarkable plasticity of coronavirus RBDs in adapting to diverse receptor surfaces[7] and illustrates the limitations of predictive modeling, as even minor sequence changes can dramatically alter receptor usage of coronaviruses[70].

The convergent utilization of APN by EriCoVs is reminiscent of the multiple independent acquisitions of ACE2 usage among coronaviruses[5,7,87]. These observations suggest that the acquisition of a receptor by coronaviruses is not random. Intriguingly, the three merbecovirus receptors—ACE2, DPP4, and APN—are all ectopeptidases with abundant expression on epithelial surfaces of the respiratory and gastrointestinal tracts. The repeated exploitation suggests strong evolutionary advantages, such as more efficient entry, potential for broad tissue tropism, and favorable biochemical properties for virus–receptor interaction[88].

Despite structural similarity and certain sequence homology between NeoCoV and EriCoV, their distinct receptor usage implies a receptor-switch event during their evolutionary separation. The direction and drivers of this shift remain unclear, though recombination, RBM insertions/deletions, and antigenic drift are likely contributors[71,89,90]. Given their shared indel

patterns, antigenic drift likely played a central role. In this case, adaptive mutations in multiple interacting residues are necessary to achieve entirely different receptor recognition modes[61], which aligns with their significant differences in receptor-interacting residues.

Our results show that EriCoVs are highly adapted to hedgehog APN orthologs, with limited ability to utilize APN orthologs from humans and other species, restricted by critical residues and glycosylation near the interaction interface. The strong host specialization and narrow compatibility to other APN orthologs imply a high evolutionary barrier of these viruses to zoonotic transmission under current conditions, in agreement with the conclusion of an independent study lead by Michael Letko[74]. In addition to receptor binding, other host factors like protease compatibility, replication efficiency, and immune responses may also influence host range. Notably, EriCoV exhibits modest ability to engage feline APN, raising the possibility that domestic cats could serve as intermediate hosts. Given the close human–cat association, it will be important to monitor feline populations, especially in areas with known hedgehog–human overlap, for signs of EriCoV exposure. To date, no spillover events have been reported, and most known EriCoVs have been sampled in *E.eur*, *E.amu* and *E.rou* hedgehogs. Whether these viruses infect other hedgehog species or have broader host ranges remains unclear. Our findings suggest that the African pygmy hedgehogs, a popular pet species with more frequent human contact, may also be susceptible to EriCoVs.

Thus, continued surveillance of more EriCoV strains and close monitoring of suspicious sequence changes, coupled with receptor-focused functional studies, are essential for pandemic preparedness[18,84]. Although receptor-switch is not common for coronaviruses, merbecoviruses are notable for their RBM plasticity[61,89,90], facilitating their ability to adapt human receptors for zoonotic emergence. Development of EriCoV-specific neutralizing antibodies and vaccines could provide preemptive countermeasures. Overall, our findings expand the repertoire of receptor usage within the *merbecovirus* subgenus, providing a structural and functional basis for risk assessment and countermeasure development for those viruses that could potentially pose a threat to humans or domestic animals.

Reference

1. Xiong, Q. *et al.* Close relatives of MERS-CoV in bats use ACE2 as their functional receptors. *Nature* **612**, 748–757 (2022).
2. Hofmann, H. *et al.* Human coronavirus NL63 employs the severe acute respiratory syndrome coronavirus receptor for cellular entry. *Proc Natl Acad Sci U S A* **102**, 7988–7993 (2005).
3. Li, W. *et al.* Angiotensin-converting enzyme 2 is a functional receptor for the SARS coronavirus. *Nature* **426**, 450–454 (2003).
4. Chen, J. *et al.* A bat MERS-like coronavirus circulates in pangolins and utilizes human DPP4 and host proteases for cell entry. *Cell* **186**, 850–863.e16 (2023).
5. Park, Y.-J. *et al.* Molecular basis of convergent evolution of ACE2 receptor utilization among HKU5 coronaviruses. *Cell* **188**, 1711–1728.e21 (2025).
6. Catanzaro, N. J. *et al.* ACE2 from Pipistrellus abramus bats is a receptor for HKU5 coronaviruses. *Nat Commun* **16**, 4932 (2025).
7. Ma, C.-B. *et al.* Multiple independent acquisitions of ACE2 usage in MERS-related coronaviruses. *Cell* **188**, 1693–1710.e18 (2025).
8. Guan, Y. *et al.* Isolation and characterization of viruses related to the SARS coronavirus from animals in southern China. *Science* **302**, 276–278 (2003).
9. Drosten, C. *et al.* Identification of a novel coronavirus in patients with severe acute respiratory syndrome. *N Engl J Med* **348**, 1967–1976 (2003).
10. Zaki, A. M., van Boheemen, S., Bestebroer, T. M., Osterhaus, A. D. M. E. & Fouchier, R. A. M. Isolation of a novel coronavirus from a man with pneumonia in Saudi Arabia. *N Engl J Med* **367**, 1814–1820 (2012).
11. Zhu, N. *et al.* A Novel Coronavirus from Patients with Pneumonia in China, 2019. *N Engl J Med* **382**, 727–733 (2020).
12. Zhou, P. *et al.* A pneumonia outbreak associated with a new coronavirus of probable bat origin. *Nature* **579**, 270–273 (2020).
13. Mallapaty, S. The pathogens that could spark the next pandemic. *Nature* **632**, 488 (2024).
14. Pathogens prioritization: a scientific framework for epidemic and pandemic research preparedness. https://www.who.int/publications/m/item/pathogens-prioritization-a-scientific-framework-for-epidemic-and-pandemic-research-preparedness.
15. Ngere, I. *et al.* Outbreak of Middle East Respiratory Syndrome Coronavirus in Camels and Probable Spillover Infection to Humans in Kenya. *Viruses* **14**, (2022).
16. Haagmans, B. L. *et al.* Middle East respiratory syndrome coronavirus in dromedary camels: an outbreak investigation. *Lancet Infect Dis* **14**, 140–145 (2014).
17. Mohd, H. A., Al-Tawfiq, J. A. & Memish, Z. A. Middle East Respiratory Syndrome Coronavirus (MERS-CoV) origin and animal reservoir. *Virol J* **13**, 87 (2016).
18. Tolentino, J. E., Lytras, S., Ito, J. & Sato, K. Beyond MERS: Merbecovirus receptor plasticity calls for emergence preparedness. *Cell Host Microbe* **33**, 453–456 (2025).
19. Cui, J., Li, F. & Shi, Z.-L. Origin and evolution of pathogenic coronaviruses. *Nat Rev Microbiol* **17**, 181–192 (2019).
20. Ithete, N. L. *et al.* Close relative of human Middle East respiratory syndrome coronavirus in bat, South Africa. *Emerg Infect Dis* **19**, 1697–1699 (2013).
21. Wang, Q. *et al.* Bat origins of MERS-CoV supported by bat coronavirus HKU4 usage of human receptor CD26. *Cell Host Microbe* **16**, 328–337 (2014).
22. Yang, Y. *et al.* Receptor usage and cell entry of bat coronavirus HKU4 provide insight into bat-to-human transmission of MERS coronavirus. *Proc Natl Acad Sci U S A* **111**, 12516–12521 (2014).

23. Corman, V. M. *et al.* Rooting the phylogenetic tree of middle East respiratory syndrome coronavirus by characterization of a conspecific virus from an African bat. *J Virol* **88**, 11297–11303 (2014).
24. Luo, C.-M. *et al.* Discovery of Novel Bat Coronaviruses in South China That Use the Same Receptor as Middle East Respiratory Syndrome Coronavirus. *J Virol* **92**, (2018).
25. Lau, S. K. P. *et al.* Receptor Usage of a Novel Bat Lineage C Betacoronavirus Reveals Evolution of Middle East Respiratory Syndrome-Related Coronavirus Spike Proteins for Human Dipeptidyl Peptidase 4 Binding. *J Infect Dis* **218**, 197–207 (2018).
26. Alagaili, A. N. *et al.* Middle East respiratory syndrome coronavirus infection in dromedary camels in Saudi Arabia. *mBio* **5**, e00884–14 (2014).
27. Meyer, B. *et al.* Antibodies against MERS coronavirus in dromedary camels, United Arab Emirates, 2003 and 2013. *Emerg Infect Dis* **20**, 552–559 (2014).
28. Azhar, E. I. *et al.* Evidence for camel-to-human transmission of MERS coronavirus. *N Engl J Med* **370**, 2499–2505 (2014).
29. Xia, L.-Y. *et al.* Isolation and characterization of a pangolin-borne HKU4-related coronavirus that potentially infects human-DPP4-transgenic mice. *Nat Commun* **15**, 1048 (2024).
30. Wang, N. *et al.* A MERS-CoV-like mink coronavirus uses ACE2 as an entry receptor. *Nature* **642**, 739–746 (2025).
31. Corman, V. M. *et al.* Characterization of a novel betacoronavirus related to middle East respiratory syndrome coronavirus in European hedgehogs. *J Virol* **88**, 717–724 (2014).
32. Lau, S. K. P. *et al.* Identification of a Novel Betacoronavirus () in Amur Hedgehogs from China. *Viruses* **11**, (2019).
33. Beissat, K. *et al.* Coding-complete genome sequences of hedgehog coronavirus isolated from in France. *Microbiol Resour Announc* **14**, e0015725 (2025).
34. Saldanha, I. F. *et al.* Extension of the known distribution of a novel clade C betacoronavirus in a wildlife host. *Epidemiol Infect* **147**, e169 (2019).
35. De Sabato, L. *et al.* Can Coronaviruses Steal Genes from the Host as Evidenced in Western European Hedgehogs by EriCoV Genetic Characterization? *Viruses* **12**, (2020).
36. Delogu, M. *et al.* Eco-Virological Preliminary Study of Potentially Emerging Pathogens in Hedgehogs () Recovered at a Wildlife Treatment and Rehabilitation Center in Northern Italy. *Animals (Basel)* **10**, (2020).
37. Domanska-Blicharz, K. *et al.* Whole genome characteristics of hedgehog coronaviruses from Poland and analysis of the evolution of the Spike protein for its interspecies transmission potential. *BMC Vet Res* **20**, 424 (2024).
38. Pomorska-Mól, M., Ruszkowski, J. J., Gogulski, M. & Domanska-Blicharz, K. First detection of Hedgehog coronavirus 1 in Poland. *Sci Rep* **12**, 2386 (2022).
39. Cruz, A. V. S. *et al.* Genomic characterization and cross-species transmission potential of hedgehog coronavirus. *One Health* **19**, 100940 (2024).
40. Lukina-Gronskaya, A. V. *et al.* Novel coronaviruses and mammarenaviruses of hedgehogs from Russia including the comparison of viral communities of hibernating and active specimens. *Front Vet Sci* **11**, 1486635 (2024).
41. He, W.-T. *et al.* Virome characterization of game animals in China reveals a spectrum of emerging pathogens. *Cell* **185**, 1117–1129.e8 (2022).
42. Li, D. *et al.* MERS-related CoVs in hedgehogs from Hubei Province, China. *One Health* **13**, 100332 (2021).
43. Lu, G., Wang, Q. & Gao, G. F. Bat-to-human: spike features determining ‘host jump’ of coronaviruses SARS-CoV, MERS-CoV, and beyond. *Trends Microbiol.* **23**, 468–478

(2015).
44. Dveksler, G. S. *et al.* Cloning of the mouse hepatitis virus (MHV) receptor: expression in human and hamster cell lines confers susceptibility to MHV. *J Virol* **65**, 6881–6891 (1991).
45. Williams, R. K., Jiang, G. S. & Holmes, K. V. Receptor for mouse hepatitis virus is a member of the carcinoembryonic antigen family of glycoproteins. *Proc Natl Acad Sci U S A* **88**, 5533–5536 (1991).
46. Raj, V. S. *et al.* Dipeptidyl peptidase 4 is a functional receptor for the emerging human coronavirus-EMC. *Nature* **495**, 251–254 (2013).
47. Niaz, K. & Nisar, M. F. *Coronavirus Disease-19 (COVID-19): A Perspective of New Scenario*. (Bentham Science Publishers, 2021).
48. Yeager, C. L. *et al.* Human aminopeptidase N is a receptor for human coronavirus 229E. *Nature* **357**, 420–422 (1992).
49. Delmas, B. *et al.* Aminopeptidase N is a major receptor for the entero-pathogenic coronavirus TGEV. *Nature* **357**, 417–420 (1992).
50. Wang, H. *et al.* TMPRSS2 and glycan receptors synergistically facilitate coronavirus entry. *Cell* **187**, 4261–4271.e17 (2024).
51. McCallum, M. *et al.* Human coronavirus HKU1 recognition of the TMPRSS2 host receptor. *Cell* **187**, 4231–4245.e13 (2024).
52. Fernández, I. *et al.* Structural basis of TMPRSS2 zymogen activation and recognition by the HKU1 seasonal coronavirus. *Cell* **187**, 4246–4260.e16 (2024).
53. Saunders, N. *et al.* TMPRSS2 is a functional receptor for human coronavirus HKU1. *Nature* **624**, 207–214 (2023).
54. Dufloo, J. *et al.* Dipeptidase 1 is a functional receptor for a porcine coronavirus. *Nat Microbiol* **10**, 2981–2996 (2025).
55. Ji, W. *et al.* Structures of a deltacoronavirus spike protein bound to porcine and human receptors. *Nat Commun* **13**, 1467 (2022).
56. Walls, A. C. *et al.* Structure, Function, and Antigenicity of the SARS-CoV-2 Spike Glycoprotein. *Cell* **181**, 281–292.e6 (2020).
57. Hoffmann, M. *et al.* SARS-CoV-2 Cell Entry Depends on ACE2 and TMPRSS2 and Is Blocked by a Clinically Proven Protease Inhibitor. *Cell* **181**, 271–280.e8 (2020).
58. Madel Alfajaro, M. *et al.* HKU5 bat merbecoviruses engage bat and mink ACE2 as entry receptors. *Nat Commun* **16**, 6822 (2025).
59. Chen, J. *et al.* Bat-infecting merbecovirus HKU5-CoV lineage 2 can use human ACE2 as a cell entry receptor. *Cell* **188**, 1729–1742.e16 (2025).
60. Zhang, Y. *et al.* Molecular insights into species-specific ACE2 recognition of coronavirus HKU5. *Nat Commun* **16**, 10889 (2025).
61. Liu, C. *et al.* HKU25 clade MERS-related coronaviruses use ACE2 as a functional receptor. *Nat Microbiol* **10**, 2860–2874 (2025).
62. Tortorici, M. A. *et al.* Structure, receptor recognition, and antigenicity of the human coronavirus CCoV-HuPn-2018 spike glycoprotein. *Cell* **185**, 2279–2291.e17 (2022).
63. Tortorici, M. A. *et al.* Loss of FCoV-23 spike domain 0 enhances fusogenicity and entry kinetics. *Nature* (2025) doi:10.1038/s41586-025-09155-z.
64. Li, W. *et al.* Broad receptor engagement of an emerging global coronavirus may potentiate its diverse cross-species transmissibility. *Proc Natl Acad Sci U S A* **115**, E5135–E5143 (2018).
65. Liang, Q.-Z. *et al.* Chicken or Porcine Aminopeptidase N Mediates Cellular Entry of Pseudoviruses Carrying Spike Glycoprotein from the Avian Deltacoronaviruses HKU11, HKU13, and HKU17. *J Virol* **97**, e0194722 (2023).

66. Shirato, K., Kawase, M. & Matsuyama, S. Middle East respiratory syndrome coronavirus infection mediated by the transmembrane serine protease TMPRSS2. *J Virol* **87**, 12552–12561 (2013).
67. Bertram, S. *et al.* TMPRSS2 activates the human coronavirus 229E for cathepsin-independent host cell entry and is expressed in viral target cells in the respiratory epithelium. *J Virol* **87**, 6150–6160 (2013).
68. Glowacka, I. *et al.* Evidence that TMPRSS2 activates the severe acute respiratory syndrome coronavirus spike protein for membrane fusion and reduces viral control by the humoral immune response. *J Virol* **85**, 4122–4134 (2011).
69. Ma, C. *et al.* Broad host tropism of ACE2-using MERS-related coronaviruses and determinants restricting viral recognition. *Cell Discov* **9**, 57 (2023).
70. Yuan, H. *et al.* Structures and receptor binding activities of merbecovirus spike proteins reveal key signatures for human DPP4 adaptation. *Sci Adv* **11**, eadv7296 (2025).
71. Si, J.-Y. *et al.* Sarbecovirus RBD indels and specific residues dictating multi-species ACE2 adaptiveness. *Nat Commun* **15**, 8869 (2024).
72. Wang, Y. *et al.* GSA: Genome Sequence Archive<sup/>. *Genomics Proteomics Bioinformatics* **15**, 14–18 (2017).
73. Kolb, A. F., Maile, J., Heister, A. & Siddell, S. G. Characterization of functional domains in the human coronavirus HCV 229E receptor. *J Gen Virol* **77 (Pt 10)**, 2515–2521 (1996).
74. Jin, M. *et al.* Aminopeptidase N is a receptor for hedgehog merbecoviruses. *bioRxiv* (2025) doi:10.1101/2025.09.03.674079.
75. Tian, Y. *et al.* Cross-species recognition of two porcine coronaviruses to their cellular receptor aminopeptidase N of dogs and seven other species. *PLoS Pathog* **21**, e1012836 (2025).
76. Reguera, J. *et al.* Structural bases of coronavirus attachment to host aminopeptidase N and its inhibition by neutralizing antibodies. *PLoS Pathog* **8**, e1002859 (2012).
77. Wong, A. H. M. *et al.* Receptor-binding loops in alphacoronavirus adaptation and evolution. *Nat Commun* **8**, 1735 (2017).
78. Li, F., Li, W., Farzan, M. & Harrison, S. C. Structure of SARS coronavirus spike receptor-binding domain complexed with receptor. *Science* **309**, 1864–1868 (2005).
79. Guo, H. *et al.* ACE2-Independent Bat Sarbecovirus Entry and Replication in Human and Bat Cells. *mBio* **13**, e0256622 (2022).
80. Letko, M., Marzi, A. & Munster, V. Functional assessment of cell entry and receptor usage for SARS-CoV-2 and other lineage B betacoronaviruses. *Nat Microbiol* **5**, 562–569 (2020).
81. Menachery, V. D. *et al.* Trypsin Treatment Unlocks Barrier for Zoonotic Bat Coronavirus Infection. *J Virol* **94**, (2020).
82. Riva, L. *et al.* Discovery of SARS-CoV-2 antiviral drugs through large-scale compound repurposing. *Nature* **586**, 113–119 (2020).
83. Xia, S. *et al.* Inhibition of SARS-CoV-2 (previously 2019-nCoV) infection by a highly potent pan-coronavirus fusion inhibitor targeting its spike protein that harbors a high capacity to mediate membrane fusion. *Cell Res* **30**, 343–355 (2020).
84. Jiang, S. & Wu, F. Global surveillance and countermeasures for ACE2-using MERS-related coronaviruses with spillover risk. *Cell* **188**, 1465–1468 (2025).
85. Shivaprakash, K. N., Sen, S., Paul, S., Kiesecker, J. M. & Bawa, K. S. Mammals, wildlife trade, and the next global pandemic. *Curr Biol* **31**, 3671–3677.e3 (2021).
86. Ruszkowski, J. J., Hetman, M., Turlewicz-Podbielska, H. & Pomorska-Mól, M. Hedgehogs as a Potential Source of Zoonotic Pathogens-A Review and an Update of

Knowledge. *Animals (Basel)* **11**, (2021).
87. Xiong, Q. *et al.* ACE2-using merbecoviruses: Further evidence of convergent evolution of ACE2 recognition by NeoCoV and other MERS-CoV related viruses. *Cell Insight* **3**, 100145 (2024).
88. Liu, P. *et al.* Design of customized coronavirus receptors. *Nature* **635**, 978–986 (2024).
89. Tolentino, J. E., Lytras, S., Ito, J., Holmes, E. C. & Sato, K. Recombination as an evolutionary driver of MERS-related coronavirus emergence. *Lancet Infect Dis* **24**, e546 (2024).
90. Tolentino, J. E., Lytras, S., Ito, J. & Sato, K. Recombination analysis on the receptor switching event of MERS-CoV and its close relatives: implications for the emergence of MERS-CoV. *Virol J* **21**, 84 (2024).

Methods

Cell lines and culture conditions

HEK293T (CRL-3216), Caco-2 (HTB-37), and I1-Hybridoma (CRL-2700) cells were obtained from the American Type Culture Collection (ATCC). HEK293T and Caco-2 cells were cultured in Dulbecco's Modified Eagle Medium (DMEM, Monad) supplemented with 10% fetal bovine serum (FBS; Excell), 1% penicillin-streptomycin (PS; Thermo Fisher Scientific) at 37 °C in a humidified incubator with 5% CO_2. The I1-Hybridoma cell line, which produces a neutralizing antibody against vesicular stomatitis virus glycoprotein (VSV-G), was maintained in Minimum Essential Medium (MEM) with Earle's balanced salts, 2.0 mM L-glutamine (Gibco), and 10% FBS. HEK293T or Caco-2 stable cell lines overexpressing various receptors were generated using lentivirus transduction, and then selected and maintained in growth medium with puromycin (1 μg/mL) or Zeocin (100 μg/mL).

Plasma donors

Plasma samples were collected from a random population at Beijing Ditan Hospital, Capital Medical University. All participants provided written informed consent prior to sample collection. The study was approved by the Ethics Committee of Beijing Ditan Hospital, Capital Medical University (Approval No. DTEC-KY2024-112-01). Demographic data for the plasma donors are presented in Supplementary Table 5.

Receptor sequence retrieval and assembly

The nucleic acid sequences of *E.amu* ACE2, *E.amu* DPP4, *E.amu* APN, *E.amu* TMPRSS2, and *A.alb* APN were assembled from RNA-seq raw data derived from *Erinaceus amurensis* Kidney (GSA accession ID: CRX555648), *Erinaceus amurensis* Lymph (SRA Accession: SRX13651754), or *Atelerix albiventris* kidney (GSA accession ID: CRX911825). Briefly, raw next-generation sequencing (NGS) reads were downloaded from the Genome Sequence Archive (GSA) database and Sequence Read Archive (SRA) database and processed using Cutadapt (v2.4) to remove adapters and discard reads shorter than 30 base pairs. De novo assembly was performed with MEGAHIT (v1.2.9), using a minimum contig length of 100 bp. Resulting final contigs were analyzed using Geneious (2023.0.1) and were subjected to Geneious workflows for mapping reads to the indicated reference sequences under default parameters.

Plasmids and vectors

Plasmids for expressing coronavirus receptors or their derivatives were constructed by inserting human codon-optimized coding sequences obtained through commercial synthesis into the lentiviral transfer vector (pLVX-EF1a-Puro, Genewiz) with C-terminally fused 3×FLAG tags (DYKDHD-G-DYKDHD-I-DYKDDDDK)[1]. Human TMPRSS2 and *E.amu* TMPRSS2 expressing plasmid were constructed to pLVX-EF1a-Zeocin (clone based on pLVX-EF1a-Puro with the resistance gene replaced with Zeocin) with C-terminally fused ALFA-tag (PSRLEEELRRRLTE)[91]. DNA fragments for cloning chimera or mutants were generated by overlap extension PCR or gene synthesis and verified by commercial DNA sequencing.

For pseudovirus production, human codon-optimized spike sequences of MO1 (UMO75628.1), F6 (QGA70692.1), cw_6 (QOQ34381.1), IT8-1 (QRN68024.1), IT5-19 (QRN68031.1), IT5-17 (QRN68055.1), IT5-1 (QRN68048.1), IT5-11 (QRN68066.1), IT5-12 (QRN68078.1), IT5-15 (QRN68101.1), GER216 (AGX27810.1), GER174 (YP009513010), UK19 (QCC20713.1), PTH9 (XAJ09624.1), RU15-1 (XCN28775.1), RU15-2 (XCN28786.1), PLJ24 (XAJ09723.1), PLJ64 (XAJ09735.1), FR7137 (XNJ65105.1), FR3151 (XNJ65093.1), were cloned into the

pCAGGS vector with 13-15 C-terminal residues replaced by a HA tag (YPYDVPDYA) to facilitate S incorporation[92].

Plasmids expressing recombinant proteins, including coronavirus antigens, and soluble viral receptor proteins are described as follows. For CoVs S_1/RBD-hFc fusion proteins, plasmids were constructed by inserting S_1 coding sequences from IT5-19 (residues 20-737), UK19 (residues 20-734), FR7137 (residues 20-731), FR3151 (residues 20-732); RBD coding sequences from RU15-1 (residues 366-574), MO1 (residues 366-575), PTH9 (residues 367-576), PLJ64 (residues 365-574), GER216 (residues 365-574), PLJ24 (residues 365-574), FR7137 (residues 362-571), FR3151 (residues 363-572), UK19 (residues 364-573), IT8-1 (residues 365-573), IT5-1 (residues 365-573), IT5-12 (residues 365-573), IT5-15 (residues 366-575), IT5-17 (residues 366-575), IT5-19 (residues 366-575), cw_6 (residues 366-575), F6 (residues 366-575), 229E (residues 293-434) into the pCAGGS vector containing an N-terminal CD5 secretion signal peptide (MPMGSLQPLATLYLLGMLVASVL) and C-terminal hFc-twin-strep-3×FLAG tags (WSHPQFEKGGGSGGGSGGSAWSHPQFEK-GGGRSDYKDHDGDYKDHDIDYKDDDDK) for purification and detection. For expressing soluble viral receptor proteins, plasmids were constructed by inserting ecto-domain coding sequences from *E.amu* APN (residues 60-960), human APN (residues 66-967) into the pCAGGS vector containing an N-terminal CD5 secretion signal peptide (MPMGSLQPLATLYLLGMLVASVL) and C-terminal 8×His tags for purification.

For Cryo-EM and BLI assays, DNA sequences encoding *E.amu* APN protein (residues 60–960; GenBank: XP_007516437.1) and RU15-1 RBD (residues 366–574; GenBank: XCN28775.1) were obtained from NCBI. An N-terminus CD5 signal peptide and a C-terminus His-tag were added to both constructs via PCR. These constructs were cloned into the pCAGGS mammalian expression vectors.

Primary hedgehog cells

All animal experiments related to hedgehogs were authorized by the Institutional Animal Care and Use Committee (IACUC) of the Institute of Laboratory Animal Science (ILAS), Chinese Academy of Medical Sciences (CAMS) & Peking Union Medical College (PUMC), with an approval number of BLL25006. All procedures were conducted in strict compliance with institutional and national ethical guidelines for animal welfare.

African pygmy hedgehogs (Atelerix albiventris) of 12 months were purchased from a pet shop in Beijing on October 11th, 2025. Following Virbac anesthesia and euthanasia with Tiletamine-zolazepam (Virbac), the hedgehogs were surgically dissected to collect tissues, and the primary kidney cells were isolated using the Multi Tissue Dissociation Kit 1 (Miltenyi, 130-110-201) following the manufacturer's instructions. Briefly, the tissue pieces were placed in RPMI 1640, and appropriate amounts of Enzymes A, D, and R were added sequentially. The tissue was then cut into small fragments (2–4 mm) with scissors and incubated at 37 °C with rotation for 30 min. After thorough trituration, the suspension was passed through a 70 μm cell strainer. The filtrate was collected and centrifuged (300×g, 7 min), and the supernatant was discarded. Finally, 1 mL of PBS (0.04% BSA) was added, the cells were gently resuspended, and cell viability was assessed with. Cell were attached in collagen-coated 96 well plates and cultured in a growth medium (DMEM-F-12 medium supplemented with 1× insulin-transferrin-selenium, 1× MEM nonessential amino acids, 0.1 μM hydrocortisone, 0.005 μg/mL EGF, 100 IU/mL penicillin, 100 μg/mL streptomycin, and 10% FBS.) at 37 °C before infection.

Protein expression and purification

Proteins for binding, pull-down, or flow cytometry assays were produced in HEK293T cells via transient transfection, following the manufacturer's guidelines. Supernatants were collected every 48 hours post-transfection. Twin-Strep-tagged proteins were enriched using Strep-Tactin XT 4Flow high-capacity resin (IBA, 2-5030-002), washed, and eluted with buffer BXT (100 mM Tris/HCl, pH 8.0, 150 mM NaCl, 1 mM EDTA, 50 mM biotin). Eluted proteins were concentrated, buffer-exchanged into PBS by ultrafiltration, aliquoted, and stored at −80 °C.

Protein expression and purification were conducted following the established method for Cryo-EM or BLI analysis[93,94]. Briefly, the plasmids of these proteins were transiently transfected into suspension-grown HEK293F maintained at 37 °C with 8% CO_2, rotating at 130 rpm. Supernatants were harvested 72 hours post-transfection, concentrated, and purified sequentially by Ni-NTA affinity chromatography and size-exclusion chromatography (SEC) using a Superdex 200 Increase 10/300 GL column (GE Healthcare) equilibrated with PBS buffer.

Enzyme-linked immunosorbent assay (ELISA)

ELISA plates were pre-coated with RBD protein from either strain MO1 or RU15-1 at a concentration of 1 μg/mL in 0.05 M coating buffer (Solarbio, cat. no. C1055) and incubated overnight at 4 °C. After washing, plates were blocked, followed by the addition of 100 μL serially diluted mouse serum to each well and incubation at room temperature for 30 minutes. Plates were then washed and incubated with peroxidase-conjugated AffiniPure goat anti-human IgG (H+L) (Jackson ImmunoResearch, cat. no. 109-035-003) at 0.25 μg/mL for 30 minutes at room temperature. The reaction was developed using tetramethylbenzidine (TMB) substrate (Solarbio, cat. no. PR1200) and stopped by the addition of H_2SO_4. Absorbance was measured at 450 nm using a microplate reader (Thermo Scientific, Multiskan Fc).

Animal immunization and antibody screening

All mouse immunization-related experiments were conducted in accordance with protocols approved by the Animal Welfare Ethics Committee of HFK Biologics (Approval No.: HFK-AP-20250313).

Female BALB/c mice aged 6-8 weeks were used in the experiments. Mice were immunized according to the schedule outlined in Fig. 6a. Specifically, mice in the MO1 and RU15-1 RBD protein groups were immunized via subcutaneous injection with 10 μg of purified RBD protein from either the MO1 strain or RU15-1 strain, each formulated with Freund's adjuvant. The primary immunization was administered with complete Freund's adjuvant (CFA), followed by a booster injection formulated with incomplete Freund's adjuvant (IFA) 14 days later. Blood samples were collected 4 days after the second immunization.

Mice in the *E.amu* APN group were immunized via intramuscular injection with 10 μg of *E.amu* APN mRNA on Day 0, Day 14, and Day 28, followed by a booster injection with 10 μg of purified *E.amu* APN protein formulated with incomplete Freund's adjuvant (IFA) on Day 35. Blood samples were collected 4 days after the second immunization and 4 days after the third immunization. Serum titers were determined using enzyme-linked immunosorbent assay (ELISA).

Spleens from euthanized mice were minced in RPMI 1640 medium supplemented with 5% FBS, filtered through a 100 μm mesh, and treated with 1 × RBC Lysis Buffer (eBioscience,

cat. no. 00-4333-57). After centrifugation (350 × g, 8 min), cells were resuspended in staining buffer (PBS + 2% FBS) and adjusted to a final concentration of 1 × 10^7 cells/mL. Recombinant biotinylated RBD proteins (MO1 or RU15-1 strain) or *E.amu* APN proteins were incubated with streptavidin-conjugated fluorophores (PE and APC; BioLegend) on ice for at least 30 minutes. Then H_2O was added to adjust volume, and the complexes were centrifuged at 14,000 × g for 10 minutes at 4 °C to remove aggregates. Before staining, splenocytes were incubated with TruStain FcX™ (BioLegend) for 10 minutes on ice in the dark to block Fc receptors. Antigen probes and fluorescently conjugated antibodies were then added, and cells were incubated on ice for 30 minutes in the dark. After staining, cells were washed twice with staining buffer (400 × g, 5–8 minutes) and resuspended in cold buffer. 7-AAD (eBioscience, cat. no. 00-6993-50) was added 10 minutes before flow cytometry to exclude dead cells. For cell sorting, antigen-specific B cells were defined as 7-AAD$^-$, CD19$^+$, IgM$^-$/IgD$^-$, OVA$^-$, and either MO1 RBD$^+$, RU15-1 RBD$^+$, or *E.amu* APN$^+$, depending on the immunization group. Single B cells were sorted using a MoFlo Astrios EQ Cell Sorter (Beckman Coulter) directly into 96-well PCR plates.

Sorted single B cells were lysed in buffer containing RNase inhibitor, 0.095% Triton X-100, Oligo dT primer, and dNTPs, followed by cDNA synthesis using the Vazyme R302 kit. Variable regions of heavy chains and light chains (lambda/kappa) were amplified via two-round PCR. After verification by 1% agarose gel electrophoresis and magnetic bead purification, the variable region amplicons were set aside. Separately, the human IgG1 constant region was cloned into pCMV3 vectors using homologous recombination with the ClonExpress II One Step Cloning Kit (Vazyme, cat. no. C112-02) at 37°C for 30 minutes. Variable regions were recombined into the pCMV3 vectors using the same homologous recombination method. Recombinant plasmids were transformed into DH5α competent cells (Tsingke, cat. no. TSC-C01), activated at 37°C, and plated for selection. Recombinant plasmids were transformed into DH5α competent cells (Tsingke, cat. no. TSC-C01), activated at 37°C, and plated for selection. Plasmid DNA of expanded cultures was extracted (CWBIO CW2105) after verified by the alignment results of Sanger sequencing. Protein production was carried out in Expi293F cells. Co-transfection was performed by mixing the antibody plasmids with polyethylenimine (Yeasen, 40816ES03) in 0.9% NaCl solution before adding to the cell culture. Cells were maintained under standard culture conditions. After 24 hours, 1 mL of nutrient supplement (OPM Biosciences, F081918-001) was added per culture bottle, with subsequent feedings every 48 hours during a 6–10 day culturing period. For antibody purification, supernatant containing the monoclonal antibodies was obtained by centrifugation (3,000 × g, 10 minutes). After incubation of Protein A magnetic beads (GenScript, L00695) with the supernatant for 2 hours, automated purification was achieved by using a KingFisher instrument (Thermo Fisher). Antibody concentration was measured with a NanoDrop (Thermo Fisher, 840-317400), while purity was assessed by SDS-PAGE (LabLead, P42015). Screening of monoclonal antibodies was performed using a pseudovirus neutralization assay. The antibody sequences are listed in Supplementary Table 4.

SPR competitive binding assay

Antibodies were assessed using the Biacore 8K system (GE Healthcare). For competitive binding experiments, His-tagged MO1 or RU15-1 RBD proteins were immobilized on Anti-His sensor chips (Cytiva) at a concentration of 1.35 μg/mL for 1 minute. Pairs of antibodies (37.5 μg/mL each) were then sequentially injected over the chip surface, with each injection lasting 2 minutes. The chip surface was regenerated with 1.5 M glycine. Competition between antibodies was quantified using the following score: score $_{b-a}$=1−response$_b$/ response$'_b$where

response$_b$ represents the response units (RU) when antibody *b* was injected as the second antibody following antibody *a*, and *response*$'_b$ represents the mean RU when antibody *b* was injected as the first antibody.

Antigen-hFc live-cell binding assay

Live-cell binding assays for coronavirus RBD-hFc fusion proteins were performed as previously described. HEK293T cells transiently expressing distinct receptors or orthologous APNs were incubated 48 hours post-transfection with recombinant RBD-hFc proteins (2 μg/mL diluted in DMEM) for 30 minutes at 37°C (5% CO_2). Cells were gently washed once with Hanks' Balanced Salt Solution (HBSS), then stained for 1 hour at 37°C with Alexa Fluor 488-conjugated goat anti-human IgG (1 μg/mL; Thermo Fisher Scientific, #A11013) and Hoechst 33342 nuclear counterstain (1:10,000 dilution in HBSS). Both reagents were prepared in HBSS containing 1% bovine serum albumin (BSA). After staining, cells were washed twice with HBSS and imaged with fresh HBSS. Fluorescence microscopy used an MI52-N system (Nikon). Relative fluorescence intensities (RFU) were quantified using a Varioskan LUX multimode plate reader (Thermo Scientific).

For experiments with RBD-specific antibody competition, recombinant RBD-hFc proteins (2 μg/mL) and indicated RBD-specific antibodies (10 μg/mL) were mixed within 50 μL DMEM for 1 hour at 37°C and then applied to HEK293T cells transiently expressing *E.amu* APN for RBD-hFc binding efficiency evaluation.

Flow cytometry

To analyze RBD-hFc binding by flow cytometry, HEK293T cells transiently expressing the indicated APN orthologs were detached with 5 mM EDTA/PBS 24 hours post-transfection. For antibody–APN competition assays, the detached cells were pretreated with indicated antibodies (10 μg/mL) in 37 ℃ for 1 hour. Cells were incubated with RU15-1 or MO1 RBD-hFc proteins (2 μg/mL) at 4 °C for 1 hour. After two PBS washes, cells were stained for 1 hour at 4 °C using Alexa Fluor 488- or DyLight 594-conjugated goat anti-human IgG antibodies to detect RBD binding (Thermo Fisher Scientific; A11013). Following two additional PBS washes, 20,000 live cells (gated based on SSC/FSC) were analyzed on a CytoFLEX flow cytometer (Beckman).

Western blot

Western blotting was performed to assess S glycoprotein incorporation into VSV pseudoviruses. Pseudovirus-containing supernatants were concentrated through a 30% sucrose cushion (30% sucrose, 15 mM Tris-HCl, 100 mM NaCl, 0.5 mM EDTA) by centrifugation at 20,000 × g for 1 hour at 4°C. Pellets were resuspended in 1 × SDS loading buffer, boiled at 95°C for 30 minutes, and subjected to SDS-PAGE and immunoblotting.

To evaluate expression of different APN orthologs, HEK293T cells were transfected for 24 hours, lysed in 1% Triton X-100 at 4°C for 10 minutes, and clarified by centrifugation at 12,000 × g for 5 minutes. Supernatants were mixed with 5 × loading buffer and analyzed by Western blot. Membranes were blocked with 5% milk in PBST for 1 hour at room temperature, incubated overnight at 4°C with anti-HA or anti-APN polyclonal antibodies (Abclonal), and then probed with goat anti-mouse IgG secondary antibody for 1 hour at room temperature. After four washes in PBST, signals were visualized using the Omni-ECL Femto Light Chemiluminescence Kit (EpiZyme, SQ201) and imaged on a ChemiDoc MP system (Bio-Rad).

Immunofluorescence assay

Immunofluorescence assays were performed to assess the expression levels of APN orthologs with C-terminal fused 3×FLAG tags. Cells expressing the receptors were seeded in the 96-well plates. Specifically, the transfected cells were fixed and permeabilized with 100% methanol for 10 minutes at room temperature. Then the cells were incubated with a mouse antibody M2 (Sigma-Aldrich, F1804) diluted in HBSS/1% BSA for 1 hour at 37 °C. After one HBSS wash, the cells were incubated with Alexa Fluor 594-conjugated goat anti-mouse IgG (Thermo Fisher Scientific, A32742) secondary antibody diluted in 1% BSA/PBS for one hour at 37 °C. The images were captured with a fluorescence microscope (Mshot, MI52-N) after the nucleus was stained blue with Hoechst 33342 reagent (1:2,000 dilution in HBSS).

Pull-down assay

For pull-down assays, recombinant viral RBD-hFc-Strep-FLAG and soluble *E.amu* APN-His proteins were expressed in eukaryotic cells and purified by affinity chromatography. Viral RBD-hFc-Strep-FLAG protein (1 μg/mL) was incubated with 30 μL suspended Mag-Strep beads in 500 μL PBS at 4 °C for 1 hour. Beads were washed three times with cold PBS and then incubated with 2 μg of *E.amu* APN-His protein in 1 mL PBS at 4 °C for an additional hour. After washing three times with cold PBS, beads were resuspended in PBS, denatured in 1 × SDS-loading buffer, and boiled for 20 minutes. Samples were analyzed by SDS-PAGE followed by western blotting.

Biolayer interferometry (BLI) binding assay

Binding affinities were measured using bio-layer interferometry (BLI) on an Octet RED96 instrument (Molecular Devices), following a protocol similar to that described above[95,96]. Briefly, recombinant MO1 and RU15-1 RBD-His proteins (50 μg/mL) were immobilized onto Ni-NTA biosensors (ForteBio) for 300 s. Following loading, the biosensors were transferred to kinetics buffer (PBS supplemented with 0.02% Tween-20; PBST) for 60 s to remove unbound proteins. The sensors were then immersed in PBST containing serial dilutions (0–10 μM) of soluble *E. amurensis* APN ectodomain (twin-Strep-tag) for 120 s to monitor the association phase, followed by a 120 s dissociation phase in PBST. Data acquisition and analysis were performed using Octet Acquisition 9.0 and Octet Analysis 12.2.0.20 software (ForteBio), respectively.

Cell-cell fusion assays

A cell-cell fusion assay based on dual-split proteins (DSPs) was performed in HEK293T cells stably expressing *E.amu* APN, which were transiently transfected with Spike and reporter gene expressing vectors by Lipofectamine 2000 following the manufacture's instructions. Two groups of cells were prepared to assess the S glycoprotein-mediated membrane fusion promoted by receptor interaction. Group A cells were transfected with plasmids expressing S glycoprotein and rLucN(1-155)-sfGFP1-7(1-157), while group B cells received plasmids encoding the S glycoprotein and sfGFP8–11(158–231)-rLuc(156–311). At 12 hours post-transfection, both groups of cells were trypsinized, mixed, and seeded into a 96-well plate at 8×10^4 cells per well. At 24 h post-transfection, the cells were washed twice with DMEM and then incubated with DMEM containing the indicated concentrations of Trypsin, from porcine pancreas (Sigma-Aldrich, T4549) for 30 minutes at 37 °C. Trypsin activity was then quenched by replacing the medium with DMEM supplemented with 10% FBS and Hoechst 33342 (1:5,000) for nuclear staining. Syncytia formation with green fluorescence was assessed after 1.5 hours post-trypsin treatment, and images were captured by an ELISPOT reader (S6 UNIVERSAL M2).

Pseudovirus production

Pseudoviruses carrying coronavirus S glycoproteins were generated using a vesicular stomatitis virus (VSV)-based pseudotyping system based on a previously published protocol with minor modifications[5]. Briefly, HEK293T cells were transfected with plasmids encoding the S proteins using Lipofectamine 2000 (Biosharp, China). After 24 hours, the cells were infected with VSV-ΔG-fLuc-GFP (1×10^6 TCID50/mL) in DMEM supplemented with 8 μg/mL polybrene and incubated for 2 hours at 37 °C on a shaker. The inoculum was then replaced with fresh DMEM or SMM 293-TII Expression Medium (Sino Biological, M293TII) containing an anti-VSV-G monoclonal antibody (I1, 1 μg/mL) to neutralize residual input virus. After another 24 hours, the supernatant containing pseudoviruses was harvested, clarified by centrifugation at 13,523 × g for 5 minutes at 4 °C, and stored at −80 °C until use.

Single-round pseudovirus entry and neutralization assay

Single-round EriCoV pseudovirus entry assays were performed in HEK293T cells transiently or stably expressing various receptors. Cells were seeded in 96-well plates at 3×10^4 cells/well and infected with pseudoviruses (1.5×10^5 $TCID_{50}$ in 100 μL) in the presence of the I1 anti-VSV-G neutralizing antibody to minimize background.

For proteolytic activation, pseudoviruses were pretreated with 1.25 mg/mL trypsin (Sigma-Aldrich, T4549) for 1 hour at 37°C, then trypsin activity was quenched with 10% FBS. For untreated controls, PBS was added instead. At 16–20 hours post-infection (hpi), intracellular luciferase activity was measured using the Bright-Glo Luciferase Assay System (Promega, E2620) on a Thermo Varioskan LUX, or GloMax 20/20 Luminometer (Promega).

Monoclonal antibodies or plasma samples were serially diluted in DMEM (Hyclone, cat. no. SH30243.01) and incubated with pseudovirus in 96-well plates at 37°C under 5% CO_2 for 1 hour. Trypsin-digested HEK293T-*E.amu* APN cells were then seeded into the plates and cultured for 24 hours. After discarding half of the supernatant, reconstituted lyophilized Bright-Lite Luciferase Assay Substrate was mixed with Bright-Lite Luciferase Assay Buffer (Vazyme, cat. no. DD1209-03-AB) before being added to the wells for incubation in the dark. Luminescence intensity was measured using a microplate spectrophotometer (PerkinElmer, model HH3400). The 50% inhibitory concentration (IC_{50}) and the 50% neutralization titer (NT_{50}) were calculated via four-parameter logistic regression using PRISM software (version 9.0.1).

rcVSV-CoV amplification and neutralization assay

Experiments involving replication-competent VSV-S (rcVSV-S) were approved by the Biosafety Committee of the State Key Laboratory of Virology and Biosafety of Wuhan University and performed under Biosafety Level 2 (BSL-2) conditions. Plasmids for rescuing rcVSV-S expressing IT5-12, RU15-1 or MO1 spike (S) glycoproteins were constructed by substituting the firefly luciferase (fLuc) coding sequence with coronavirus S gene sequences in the pVSV-ΔG-fLuc-GFP vector backbone[69,88]. In these recombinant viruses, the VSV-G gene was replaced with genomically encoded S glycoproteins, with a GFP reporter expression cassette for visualization. rcVSVs expressing IT5-12, RU15-1 or MO1 S glycoproteins were generated via reverse genetics following a modified published protocol. Briefly, BHK21 cells seeded at 80% confluence in 6-well plates were infected with recombinant vaccinia virus expressing T7 RNA polymerase (vvT7 provided by Mingzhou Chen's laboratory, Hubei University) at a multiplicity of infection (MOI) of 5 for 45 minutes at 37°C. Following infection, cells were transfected with pVSV-ΔG-GFP-S plasmids and helper plasmids (mass ratio: 5:3:5:8:1 for pVSV-ΔG-GFP-S:pBS-N:pBS-P:pBS-G:pBS-L). Supernatants containing rcVSV-

S (designated P0) were harvested 48 hours post-transfection, filtered (0.22 μm) to eliminate residual vvT7, and used to infect Caco-2 cells pre-transfected with VSV-G for production of passage 1 (P1) viruses. To generate passage 2 (P2) viral particles carrying IT5-12, RU15-1, or MO1 S glycoproteins, P1 viruses were used to infect Caco-2 cells stably expressing *E.amu* APN without ectopic VSV-G expression and in the presence of anti-VSV-G (I1-hybridoma supernatant).

For viral amplification assays, 3×10^4 trypsinized Caco-2 cells expressing relevant APNs were seeded in 96-well plates and incubated with rcVSV-CoV (1×10^4 $TCID_{50}$/100 μL) in DMEM supplemented with 2% FBS, with or without TPCK-treated trypsin. Nuclei were stained with Hoechst 33342 (1:10,000 dilution in HBSS) for 30 minutes at 37°C. Fluorescence images were acquired at designated time points post-infection using an MI52-N fluorescence microscope (Nikon).

For antibody neutralization assays, Caco-2-*E.amu* APN-*E.amu* TMPRSS2 cells were seeded in 96-well plates at a density of 5×10^4 cells per well. Twelve hours later, rcVSV-CoV was incubated with the indicated concentrations of antibodies in DMEM for 1 hour at 37 °C, then added to the target cells in DMEM containing 2% FBS. At the indicated time post-infection, nuclei were stained with Hoechst 33342 (1:10,000 dilution in HBSS) for 30 minutes at 37 °C, and fluorescence images were acquired using a fluorescence microscope (MI52-N).

Cryo-EM sample preparation and data collection

Cryo-EM samples were prepared by mixing the respective protein components at defined molar ratios. For the *E.amu* APN–RU15-1 RBD complex, proteins were combined at a 1:3 molar ratio. For the RU15-1 RBD+BD23-0177 Fab+BD23-0152 Fab and MO1 RBD+BD23-0027 Fab+BD23-0087 Fab complexes, the components were mixed at 1:1.2:1.2 molar ratios, respectively. The RU15-1 Spike sample was adjusted to a final concentration of 1 mg/mL. All mixtures were incubated at 4 °C overnight prior to grid preparation, following the same procedure as used for previous cryo-EM sample preparations[97]. Each complex was subjected to size-exclusion chromatography (SEC) to ensure sample homogeneity. The subsequent mixture of RBD and *E.amu* APN requires the addition of amastatin to a final concentration of 1 mM. The samples were applied to glow-discharged holey carbon-coated gold grids (C-flat, 300 mesh, 1.2/1.3, Protochips Inc.), blotted for 7 seconds without blotting force under 100% relative humidity, and plunge-frozen in liquid ethane using a Vitrobot (FEI).

Cryo-EM data were collected on an FEI Titan Krios transmission electron microscope operated at 300 kV. Movies were recorded using a K3 Summit direct electron detector in counting mode, with each movie consisting of 32 frames (0.2 s per frame) and a total electron dose of 60 $e^-/Å^2$. Automated data acquisition was performed using SerialEM. For the *E.amu* APN–RU15-1 RBD, the RU15-1 RBD+BD23-0177 Fab+BD23-0152 Fab and MO1 RBD+BD23-0027 Fab+BD23-0087 Fab complexes, data were acquired at a nominal magnification of 165,000 ×, corresponding to a calibrated pixel size of 0.82 Å. For RU15-1 Spike, data were acquired at a nominal magnification of 29,000 ×, corresponding to a calibrated pixel size of 1.07Å. The defocus range was set between −1.2 and −2.0 μm.

Cryo-EM data processing, model fitting, and refinement

A total of 2,125, 3,559, 4,260, and 4,002 micrographs were collected for the RU15-1 Spike, *E.amu* APN–RU15-1 RBD, RU15-1 RBD–BD23-0177–BD23-0152, and MO1 RBD–BD23-0027–BD23-0087 complexes, respectively. Beam-induced motion correction was performed

using MotionCor2, and the defocus values of each micrograph were estimated with Gctf[98]. A total of 1,073,532, 1,178,055, 1,516,562, and 1,134,767 particles were extracted from the corresponding datasets. Based on the 2D class averages, 215,898, 170,003, 179,494, and 129,849 particles were selected for final reconstruction in cryoSPARC[99].

During ab initio reconstruction, no symmetry was imposed, which resulted in multiple initial models representing potential conformational states of the complexes. For homogeneous refinement, symmetries of C3, C2, C1, and C1 were applied to the RU15-1 Spike, *E.amu* APN–RU15-1 RBD, RU15-1 RBD–BD23-0177–BD23-0152, and MO1 RBD–BD23-0027–BD23-0087 datasets, respectively. The best models were subsequently subjected to non-uniform refinement in cryoSPARC to generate the final cryo-EM density maps. For the *E.amu* APN–RU15-1 RBD complex, to further improve the local resolution at the interaction interface between *E.amu* APN and RU15-1 RBD, symmetry expansion followed by local refinement (C1) was performed, yielding a high-resolution structure of the *E.amu* APN monomer in complex with RU15-1 RBD.

The final resolution of each structure was estimated using the gold-standard Fourier shell correlation (FSC) criterion (threshold=0.143), and local resolution was evaluated using ResMap[100]. A detailed summary of the image processing workflow is provided in Supplementary Information, Extended Data Fig. 6a and 10a,b, and the statistics are listed in Extended Data Table 1.

The atomic model of all complexes were generated by fitting structures (predicted by AlphaFold3) into the cryo-EM densities described above by Chimera[101], followed by manual adjustment and correction according to the protein sequences and densities in Coot[102], as well as real space refinement using Phenix[103]. Details of the refinement statistics of the complexes are summarized in Extended Data Table 1.

Bioinformatic and structural analysis

A dataset of 25 unique EriCoV S glycoproteins was gathered via BLAST searches of the NCBI database using the HKU31-F6 S protein as a reference sequence. After eliminating redundant sequences with 100% RBD amino acid identity and those containing ambiguous base calls, 22 unique RBD sequences were collected for further analysis. The RBD and S protein sequences used for phylogenetic analysis in Fig. 1c and Extended Data Fig. 1b were aligned via MAFFT-DASH, while the RBM sequence alignments in Fig. 1f were aligned via MAFFT (v7.45071) with manual adjustments to optimize indel positioning. Phylogenetic trees were constructed using IQ-TREE (version 2.0.6) under the Maximum Likelihood model with 1,000 bootstrap replicates. Evolutionary model selection was performed using ModelFinder Plus in IQ-TREE with Bayesian Information Criterion (BIC) optimization. The best-fit models implemented were: WAG+G4 model for RBDs, GTR+F+I+I+R4 model for the whole genomes, WAG+F+I+R3 model for spike proteins, and Q.plant+F+I+I+R6 model for the APN protein sequences. Pairwise sequence identities were calculated in Geneious Prime (version 2023.0.4) (https://www.geneious.com/) following MAFFT-DASH alignment. Experimentally resolved structures used for structural analysis in this study included: MERS-CoV RBD (4KQZ), HKU4-1 RBD (4QZV), HKU5-19s RBD (9D32), NeoCoV RBD (PDB: 7WPO), EriCoV-GER216 RBD (9JMG), MOW15-22 RBD (9C6O), HCoV-229E RBD-hAPN complex (6U7E), PDCoV RBD-pAPN complex (7VPQ), and PRCV RBD-pAPN complex (4F5C). Structural visualization and analysis were performed using ChimeraX (v1.7.1). A total of 94 orthologous APN protein sequences from mammals and *Gallus gallus* were collected from NCBI (either directly annotated or extracted from whole-genome assemblies) and UniProt. Multiple sequence alignment was performed using MAFFT (v7.45071)[104], and phylogenetic trees were

constructed with IQ-TREE using the Maximum Likelihood method with 1,000 bootstrap replicates[105]. The resulting trees were visualized using iTOL (https://itol.embl.de/).

Predicting the Effects of Human APN Mutations on Binding Affinity to RU15-1

To evaluate the impact of hAPN mutations on its interaction with the RU15-1 RBD, we computationally predicted the changes in binding free energy (ΔΔG) induced by multiple amino-acid substitutions. Structure-based binding affinity predictions were performed using PPI2, a machine learning–based approach for assessing the energetic effects of point mutations on protein–protein interactions. The structure of the hAPN–RU15-1 complex was used as the template for all calculations after removal of solvent molecules and glycosylation site.

For each designed mutation, PPI2 was applied to estimate the binding free energy change (ΔΔG), calculated as:

$$\Delta\Delta G = \Delta G_{wt} - \Delta G_{mut}$$

where ΔG_wt and ΔG_mut represent the predicted binding free energy values of the wild-type and mutant complexes, respectively. Positive ΔΔG values indicate a predicted enhancement of binding affinity, whereas negative values correspond to reduced affinity relative to the wild-type.

Quantification and statistical analysis

Most experiments related to pseudovirus infection were conducted 2-3 times with 2-3 biological repeats; technical repeats are indicated in the legends. Representative results were shown. All data were presented by MEAN or MEAN ± SD. Unpaired two-tailed t-tests were conducted for all statistical analyses for two independent groups using GraphPad Prism 10. $P<0.05$ was considered significant. *: $P<0.05$, **: $P<0.01$, ***: $P<0.005$, and ****: $P<0.001$, NS: not significant. No data were excluded for data analysis.

Reference

91. Götzke, H. *et al.* The ALFA-tag is a highly versatile tool for nanobody-based bioscience applications. *Nat Commun* **10**, 4403 (2019).
92. Schwegmann-Weßels, C. *et al.* Comparison of vesicular stomatitis virus pseudotyped with the S proteins from a porcine and a human coronavirus. *J Gen Virol* **90**, 1724–1729 (2009).
93. Zhu, Q., Liu, P., Liu, S., Yue, C. & Wang, X. Enhancing RBD exposure and S1 shedding by an extremely conserved SARS-CoV-2 NTD epitope. *Signal Transduction and Targeted Therapy* **9**, 1–3 (2024).
94. Yue, C. *et al.* Deletion of V483 in the spike confers evolutionary advantage on SARS-CoV-2 for human adaptation and host-range expansion after a prolonged pandemic. *Cell Research* **34**, 739–742 (2024).
95. Wang, K. *et al.* Memory B cell repertoire from triple vaccinees against diverse SARS-CoV-2 variants. *Nature* **603**, 919–925 (2022).
96. Cao, Y. *et al.* Characterization of the enhanced infectivity and antibody evasion of Omicron BA.2.75. *Cell Host Microbe* **30**, 1527–1539.e5 (2022).
97. Liu, P. *et al.* Spike N354 glycosylation augments SARS-CoV-2 fitness for human adaptation through structural plasticity. *Natl Sci Rev* **11**, nwae206 (2024).
98. Gctf: Real-time CTF determination and correction. *Journal of Structural Biology* **193**, 1–12 (2016).
99. Punjani, A., Rubinstein, J. L., Fleet, D. J. & Brubaker, M. A. cryoSPARC: algorithms for rapid unsupervised cryo-EM structure determination. *Nature Methods* **14**, 290–296

(2017).
100. Kucukelbir, A., Sigworth, F. J. & Tagare, H. D. Quantifying the local resolution of cryo-EM density maps. *Nature Methods* **11**, 63–65 (2013).
101. Pettersen, E. F. *et al.* UCSF Chimera—A visualization system for exploratory research and analysis. *Journal of Computational Chemistry* **25**, 1605–1612 (2004).
102. Emsley, P. & Cowtan, K. Coot: model-building tools for molecular graphics. *Acta Crystallogr D Biol Crystallogr* **60**, 2126–2132 (2004).
103. Adams, P. D. *et al.* PHENIX: a comprehensive Python-based system for macromolecular structure solution. *Acta Crystallogr D Biol Crystallogr* **66**, 213–221 (2010).
104. Nakamura, T., Yamada, K. D., Tomii, K. & Katoh, K. Parallelization of MAFFT for large-scale multiple sequence alignments. *Bioinformatics* **34**, 2490–2492 (2018).
105. Nguyen, L.-T., Schmidt, H. A., von Haeseler, A. & Minh, B. Q. IQ-TREE: a fast and effective stochastic algorithm for estimating maximum-likelihood phylogenies. *Mol. Biol. Evol.* **32**, 268–274 (2015).

Acknowledgments

This study was supported by the National Key R&D Program of China (2024YFC2607300 and 2023YFC2605500 to H.Y.), the National Natural Science Foundation of China (NSFC) projects (82322041, 32270164 to H.Y., 323B2006 to C.-B.M.), Scientific Research Innovation Capability Support Project for Young Faculty (ZYGXONJSKYCXNLZCXM-H16 to H.Y.), Natural Science Foundation of Hubei Province (2023AFA015 to H.Y.), the Fundamental Research Funds for the Central Universities (to H.Y.), and TaiKang Center for Life and Medical Sciences (to H.Y.). This work was also supported by the Strategic Priority Research Program (XDB1310000 to X.W.), National Science Foundation Grants (32325004, T2394482, and 12034006 to X.W.), Basic Research Program Based on Major Scientific Infrastructures, CAS-JZHKYPT-2021-05, CAS (YSBR-010 to X.W.), Ministry of Science and Technology of China (CPL-1233 to X.W.), the New Cornerstone Science Foundation (to X.W.), and Changping Laboratory (2025D-04-01 to Y.C.), National Key R&D Program of China (2023YFF0724800 to L.B.). We thank Lu Lu (Fudan University) for providing the EK1C4 peptides used in this study.

Author contributions

H.Y., X.W., Y.C., L.B., and P.L. conceived the project. P.L., C.M., Z.M., Q.Z., J.L., Y.L., and T.L. cloned S, RBD-hFc, and APN mutants and conducted RBD-hFc binding assays. C.M., P.L., J.L., Y.Y., T.L., and X.Yang designed APN ectodomain and antibody constructs and expressed recombinant proteins. C.L., P.L., and J.S. conducted phylogenetic and conservation analysis. Z.M., P.L., and M.H. conducted pseudovirus production and cell-cell fusion assays. Z.M., P.L., and X.Yang rescued the rcVSV-EriCoV-S pseudotypes and performed rcVSV propagation and inhibition assays. Q.Z. and T.L. conducted biolayer interferometry binding experiments. J.L., P.L., and X.Yang carried out VSV pseudovirus entry and neutralization assays. H.M. conducted hedgehog organoid culture-related experiments. Q.Z. carried out cryo-EM sample preparation, data collection, and processing. Q.Z. and X.W. built and refined the structures. J.L., Y.Y., and Q.W. performed animal experiments and flow cytometric sorting of single B cells. Y.Y., J.L., and L.Y. conducted monoclonal antibody expression, functional characterization, and neutralization assays. Q.L., P.L., J.L., Y.Y., and G.M., conducted hedgehog primary cells infection assays. P.L., Z. M., C.L., Y.S., J.S., X.Yu, J.L., and Y.X. analyzed the data. H.Y., X.W., and Y.C. wrote the manuscript with input from all authors.

Data availability

The Cryo-EM maps and models have been deposited to the Electron Microscopy Data Bank and Protein Data Bank (PDB) with accession numbers EMD-67300/PDB ID 9XVR (global refinement of the RU15-1 Spike trimer), EMD-67326/PDB ID 9XW6 (focused reconstruction of the *E.amu* APN in complex with RU15-1 RBD), EMD-67300/PDB ID 9XWA (global refinement of the *E.amu* APN in complex with RU15-1 RBD), EMD-67338/PDB ID 9XWN (global refinement of the RU15-1 RBD+BD23-0177 Fab + BD23-0152 Fab complex), and EMD-67337/PDB ID 9XWM (global refinement of the MO1 RBD+BD23-0027 Fab+BD23-0087 Fab complex).

The 25 EriCoV spike sequences, five receptor sequences from hedgehog (*E.amu* ACE2, *E.amu* DPP4, *E.amu* APN, *E.amu* TMPRSS2, and *A.alb* APN), and 139 APN-coding sequences are provided in the Methods and Supplementary Tables. All other data supporting the findings of this study are available with the Article and the Supplementary Information.

Code availability

This study did not generate custom computer code.

Materials availability

All plasmids generated in this study are available with a completed Materials Transfer Agreement. Correspondence and requests for materials can be addressed to the lead contact, Huan Yan (huanyan@whu.edu.cn).

Competing interests

The authors declare no competing interests.

Supplementary Information is available for this paper.

Supplementary information for

Convergent utilization of APN receptor by hedgehog merbecoviruses

Peng Liu[1,#], Qianhui Zhu[2,3,#], Jingyi Liu[4,5,7,#], Zhixing Ma[1,#], Guocui Mou[8,#], Yuanling Yu[5], Chen Liu[1], Chengbao Ma[1], Junyu Si[1], Xiao Yang[1], Meiling Huang[1], Yanchu Liu[1], Yehui Sun[1], Xiao Yu[1], Yucheng Sun[1], Tianci Liu[2,3], Lingling Yu[5], Qianran Wang[5], Honghao Ma[5], Qi Lv[8], Jing Li[1], Linlin Bao[8,*], Yunlong Cao[4,5,6,*], Xiangxi Wang[2,3,*], Huan Yan[1,*]

The PDF document file includes:

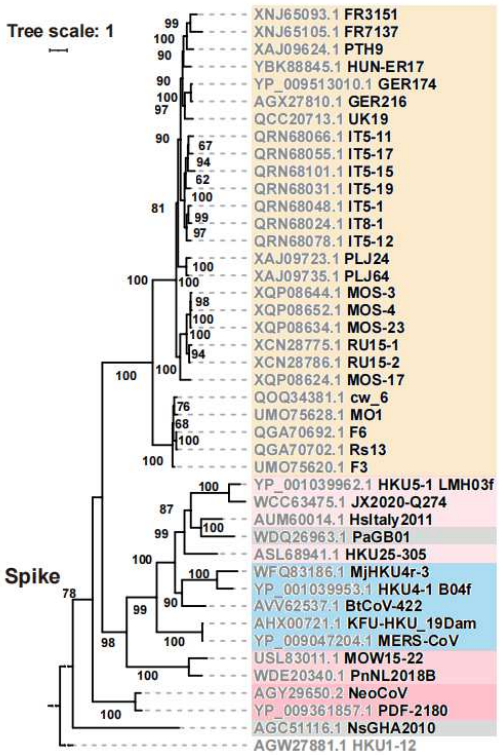
Extended Data Fig. 1 to 12 and Extended Data Table 1

Excel file for Supplementary Table 1
Excel file for Supplementary Table 2
Excel file for Supplementary Table 3
Excel file for Supplementary Table 4
Excel file for Supplementary Table 5

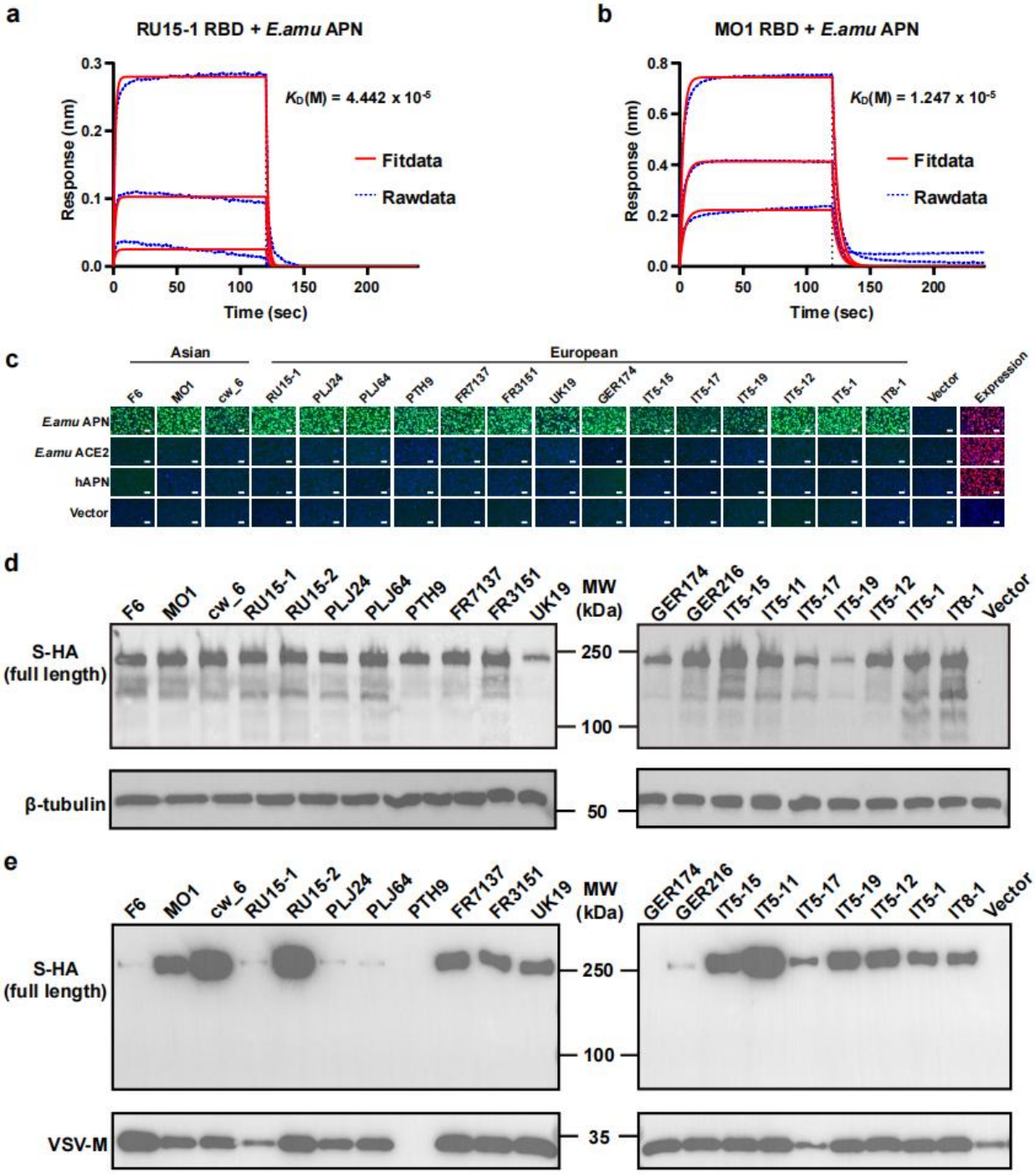
a

Accession numbers	Strains	Abbr.
QOQ34381.1	Erinaceus amurensis coronavirus HKU31 cw_6	cw_6
UMO75628.1	ErinCoV/HKU31/HeB-MO1/2022/China	MO1
UMO75620.1	ErinCoV/HKU31/HeN-F3/2022/China	F3
QGA70692.1	HKU31 F6	F6
QGA70702.1	HKU31 Rs13	Rs13
QRN68066.1	ErinCoV/Italy/50265-11/2019	IT5-11
QRN68101.1	ErinCoV/Italy/50265-15/2019	IT5-15
YP_009513010.1	ErinCoV/2012-174/GER/2012	GER174
AGX27810.1	ErinCoV/2012-216/GER/2012	GER216
XNJ65093.1	ErinCoV/FR/22-3151/2023	FR3151
XNJ65105.1	ErinCoV/FR/22-7137/2022	FR7137
QRN68055.1	ErinCoV/Italy/50265-17/2018	IT5-17
QRN68031.1	ErinCoV/Italy/50265-19/2018	IT5-19
XAJ09723.1	ErinCoV/Poland/J24/2020	PLJ24
XAJ09735.1	ErinCoV/Poland/J64/2021	PLJ64
XCN28775.1	ErinCoV/RU/MOW15-1/2022	RU15-1
XCN28786.1	ErinCoV/RU/MOW15-2/2022	RU15-2
XAJ09624.1	Hedgehog coronavirus 1/Portugal/H9	PTH9
QCC20713.1	Hedgehog coronavirus 1/UK/2019	UK19
QRN68078.1	ErinCoV/Italy/50265-12/2019	IT5-12
QRN68048.1	ErinCoV/Italy/50265-1/2018	IT5-1
QRN68024.1	ErinCoV/Italy/116988-1/2018	IT8-1
XQP08624.1	EriCoV_23_17_MOS-a	MOS-17
XQP08634.1	EriCoV_23_23_MOS-F_2	MOS-23
XQP08644.1	EriCoV_23_3_MOS-a	MOS-3
XQP08652.1	EriCov_23_4_MOS-o	MOS-4
YBK88845.1	EriCoV/ER17/HUN/2023	HUN-ER17

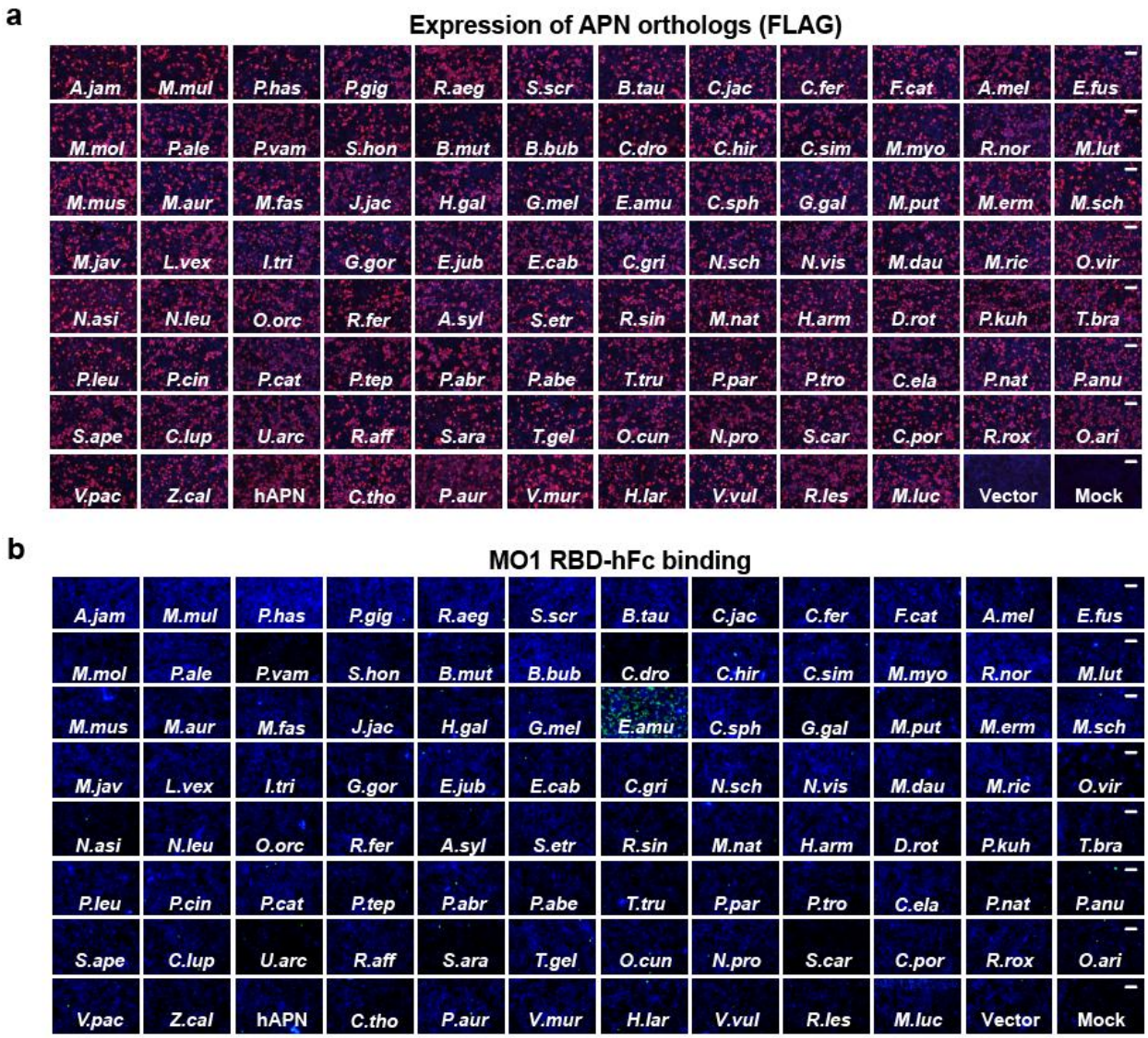
b



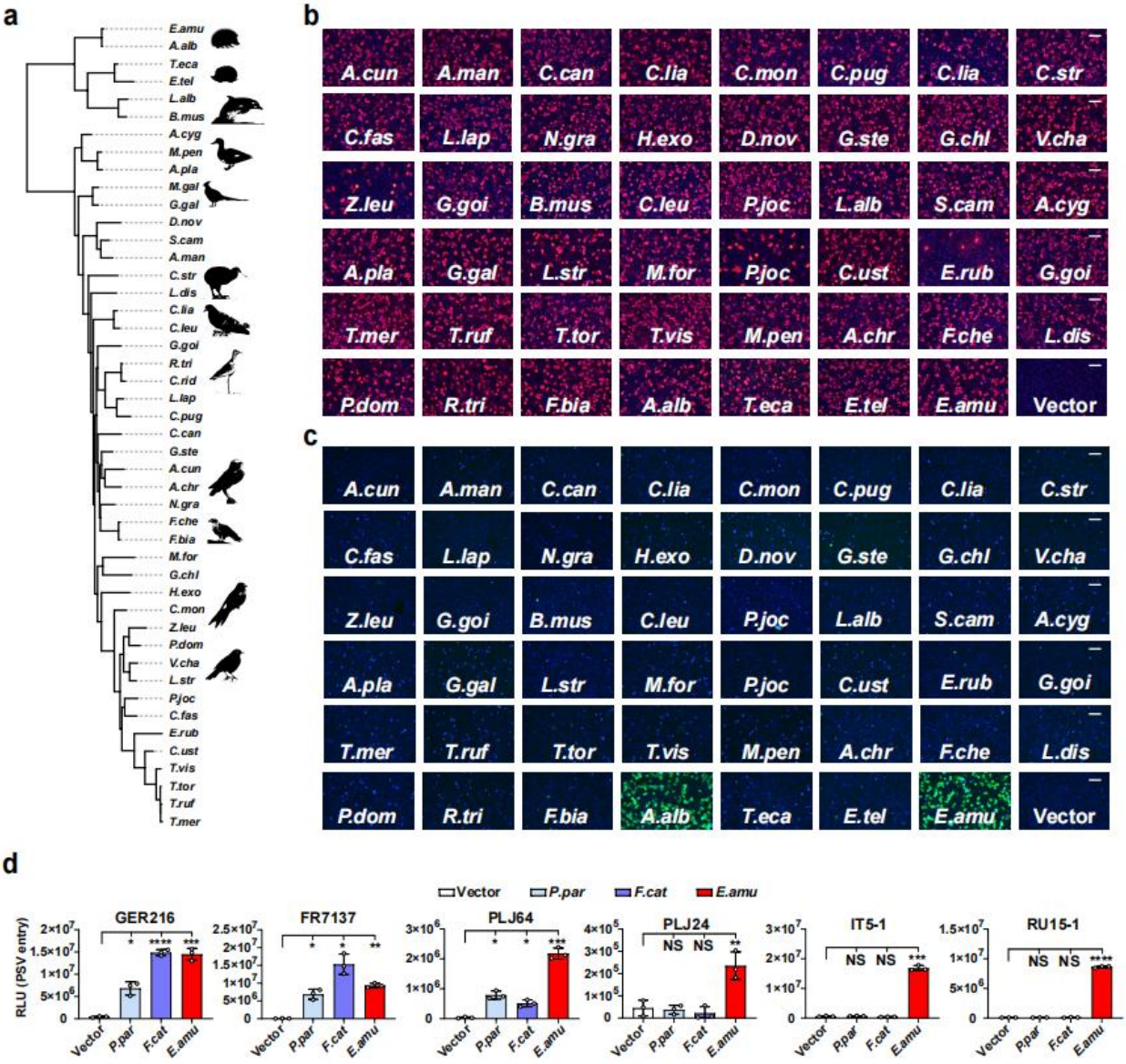
Extended Data Fig. 1 | Abbreviations and phylogenetic analysis of EriCoV S glycoprotein sequences. (**a**) The accession number and abbreviation of the EriCoV strain names involved in this study. (**b**) Phylogenetic trees based on amino acid sequences of S glycoproteins from selected representative merbecoviruses were generated using IQ-TREE. Outgroup: HKU1-12.


a
RU15-1 RBD + E.amu APN
Response (nm)
Time (sec)
KD(M) = 4.442 x 10-5
Fitdata
Rawdata
b
MO1 RBD + E.amu APN
Response (nm)
Time (sec)
KD(M) = 1.247 x 10-5
Fitdata
Rawdata
c
Asian
European
F6
MO1
cw_6
RU15-1
PLJ24
PLJ64
PTH9
FR7137
FR3151
UK19
GER174
IT5-15
IT5-17
IT5-19
IT5-12
IT5-1
IT8-1
Vector
Expression
E.amu APN
E.amu ACE2
hAPN
Vector
d
F6
MO1
cw_6
RU15-1
RU15-2
PLJ24
PLJ64
PTH9
FR7137
FR3151
UK19
MW (kDa)
GER174
GER216
IT5-15
IT5-11
IT5-17
IT5-19
IT5-12
IT5-1
IT8-1
Vector
S-HA (full length)
β-tubulin
250
100
50
e
F6
MO1
cw_6
RU15-1
RU15-2
PLJ24
PLJ64
PTH9
FR7137
FR3151
UK19
MW (kDa)
GER174
GER216
IT5-15
IT5-11
IT5-17
IT5-19
IT5-12
IT5-1
IT8-1
Vector
S-HA (full length)
VSV-M
250
100
35

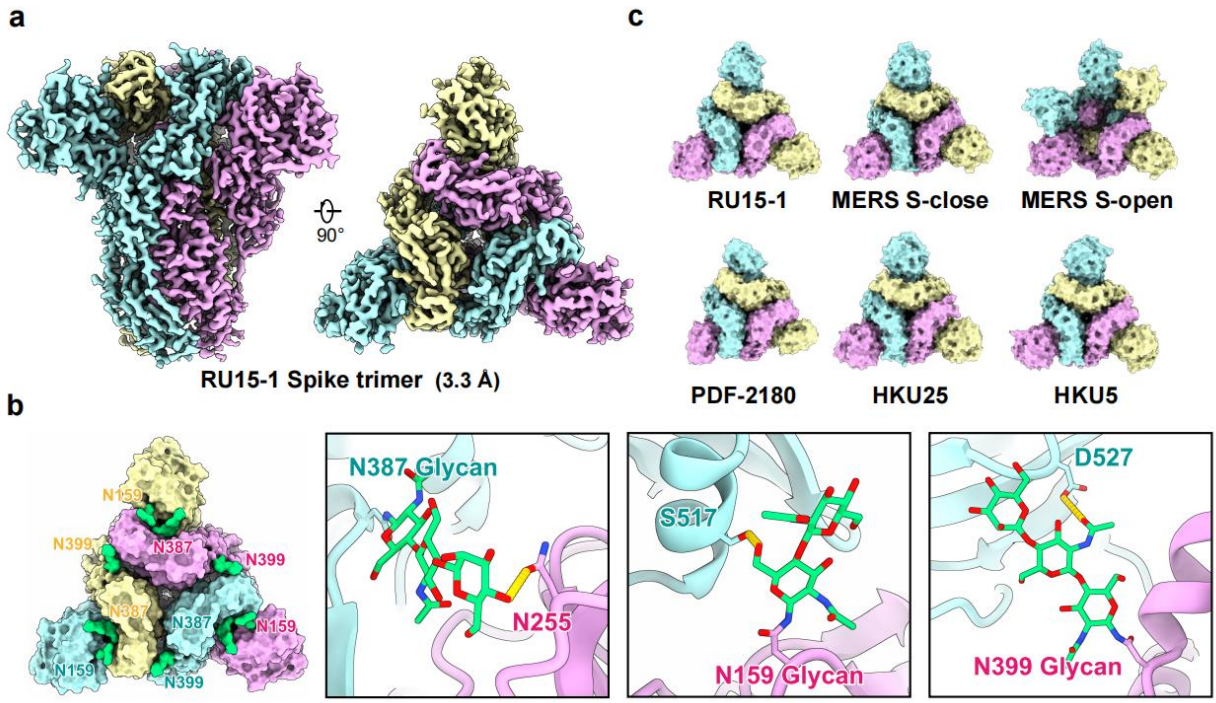
Extended Data Fig. 2 | Binding kinetics of *E.amu* APN–EriCoV RBD-hFc and the expression efficiency of EriCoV spikes. (**a-b**) BLI assays analyzing the binding kinetics of *E.amu* APN ectodomains to immobilized monomeric RU15-1 (a) and MO1 (b) RBD-His proteins on Ni-NTA biosensors. The BLI assay was performed using a 1:1 binding model with fixed-phase and mobile-phase interactions. Data were analyzed by global fitting, and the equilibrium dissociation constant (K_D) was derived from the ratio of the association rate (ka) to the dissociation rate (kd). The fits are shown as red lines. (**c**) RBD-hFc binding of indicated EriCoV strains in HEK293T cells transiently expressing *E.amu* APN, *E.amu* ACE2, hAPN, or vector control. Receptor expression was evaluated by immunofluorescence, detecting the C-terminally fused FLAG tag (red). Scale bars: 100 μm. (**d**) Western blot analysis of indicated EriCoV S protein expression in HEK293T cells. β-tubulin served as a loading control. (**e**) Detection of EriCoV S glycoprotein in VSV pseudovirions via Western blot using an anti-HA antibody targeting the C-terminally fused HA tag. VSV-M serves as a loading control.



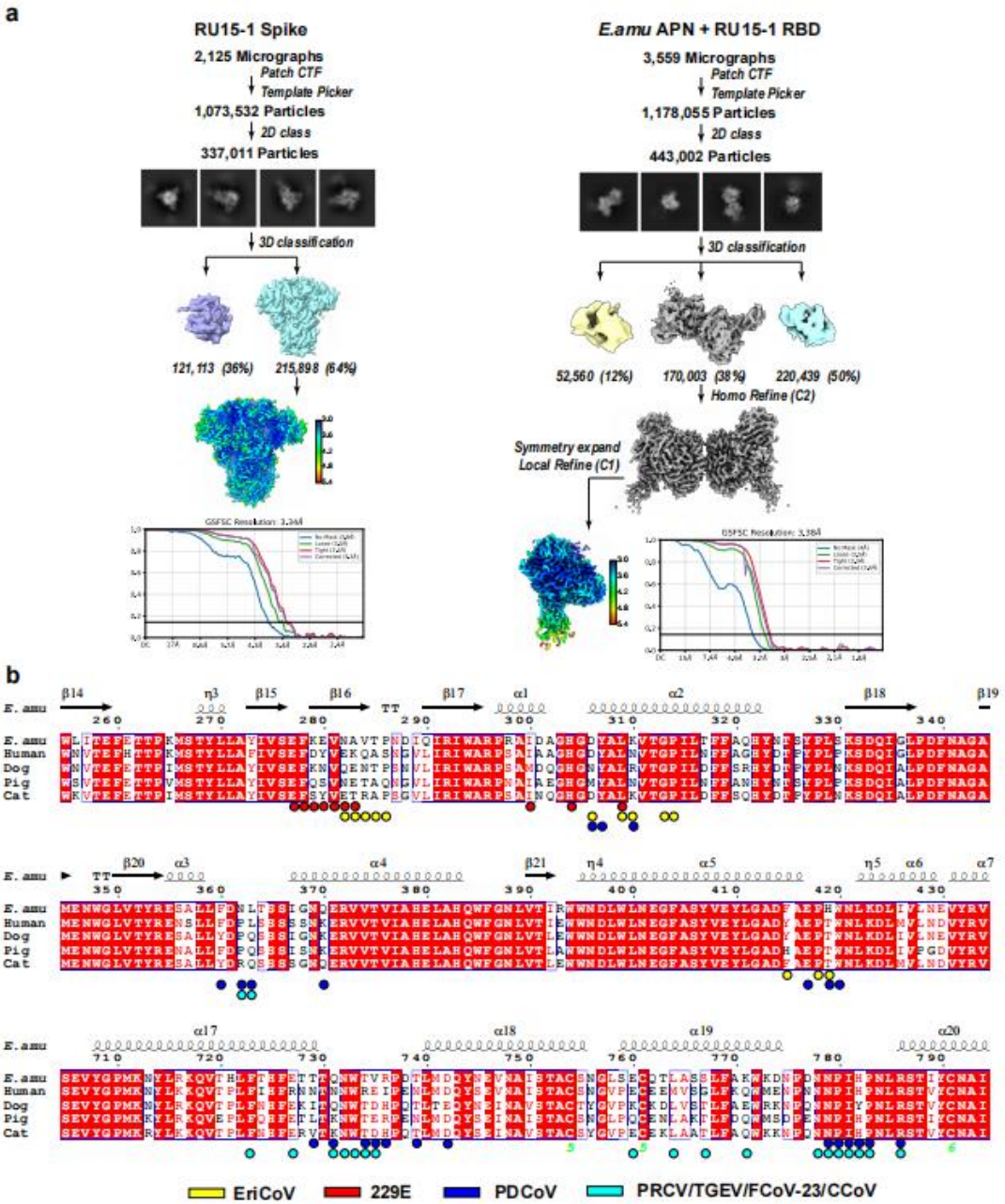
Extended Data Fig. 3 | APN tropism and host range determinant of EriCoV. (**a**) Expression of 94 APN orthologs in HEK293T cells transiently transfected with C-terminally fused 3×FLAG tags was examined through immunofluorescence (red). (**b**) Binding of MO1 RBD-hFc (green) to HEK293T cells transiently expressing the indicated APN orthologs, assessed by immunofluorescence using an anti-hFc antibody (green). Scale bars: 100 μm.



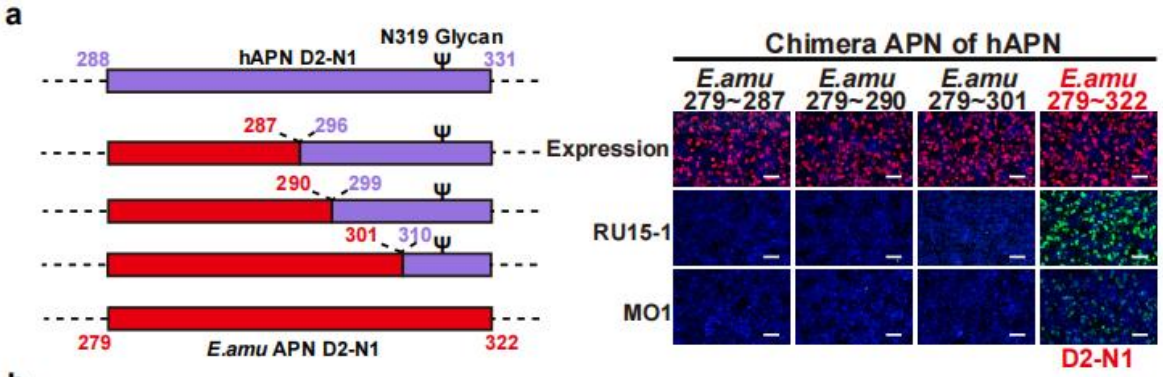
Extended Data Fig. 4 | Avian and mammalian APN tropism of EriCoV. (**a**) Maximal likelihood phylogenetic trees of 46 APN orthologs from mammalian and avian species were constructed using IQ-TREE based on amino acid sequences. (**b**) Expression of selected APN orthologs in HEK293T cells transiently transfected with C-terminally fused 3×FLAG tags was examined through immunofluorescence (red). (**c**) RU15-1 RBD-hFc binding to HEK293T cells transiently expressing indicated receptors. (**d**) Entry of selected EriCoV strains into HEK293T cells transiently expressing indicated APN orthologs. PSVs were pretreated with 1.25 mg/mL trypsin. Data are presented as mean ± SD for d. Statistical significance was determined using unpaired two-tailed *t* tests (n=3 biological replicates). *: P<0.05, **: P<0.01, ***: P<0.005, ****: P<0.001, and NS: not significant. Scale bars: 100 μm.



Extended Data Fig. 5 | Conformations of *E.amu* APN, structural features of the RU15-1 spike. (**a**) Cryo-EM structure of the RU15-1 spike trimer. Cryo-EM reconstruction of the RU15-1 spike trimer at 3.3 Å resolution shown in front (left) and top (right) views. The three protomers are colored cyan, purple, and yellow, respectively. (**b**) Structural representation of glycosylation sites on the RU15-1 Spike. N-linked glycosylation sites are shown in green (left: cartoon representation; right: stick representation). The three protomers are depicted in cyan, purple, and yellow, respectively, and key residues are annotated. (**c**) Cryo-EM reconstructions showing the conformational states of spike trimers from representative merbecoviruses, including RU15-1, MERS-CoV (open and closed), PDF-2180, HKU25, and HKU5. The three protomers are colored cyan, purple, and yellow, respectively.

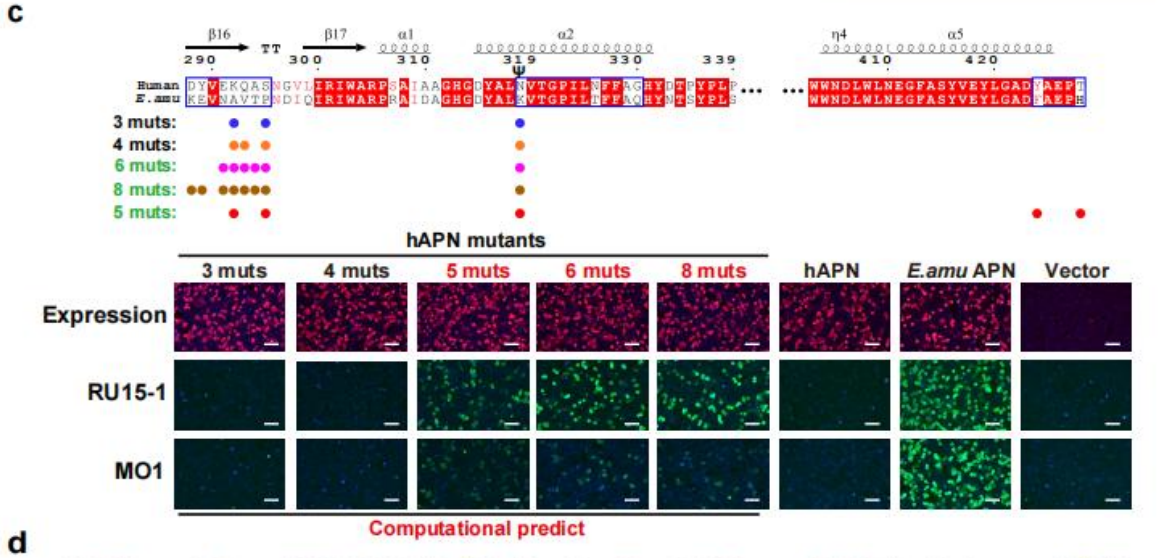

a
RU15-1 Spike
2,125 Micrographs
Patch CTF
Template Picker
1,073,532 Particles
2D class
337,011 Particles
3D classification
121,113 (36%)
215,898 (64%)
E.amu APN + RU15-1 RBD
3,559 Micrographs
Patch CTF
Template Picker
1,178,055 Particles
2D class
443,002 Particles
3D classification
52,560 (12%)
170,003 (38%)
220,439 (50%)
Homo Refine (C2)
Symmetry expand
Local Refine (C1)
b
E.amu
Human
Dog
Pig
Cat
EriCoV
229E
PDCoV
PRCV/TGEV/FCoV-23/CCoV
c
E.amu APN
A283
Y539
RU15-1 RBD
P286
P314
Y528
K310
T532
E.amu APN mutant
K283
S286
N310 glycan

Extended Data Fig. 6 | Cryo-EM data processing workflow and binding site analysis. (**a**) Flowcharts for structure determinations of the RU15-1 Spike and RU15-1 RBD–*E.amu* APN complex. Gold-standard Fourier shell correlation (FSC) curves are shown to assess map quality and resolution. Local resolution assessments of cryo-EM maps using rainbow are shown. (**b**) Multiple sequence alignment of APN orthologs from different species. APN sequences from *Erinaceus amurensis* (Eri), *Homo sapiens* (Homo), *Canis lupus* (Canis), *Sus scrofa* (Sus), and *Felis catus* (Felis) are aligned to highlight sequence conservation and variability. Binding sites located within 4 Å of viral RBDs are indicated by colored circles: yellow for EriCoV, red for HCoV-229E, blue for PDCoV, and cyan for PRCV, TGEV, FCoV-23, and CCoV, which share a common APN-binding mode. (**c**) Structural basis for the effects of key residue mutations in *E.amu* APN on RU15-1 and MO1 binding. The upper panel showed the wild-type *E.amu* APN, and the lower panel displayed the corresponding residue-mutant *E.amu* APN. *E.amu* APN was colored in grey, and the RU15-1 RBD was shown in yellow. All structures were presented as cartoon representations, with key residues highlighted as sticks. The hydrophobic pocket was indicated by a semi-transparent blue surface, hydrogen bonds were depicted as yellow dashed lines, and steric clashes were highlighted by red pentagrams.

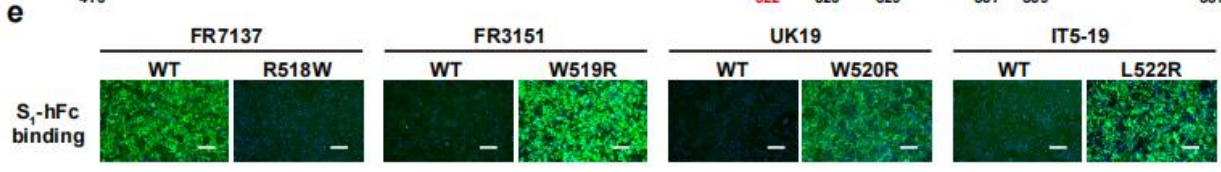


b

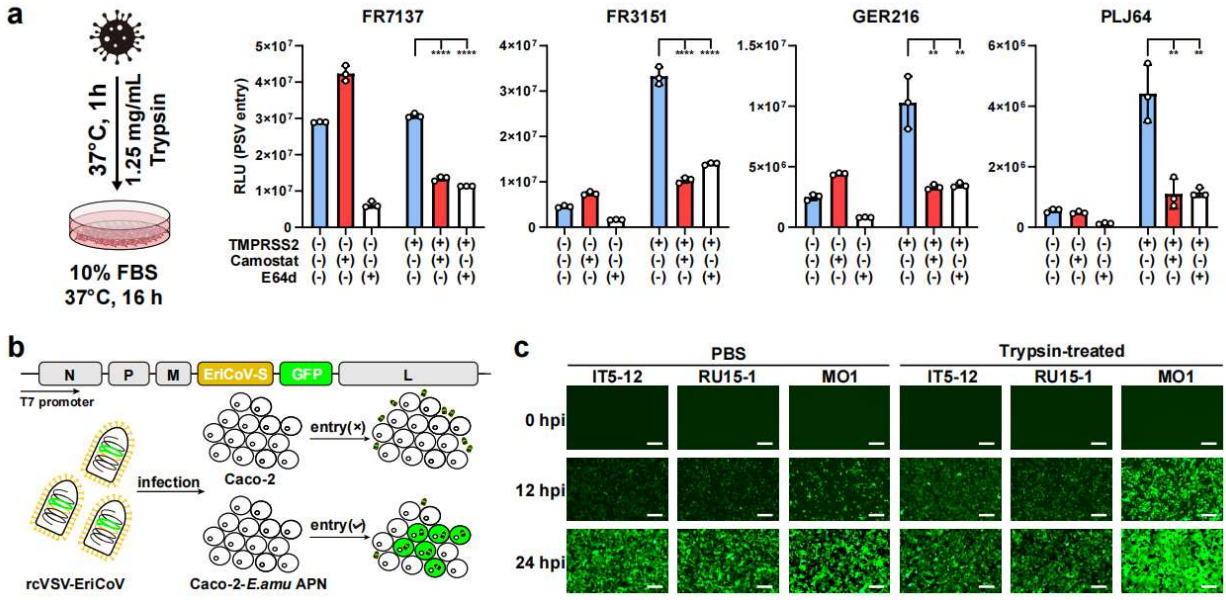
hAPN mutants	ΔΔG (kcal/mol)
3muts: N319K;K292A;S295P	0.235
4muts: N319K;K292A;Q293V;S295P	0.214
5muts: N319K;K292A;S295P;Y424F;T428H	0.331
6muts: N319K;E291N;K292A;Q293V;A294T;S295P	0.365
8muts: N319K;D288K;Y289E;E291N;K292A;Q293V;A294T;S295P	0.389



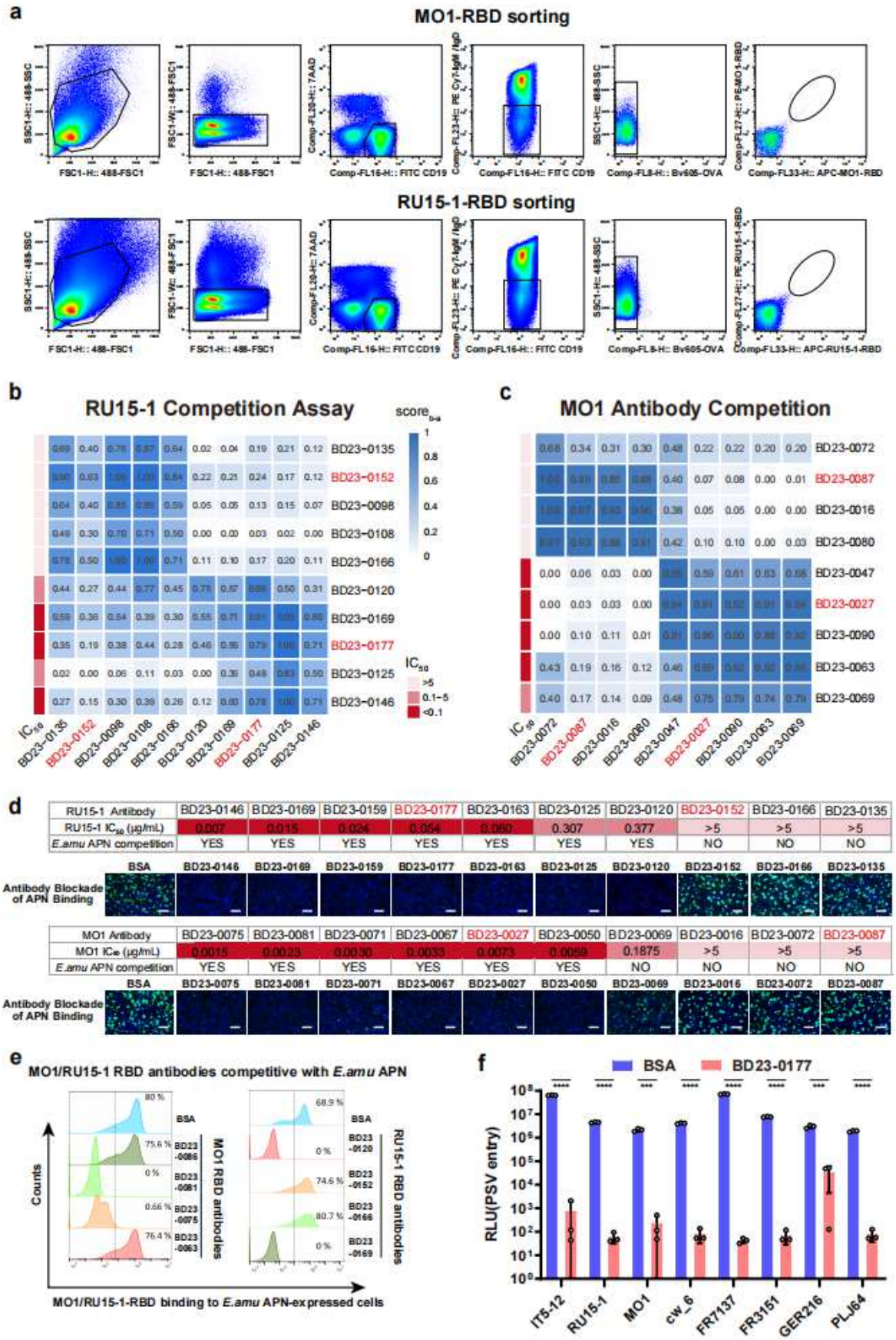




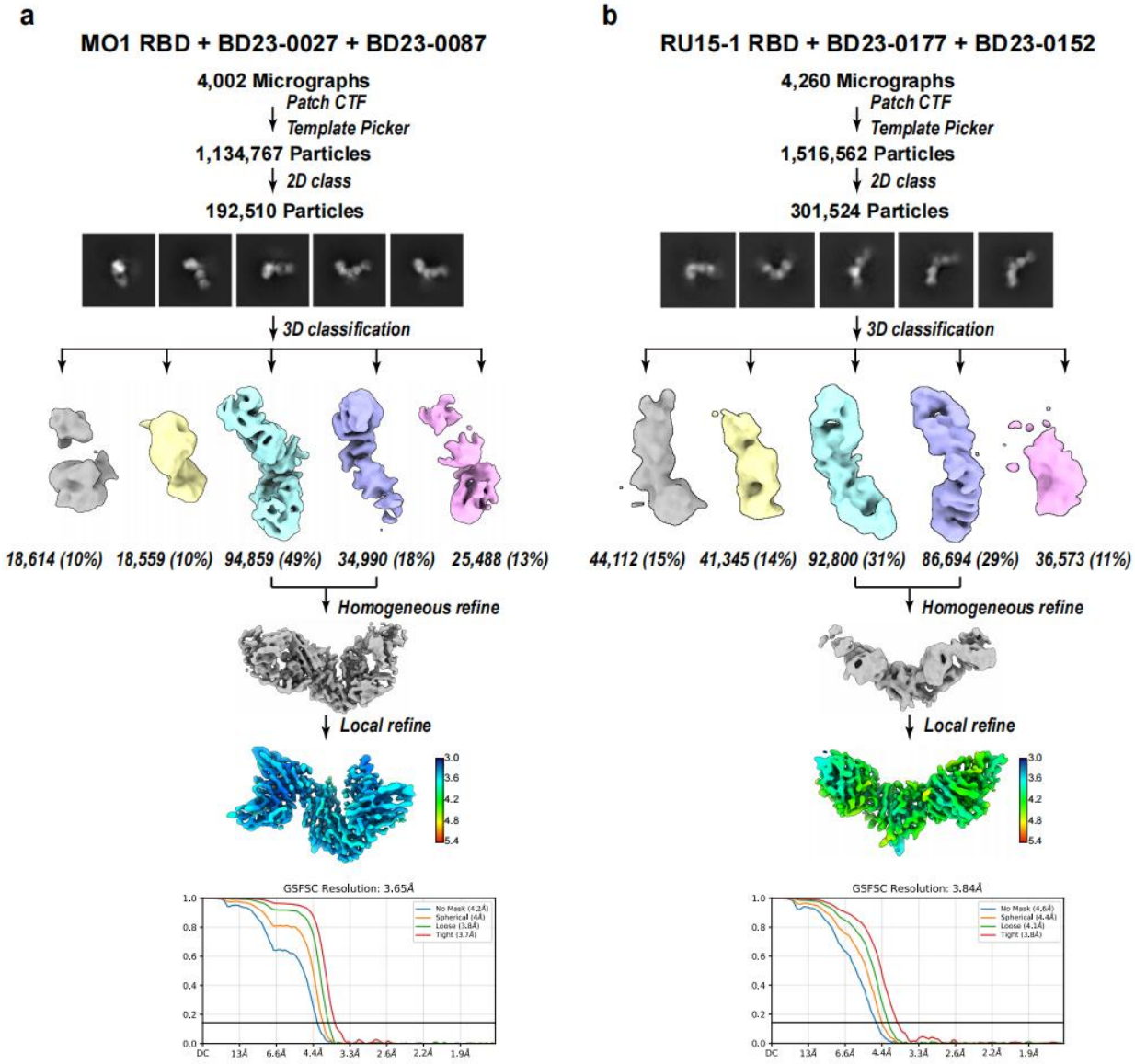
Extended Data Fig. 7 | Prediction and validation of key determinants for EriCoV–APN interaction. (**a**) Substitution of the full D2-N1 region (residues 279-322) from *E.amu* APN is required for hAPN to support RBD-hFc binding of RU15-1 and MO1. N-319 glycosylation in hAPN is labeled with Ψ. Scale bars: 100 μm. (**b**) Predicted effects of multiple mutations in human APN on its binding affinity to RU15-1. Binding affinity changes were estimated by PPI2 with ΔΔG (kcal/mol) calculated as ΔG_wt − ΔG_mut. Positive ΔΔG values indicate enhanced binding affinity of the mutant human APN to RU15-1 relative to the wild-type complex. (**c**) Substitutions of the corresponding residue combinations, based on computational prediction and structural analysis, rendered hAPN capable of supporting RU15-1 or MO1 RBD-hFc binding. Expression of APN and its mutants was confirmed by FLAG-tag immunostaining. (**d**) Sequence logo plot displaying the polymorphisms in receptor binding motifs from 22 EriCoV strains. Critical residues involved in APN interaction were marked with red dots. (**e**) Binding of wild-type and mutant S1-hFc proteins from the indicated European EriCoV strains to HEK293T cells stably expressing *E.amu* APN. Scale bars: 100 μm.



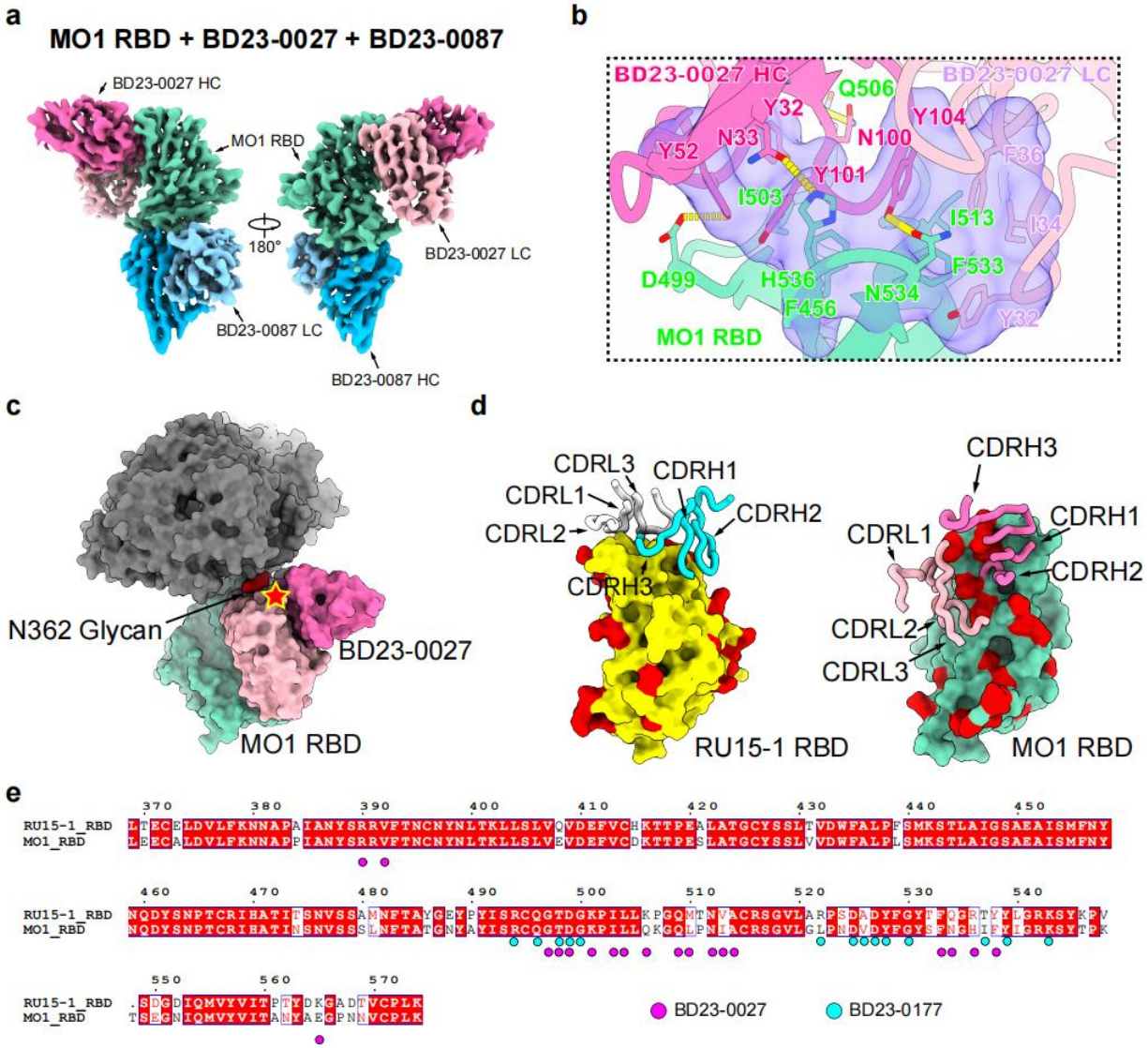
Extended Data Fig. 8 | Inhibition of EriCoV pseudovirus entry by protease inhibitors and rescue/amplification of rcVSV-EriCoV-S. (**a**) Entry of selected EriCoV pseudoviruses into HEK293T cells expressing *E.amu* APN alone or co-expressing *E.amu* APN and *E.amu* TMPRSS2 upon 100 μM Camostat or E64d treatment. (**b**) Schematic illustration of the genetic organization and amplification workflow for rcVSV-S constructs encoding EriCoV S glycoproteins. **(c)** Amplification of rcVSV-RU15-1, rcVSV-IT5-12, and rcVSV-MO1 in Caco-2 cells with the expression of *E.amu* APN. Data are presented as mean ± SD for A. Statistical significance was determined using unpaired two-tailed *t* tests (n=3 biological replicates). *: $P<0.05$, **: $P<0.01$, ***: $P<0.005$, ****: $P<0.001$, and NS: not significant. Scale bars: 200 μm.


a
MO1-RBD sorting
RU15-1-RBD sorting
b
RU15-1 Competition Assay
c
MO1 Antibody Competition
d
RU15-1 Antibody
RU15-1 IC50 (μg/mL)
E.amu APN competition
Antibody Blockade of APN Binding
MO1 Antibody
MO1 IC50 (μg/mL)
e
MO1/RU15-1 RBD antibodies competitive with E.amu APN
Counts
MO1/RU15-1-RBD binding to E.amu APN-expressed cells
f
BSA
BD23-0177
RLU(PSV entry)
IT5-12
RU15-1
MO1
cw_6
FR7137
FR3151
GER216
PLJ64

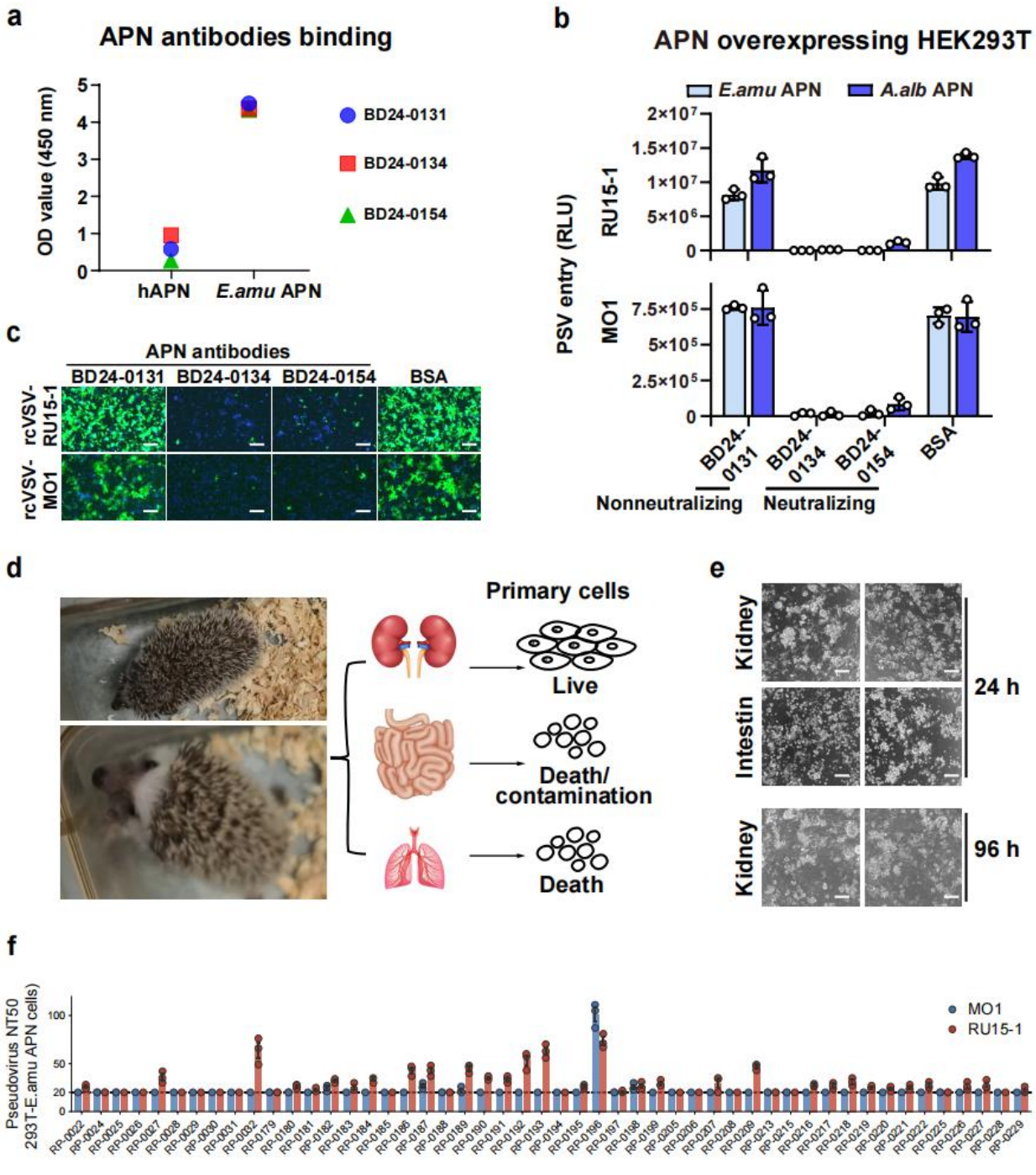
Extended Data Fig. 9 | EriCoV RBD-specific antibodies efficiently inhibited the EriCoV psdovirus entry and the structural analysis of the neutralizing mechanism. (**a**) Flow cytometry gating strategy for isolation of antigen-specific B cells. Splenic B cells were pooled from immunized BALB/c mice and stained for surface markers and antigen probes. The gating strategy is shown for two representative samples: MO1-RBD (top) and RU15-1-RBD (bottom). Lymphocytes were first identified based on FSC and SSC profiles, followed by doublet exclusion. Live cells were gated by excluding 7-AAD$^+$ events. CD19$^+$ B cells were selected, and IgM$^-$/IgD$^-$ class-switched B cells were further enriched. OVA-negative (BV605$^-$) cells were gated to exclude non-specific binding. Antigen-specific B cells were identified as double-positive for PE-conjugated SA-MO1-RBD or SA-RU15-1-RBD and APC-conjugated SA-MO1-RBD or SA-RU15-1-RBD, respectively. These antigen-binding B cells were subsequently sorted for downstream single-cell V(D)J sequencing and antibody cloning. (**b-c**) Heatmap for pair-wise SPR competition scores of anti-MO1 RBD mAbs, anti-RU15-1 RBD mAbs, with darker blue indicating stronger competition. Corresponding IC50 of mAbs are represented as red bars on the left of each heatmap, with darker red indicating higher neutralizing activity. (**d**) Blockage of MO1/RU15-1 RBD-hFc binding (green) to *E.amu* APN transiently expressed in HEK293T cells by indicated antibodies (10 μg/mL), and analyzed by immunofluorescence. (**e**) Blockage of MO1 (left)/ RU15-1 (right) RBD-hFc binding to *E.amu* APN transiently expressed in HEK293T cells by indicated antibodies (10 μg/mL), and analyzed by flow cytometry. RBD-hFc was stained with goat anti-human Fc conjugated with DL594. (**f**) Inhibition of EriCoV pseudovirus entry by neutralizing antibodies in HEK293T cells transiently expressing *E.amu* APN. BSA: Bovine serum albumin, 10 μg/mL. Data are presented as mean ± SD. Statistical significance was determined using unpaired two-tailed *t* tests (n=3 biological replicates). *: $P<0.05$, **: $P<0.01$, ***: $P<0.005$, ****: $P<0.001$, and NS: not significant. Scale bars: 100 μm.



Extended Data Fig. 10 | The Cryo-EM processing workflow. (**a-b**) Flowcharts for structure determinations of MO1 RBD bound to BD23-0087 and BD23-0027 (a), and RU15-1 RBD bound to BD23-0177 and BD23-0152 complex (b). Gold-standard Fourier shell correlation (FSC) curves are shown to assess map quality and resolution. Local resolution assessments of cryo-EM maps using rainbow are shown.


a
MO1 RBD + BD23-0027 + BD23-0087
BD23-0027 HC
MO1 RBD
180°
BD23-0027 LC
BD23-0087 LC
BD23-0087 HC
b
BD23-0027 HC
BD23-0027 LC
Q506
Y32
Y104
N33
N100
Y52
F36
Y101
I503
I513
I34
F533
D499
H536
N534
F456
Y32
MO1 RBD
c
N362 Glycan
BD23-0027
MO1 RBD
d
CDRL3
CDRH1
CDRL1
CDRH2
CDRL2
CDRH3
RU15-1 RBD
CDRH3
CDRH1
CDRL1
CDRH2
CDRL2
CDRL3
MO1 RBD
e
RU15-1_RBD
MO1_RBD
BD23-0027
BD23-0177

Extended Data Fig. 11 | The structural analysis of the neutralizing mechanism of EriCoV RBD-specific antibodies. (**a**) The overall structures of the EriCoV MO1 RBD bound to BD23-0027 and BD23-0087. The MO1 RBDs are shown in medium aquamarine. The heavy chain and light chain of BD23-0027 are colored hot pink and light pink, respectively. Those of BD23-0087 are deep sky blue and light sky blue. (**b**) The interaction details of MO1 RBD bound to BD23-0027. Structures are shown as cartoon representations with key residues rendered as sticks. The hydrophobic pocket and hydrogen bonds are colored semi-transparent blue and yellow dashed lines, respectively. (**c**) The structural basis of the neutralization mechanism of antibodies BD23-0027. The structures are shown as surface, and steric clashes are highlighted by red pentagrams. The *E.amu* APN, MO1 RBDs, and Fabs are colored as described previously. (**d**) Details interactions between the CDRs of BD23-0177 and BD23-0027 with the RU15-1 RBD (left) and MO1 RBD (right), respectively. Close-up views show the interaction interfaces, with the RU15-1 and MO1 RBDs displayed in surface representation and the antibody CDRs shown in cartoon representation. The RU15-1 and MO1 RBDs are colored yellow and medium aquamarine, respectively. Residues that differ between RU15-1 and MO1 RBDs are highlighted in red. The colors of the antibody heavy and light chains are consistent with those described previously. (**e**) Multiple sequence alignment of RU15-1 and MO1 RBDs. The binding sites located within 4 Å of RU15-1 RBD bound to BD23-0177 and MO1 RBD bound to BD23-0027 are indicated by cyan circles and magenta circles, respectively.


a
APN antibodies binding
OD value (450 nm)
BD24-0131
BD24-0134
BD24-0154
hAPN
E.amu APN
b
APN overexpressing HEK293T
E.amu APN
A.alb APN
PSV entry (RLU)
RU15-1
MO1
BD24-0131
BD24-0134
BD24-0154
BSA
Nonneutralizing
Neutralizing
c
APN antibodies
BD24-0131
BD24-0134
BD24-0154
BSA
rcVSV-RU15-1
rcVSV-MO1
d
Primary cells
Live
Death/ contamination
Death
e
Kidney
Intestin
Kidney
24 h
96 h
f
Pseudovirus NT50 293T-E.amu APN cells)
MO1
RU15-1

Extended Data Fig. 12 | Hedgehog APN-specific antibodies efficiently block EriCoV S-mediated entry in APN over-expressing human cell lines and hedgehog primary cells. (**a**) ELISA analyses of the binding efficiency of three indicated *E.amu* APN-targeting antibodies against immobilized hAPN or *E.amu* APN. (**b**) Entry efficiency of RU15-1 and MO1 pseudovirus in HEK293T cells transiently expressing *E.amu* or *A.alb* APN in the presence of 10 μg/mL neutralizing (BD24-0134, and BD24-0154) or non-neutralizing (BD24-0131) antibodies. Mean ± SD for b. BSA: 10 μg/mL Bovine serum albumin for b. RLU, relative light units. (**c**) Evaluation of the neutralizing activity of *E.amu* APN antibodies (10 μg/mL) against rcVSV-RU15-1 or rcVSV-MO1 in Caco-2 cells overexpressing *E.amu* APN and *E.amu* TMPRSS2. Scale bars, 200 μm. (**d-e**) Primary cells derived from the kidney of the African pygmy hedgehogs (*Atelerix albiventris, A.alb*). (**f**) Neutralization 50% titers of plasma samples from random human donors against MO1 and RU15-1 pseudoviruses, determined using HEK293T-*E.amu* APN cells. Dashed lines indicate the assay baseline.

Extended Data Table 1 Cryo-EM data collection and atomic models refinement statistics

Data collection					
Complex	RU15-1 Spike	E.amu APN in complex with RU15-1 RBD	E.*amu* APN in complex with RU15-1 RBD (focused reconstruction)	RU15-1 RBD + BD23-0177 + BD23-0152	MO1 RBD + BD23-0027 + BD23-0087
Microscope	FEI Titan	FEI Titan	FEI Titan	FEI Titan	FEI Titan
Camera	Gatan K3	Gatan K2	Gatan K2	Gatan K2	Gatan K2
Voltage (kV)	300	300	300	300	300
Total dose (e^-/A^2)	60	60	60	60	60
Micrographs (total)	2,125	3,559	3,559	4,260	4,002
Micrographs (used)	2,125	3,559	3,559	4,260	4,002
Particles selected	1,073,532	1,178,055	1,178,055	1,516,562	1,134,767
Particles included in final reconstruction	215,898	170,003	285,605	179,494	129849
sampling, Å per pixel	1.07	0.82	0.82	0.82	0.82
Defocus range (μm)	-1.2 ~ -2.0	-1.2 ~ -2.0	-1.2 ~ -2.0	-1.2 ~ -2.0	-1.2 ~ -2.0
Symmetry	C3	C2	C1	C1	C1
Resolution (Å) (FSC=0.143 criterion)	3.34	3.28	3.38	3.84	3.65
Model refinement					
Ramachandran statistics (%)					
Most favored	95.17	93.76	92.58	92.12	92.63
Allowed	4.35	5.88	6.7	7.11	6.45
Outliers	0.48	0.36	92.58	0.77	0.92
Bonds (RMSD)					
Bond lengths (Å)	0.004	0.004	0.004	0.003	0.005
Bond angles (°)	0.63	0.663	0.809	0.839	0.93
MolProbity score	1.71	1.95	2.01	2.19	2.09
Clash score	6.63	10.3	10.33	15.97	12.99
Rama-Z					
Rotamer outliers (%)	0.56	0.51	1.02	0	0.54
Cβ outliers (%)	0	0	0	0	0

Supplementary Files

This is a list of supplementary files associated with this preprint. Click to download.

- SupplementaryTable1EriCoVSsequence.xlsx
- SupplementaryTable2E.amureceptorsequences.xlsx
- SupplementaryTable3APNorthologuessequencesinthisstudy.xlsx
- SupplementaryTable4TheantibodysequencesofRU151RBDMO1RBDandE.amuAPN.xlsx
- SupplementaryTable5Demographicdatafortheplasmadonors.xlsx
- D1300066549valreportfullP1EriCoVRU151RBDE.amuAPN.pdf
- D1300066579valreportfullP1.pdf
- D1300066582valreportfullP1.pdf
- D1300066564valreportfullP1.pdf
- D1300066461valreportfullP1.pdf